Glycemic challenge is associated with the rapid cellular activation of the locus ceruleus and nucleus of solitary tract: Circumscribed spatial analysis of phosphorylated MAP kinase immunoreactivity in relation to catecholaminergic and cholinergic chemoarchitecture

Geronimo P. Tapia [1,3,†], Lindsay J. Agostinelli [5,†], Sarah D. Chenausky [1,2], Jessica V. Salcido Padilla [1,2], Vanessa I. Navarro [1,3], Amy Alagh [5], Gabriel Si [5], Richard H. Thompson [5,6], Sivasai Balivada [1], and Arshad M. Khan [1,4,5,*]

[1]UTEP Systems Neuroscience Laboratory, Department of Biological Sciences, The University of Texas at El Paso, El Paso, TX 79968, USA; gptapia@miners.utep.edu (G.P.T.); sarahchenausky@gmail.com (S.D.C.); jvsalcido@miners.utep.edu (J.S.P.); vinavarro@miners.utep.edu (V.I.N.); sbalivada@utep.edu (S.B.); amkhan2@utep.edu (A.M.K.)

[2]M.S. Program in Biology, Department of Biological Sciences, The University of Texas at El Paso

[3]Ph.D. Program in Bioscience, Department of Biological Sciences, The University of Texas at El Paso

[4]Border Biomedical Research Center, College of Science, The University of Texas at El Paso

[5]Department of Biological Sciences, University of Southern California, Los Angeles, CA 90089, USA; ljagostine@gmail.com (L.J.A.); amy.alagh@gmail.com (A. Alagh); gsiusc@gmail.com (G.S.)

[6]School of Information, The University of Texas at Austin, Austin, TX, 78701, USA; rhthompson@utexas.edu (R.H.T.)

*Correspondence: amkhan2@utep.edu; Tel.: +1-915-747-8436

†These authors contributed equally to this work.

Abstract

Research using laboratory rats has shown that impaired glucose utilization or hypoglycemia is associated with cellular activation of neurons in the *medulla (Winslow, 1733)* (MY) that are implicated in the control of feeding behavior and hormonal counterregulatory responses. Changes in the activation of these neuronal populations are also associated with autonomic dysfunction that manifests itself in the form of blunted counterregulatory responses to repeated episodes of glucoprivation or hypoglycemia. An improved appreciation of the spatiotemporal dynamics of these medullary responses — and the phenotypes of the neurons responsible for them — could lead to the development of rational therapies or diagnostics to address patient complications associated with diabetes management, such as hypoglycemia-associated autonomic failure. At present, however, cellular-scale neural activation following glycemic challenge has been tracked in rodents primarily within hours of the challenge, rather than sooner, and these responses have been poorly mapped within standardized brain atlases in relation to the locations of cell types known to be present in the medulla and the larger *rhombic brain (His, 1893)* (RB). Here, we report that within 15 min of receiving the glycemic challenge, 2-deoxy-D-glucose (2-DG; 250 mg/kg, i.v.), which is known to produce intracellular glucopenia and trigger glucoprivic feeding behavior, marked elevations were observed in the numbers of RB neuronal cell profiles immunoreactive for the cellular activation marker(s), phosphorylated p44/42 MAP kinases (phospho-ERK1/2). Dual immunostaining experiments showed that some, but not all, of these neurons were catecholaminergic, as identified by immunostaining for dopamine β-hydroxylase (DBH). To begin the process of mapping the locations of these rapidly-activated neurons in relation to known cytoarchitecture with standardized neuroanatomical nomenclature, we performed Nissl- and chemoarchitecture-based plane-of-section analysis to map their distributions at discrete rostrocaudal levels, along with associated basally-activated cholinergic and other catecholaminergic cell groups, within an open-access rat brain atlas. This analysis revealed that neurons of the *locus ceruleus (Wenzel & Wenzel, 1812)* (LC) and the *nucleus of solitary tract (>1840)* (NTS) displayed elevated numbers of phospho-ERK1/2+ neurons within 15 min following 2-DG administration. Notably, while catecholaminergic neurons co-labeled with phospho-ERK1/2 immunoreactivity, many non-catecholaminergic NTS neurons also displayed such activation. Both 2-DG and saline-treated groups also displayed phospho-ERK1/2+ neurons in the *dorsal motor nucleus of vagus nerve (>1840)*, identified both by Nissl criteria and immunostaining for the cholinergic marker, choline acetyltransferase. Our results show that 2-DG-activation of certain RB catecholaminergic neurons is more rapid than perhaps previously realized, engaging neurons that serve multiple functional systems and are of varying cellular phenotypes. They also place these and other activated populations within standardized maps of cytoarchitectonically-defined RB regions, thereby streamlining their precise targeting and/or comparable mapping in preclinical rodent models of disease.

Keywords: mapping; brain atlas; neural network; deoxyglucose; feeding; locus coeruleus; hindbrain

1. Introduction

Glucose is the essential metabolic fuel source for the brain, with a constant and adequate supply needed for proper function and survival. Iatrogenic hypoglycemia is a formidable clinical problem for patients suffering from diabetes mellitus [1], and despite steady improvements in long-term diabetes management [2], remains a major limiting factor in such management for both Type I and Type II diabetics [1, 3–5]. Glucose counterregulatory mechanisms defend the body against precipitous drops in blood sugar by increasing glucagon and reducing insulin secretion from pancreatic α and β cells, respectively; and by increasing epinephrine release from the adrenal medulla [6]. In Type I and advanced (end-stage) Type II diabetes, these defenses are impaired, thereby compromising the body's ability to maintain glucose homeostasis. Such impairment becomes exacerbated during hypoglycemia-associated autonomic failure (HAAF), in which antecedent iatrogenic hypoglycemia causes defective glucose counterregulation by blunting plasma epinephrine responses to a given level of subsequent hypoglycemia — all in the face of impaired glucagon release and insulin reductions [7]. In addition to defective glucose counterregulation, HAAF is often associated with hypoglycemia unawareness, in which "cognitive function is so disturbed that the patient can become drowsy, uncoordinated, confused or even comatose" [8].

Human and animal models for HAAF exist but need refinement [9], partly because not all of the fundamental mechanisms underlying counterregulation have been elucidated [10]. Although sensors in the periphery (*e.g.*, portal vein [11, 12]) contribute to counterregulatory responses to glycemic challenges, there is a growing understanding that brain mechanisms also contribute to these responses [12–15]. Therefore, there have been intensive efforts to understand how the *central nervous system (Carus, 1814)* [16] (CNS) (*see Section 2.1 for naming conventions used in this study*) senses circulating levels of glucose and initiates counterregulatory responses, and how CNS impairments contribute to defective glucose counterregulation [17–20]. In particular, a compelling body of evidence has established a critical role for various *Rhombic brain (His, 1893)* [21] (RB) regions in glucosensing and counterregulatory responses to glycemic challenges [22–36], with much of this work focused on the role of catecholaminergic neurons in the *medulla (Winslow, 1733)* [37] (MY) in these functions [17, 38–42]. Certain neuronal populations in the *hypothalamus (Kuhlenbeck, 1927)* [54] (HY) also appear to be glucosensing and/or critical for counterregulation [55–65], and neural circuits linking the RB to the HY help trigger feeding and hypothalamo-pituitary-adrenal (HPA) axis responses to glycemic challenges [15, 66–73]. Moreover, peripheral glucosensing mechanisms can be linked by neural circuits to RB regions controlling counterregulatory responses [18, 19, 74–76].

Despite these advances in our understanding of RB glucosensing and counterregulation, two points regarding the spatiotemporal dynamics of these responses remain unclear, both of which are the focus of the present study. First, in terms of temporal dynamics, it is not fully understood how quickly RB neuronal networks track changes in glycemic status *in vivo*. Immunodetection of the transcription factor, Fos, has been used to track RB neuronal activation associated with glycemic challenge [30, 39, 42, 53, 75], but its protein expression typically peaks within 1–3 hours [77]. Thus, it is difficult to attribute its delayed expression to changes in glycemic status per se rather than to secondary effects set in motion by such changes. Ideally, an anatomically non-labile biomarker of an "activated" neuron should be induced at a time more proximate to the stimulus event (discussed in [79]). In this study, the phosphorylated forms of p44/42 MAP kinases were used to rapidly track glycemic challenge, a strategy first employed by the Watts laboratory [66–69].

Second, in terms of spatial dynamics, the locations of RB neuronal populations that are activated following glycemic challenge have not been charted precisely within standardized atlases of the brain, rendering their reproducible experimental targeting and documentation more difficult (discussed in [80]). Nor is it clear if RB neuronal populations more traditionally studied in the context of arousal rather than hormonal counterregulation are also activated rapidly by glycemic challenge. This knowledge could help us understand if such regions might play a role in producing the cognitive perceptions of hypoglycemic events, the absence of which could contribute to hypoglycemia unawareness in diabetic individuals [8, 81]. Here, we build upon previous work [68] to map RB neuronal activation associated with glycemic challenge to an open-access rat brain atlas [82] and identify the *locus ceruleus (Wenzel & Wenzel, 1812)* [83], a key arousal-promoting RB structure, as a region displaying rapid activation to glycemic challenge, alongside other RB structures more traditionally understood to serve in

networks for glucosensing and counterregulation. Taken together, the results of this work, portions of which have been presented in preliminary form [85–89], provide evidence that RB neuronal populations implicated in glucosensing, counterregulation and arousal can track the onset of glycemic challenge within 15 minutes. The cellular activation patterns mapped in this study are a useful starting point towards the development of global CNS cellular activation maps for glycemic challenges.

2. Materials and Methods

2.1 Neuroanatomical naming conventions used in this study

In this study, as part of our ongoing effort to encourage the use of standardized nomenclature to enable the seamless registration of datasets across laboratories (and datasets within our own laboratory), we use *standard terms* for brain structures as proposed by Swanson [82, 90]. These terms are listed in italics together with the associated citation that first uses the term as defined. Note that the author-date citation is part of the standard term, and these nomenclature-embedded citations are also included in the references list. If a definitive assignment of priority for the term was not possible, it was assigned by Swanson the citation "(>1840)"; that is, "defined sometime after the year 1840″. Refer to Swanson [82, 90] for further details regarding this standard nomenclature system.

2.2 Subjects and surgical procedures

All procedures were approved by the Institutional Animal Care and Use Committee of the University of Southern California (Protocol code #11239). Adult male Sprague-Dawley rats (Harlan Labs, Indianapolis, IN, USA; n = 12; body weights (BW) 258–270 g on the day of surgery) were single-housed and kept on a 12h:12h light:dark cycle (lights on: 6:00 a.m.) with *ad libitum* access to standard laboratory animal chow and water. On the day of surgery, each rat was anesthetized with a cocktail of 50% ketamine (100 mg/ml), 25% xylazine (100 mg/ml), and 10% acepromazine (10 mg/ml) dissolved in 0.9% sterile saline; delivered i.m. at 0.1 ml of cocktail/100 g BW). The animal was judged to be at the appropriate surgical plane of anesthesia by tracking expected reductions in respiratory rate following anesthesia, as well as the absence of a reflex response to a brief tail or paw pinch. Once under this level of sedation, the animal was placed ventral side up on a surgical pad and prepared for surgery. Intra-atrial catheterizations by way of the jugular vein, under aseptic surgical conditions, were performed as previously reported [66, 91], with additional details noted here as follows. The throat was shaved, disinfected with surgical scrub, and the right jugular vein located under the guidance of a dissecting stereoscope and fiber-optic illumination. The surgical target area harboring the vein was apparent under the microscope by the fluttering of the overlying skin with each heartbeat. Once the area was located in this manner, cold-sterilized forceps and surgical scissors were used to lift up the skin and make an incision to expose the jugular vein. A previously-prepared cold-sterilized catheter assembly consisting of silastic tubing (0.020" i.d., 0.037" o.d.; Catalog # 76P020-210-037; Specialty Manufacturing, Inc., Saginaw, MI), held fast by cured cyanoacrylate glue and a 23-gauge stainless steel connector to larger-diameter Tygon tubing, was first flushed with sterile 0.9% saline, and then inserted slowly through the vein and into the atrium of the heart. It was held firmly but loosely in place with two lines of suture filament threaded under the vein and catheter assembly. Once secured in this manner, the catheter was gently aspirated using a 1.0 ml syringe to ensure blood flow from the heart, and the filaments untied if adjustments were needed. Once patency was confirmed, the filaments were then tied securely, as were two additional filaments, and the larger end of the tubing was exteriorized by tunneling it under the skin and out through the subscapular space. The entire procedure took approximately 15–20 min for each animal, after which the incision was closed using wound clips and cleaned. Post-operative care consisted of administration of flunixin meglumine analgesic (0.25 mg/100 g BW, i.m.) and gentamicin antibiotic (0.2–0.4 mg/100 g BW, i.m.), and the careful daily monitoring and gentle handling of each animal throughout the course of the 3–6-day recovery period, during which time each animal was weighed to determine whether they reached pre-surgical body weight. During this recovery period, their newly-installed catheters were also inspected and flushed daily with heparinized saline to ensure their patency.

2.3 In vivo experimental procedures

On the day of the experiment, during the early portion of the light phase, the animals received an injection, through the catheter, of 0.9% sterile saline as a vehicle control (n = 7), or 250 mg/kg of 2-deoxy-D-glucose (2-DG; catalog #D6134-5G; MilliporeSigma, Inc., Burlington, MA, USA) dissolved in the vehicle (n = 5). This intravenous procedure was intended to eliminate pain-related neuronal activation that would otherwise occur by administering the treatment through intraperitoneal injection. Approximately fifteen minutes after receiving saline or 2-DG, subjects received an intravenous infusion of ~1.0 ml sodium pentobarbital anesthesia (50 mg/kg) over a 30-sec period. Deeply sedated, the subjects were relocated to a fume hood, under which they were perfused transcardially, first with 0.01 M sodium phosphate-buffered saline and then with freshly depolymerized 4% (w/v) *p*-formaldehyde, buffered to pH 9.5 using sodium borate. The fixed brain was removed from the cranium, placed overnight on a shaker at 4°C in 4% (w/v) *p*-formaldehyde containing 12% (w/v) sucrose, blocked into forebrain and hindbrain segments, and then frozen using hexane supercooled on a bed of powdered dry ice. The frozen blocks were removed from the hexane bath and stored in vials at –80°C until sectioning.

2.4 Tissue processing and immunocytochemistry

2.4.1 Histological processing of brain tissue. Rhombic brain (His, 1893) [21] (RB) blocks were removed from –80°C and mounted onto the freezing stage of a Reichert sliding microtome and cut into 20-µm-thick coronal sections. Sections kept for histochemical staining were collected as eight 1-in-8 series in tissue culture wells filled with cryoprotectant (50% phosphate buffer, 30% ethylene glycol, 20% glycerol; pH 7.4) and stored at –20°C until further processing. In most cases, the fourth tissue series collected was reserved for preparing a cytoarchitectural *Reference (R) series* using Nissl-staining (*see Section 2.5*), while the remaining tissue series were reserved for immunohistochemical analyses. The *R series* for any one subject is defined as the tissue series from which we used cytoarchitectural information to identify the boundary conditions for mapping the atlas gray matter regions (Swanson & Bota, 2010) of our immunoreactive neuronal populations, which were visualized in adjacent tissue series from the same subject.

2.4.2 Immunohistochemistry

2.4.2.1. Main procedures. Using Tris-buffered saline (TBS) (0.05 M; pH 7.4 at room temperature), sections were rinsed of cryoprotectant (5 rinses for 5 minutes each; 5 × 5) and were then incubated in blocking solution consisting of TBS containing 2% (v/v) normal donkey serum (Catalog # S30–100ML; EMD-Millipore), and 0.1% (v/v) Triton X-100 for ~1.5–2.0 h at room temperature. The tissue was reacted with a cocktail consisting of blocking solution together with primary antibodies targeting dopamine-β-hydroxylase (EC 1.14.17.1), choline acetyltransferase (EC 2.3.1.6), or the phosphorylated forms of ERKs 1 and 2 (EC 2.7.11.24) (*see* **Table 1** *for details*). After another 5 × 5 TBS rinse, the sections were reacted with the appropriate secondary cocktail (again with blocking solution), followed by a conjugate reagent **(Table 1)**. The tissue underwent a final 5 × 5 wash series before being mounted on Superfrost™ Plus slides, which were coverslipped with sodium bicarbonate-buffered glycerol (pH 8.6 at room temperature), sealed with clear nail polish, stored at 4°C, and protected from ambient light until further analysis.

2.4.2.2 Antibody information. Preadsorption experiments performed by ourselves or other laboratories have demonstrated the specificity of the primary antibodies we used in this study for binding to their intended antigen targets. First, as noted previously [67], preadsorption of the rabbit phospho-ERK1/2 antibody we used in this study with the immunizing peptide used to produce it abolished all immunostaining in brain tissue (AMK; *unpublished data*). Second, the mouse monoclonal anti-DBH antibody we used reportedly produces immunoreactivity that is completely abolished in rat brain tissue sections when the antibody is preadsorbed with a 10-fold excess of bovine adrenal DBH [92]. Similarly, the primary anti-ChAT antibody we used, which was raised against human placental ChAT, reportedly did not produce immunoreactive signal when preadsorbed with a rat recombinant ChAT protein [93].

2.4.2.3 Control experiments to test for secondary antibody cross-reactivity. A series of tests were performed to check the specificity of the secondary antibodies we used for their primary antibody targets. First, using a single series from saline- (#K10-011) and 2-DG-treated (#K10-026) subjects, we performed immunofluorescence histochemical experiments as noted above, but using secondary antibodies that were purposefully mismatched

Table 1. Antibody combinations

Reagent [a]	Antigen or Conjugate	Host	Type	Source [b], Catalog #	Titer [c]	RRID	Reaction (h, temp.) [d]
Reaction Series 1							
Primary	Phospho-ERK1/2 [e]	Rb	Poly IgG	CST, 9101 [j]	1:1,000	AB_331646	64–66, 4°C
Secondary	Rabbit IgG (H+L) [f]	Dk	Cy3-labeled	JIL, 711-165-152 [k]	1:500	AB_2307443	5–6, 4°C
Primary	DBH	Ms	Mono IgG	M, MAB308 [l]	1:10,000	AB_2245740	64–66, 4°C
Secondary	Mouse IgG (H+L) [g]	Dk	Biotinylated	JIL, 715-065-150 [m]	1:500	AB_2307438	5–6, 4°C
Conjugate	Streptavidin		A488-labeled	TF, S-11223 [n]	1:2,000	na	1, 4°C
Primary	human placental ChAT	Gt	Poly IgG	M, AB144P [o]	1:6,000	AB_2079751	64–66, 4°C
Secondary	Goat IgG (H+L) [h]	Dk	A647-labeled	JIL, 705-605-147 [p]	1:500	AB_2340437	5–6, 4°C
Counterstain	DAPI [i]	–	RNA label	TF, D1306 [q]	1:4,000	na	0.5, RT
Reaction Series 2							
Primary	Phospho-ERK1/2 [e]	Rb	Poly IgG	CST, 9101 [j]	1:1,000	AB_331646	60–65, 4°C
Secondary	Rabbit IgG (H+L) [f]	Dk	Biotinylated	JIL, 711-065-152^	1:500	AB_2340593	4–5, 4°C
Conjugate	Streptavidin		A488-labeled	TF, S-11223 [n]	1:2,000	na	1, 4°C
Primary	DBH	Ms	Mono IgG	M, MAB308 [l]	1:10,000	AB_2245740	60–65, 4°C
Secondary	Mouse IgG (H+L) [g]	Dk	Cy3-labeled	JIL, 715-165-150^	1:500	AB_2340813	4–5, 4°C
Primary	human placental ChAT	Gt	Poly IgG	M, AB144P [o]	1:6,000	AB_2079751	60–65, 4°C
Secondary	Goat IgG (H+L) [h]	Dk	A647-labeled	JIL, 705-605-147 [p]	1:500	AB_2340437	4–5, 4°C

^ Lot # not available.

[a] Reagents used within a common reaction set are grouped by reaction number in the left column. Each number represents a common set of reagents applied to one series of tissue sections.

[b] See abbreviations below for full names of suppliers.

[c] The dilutions listed are calculated from the suppliers' stock. All secondaries and conjugate stocks from suppliers were diluted 1:2 in glycerol (i.e., 50% glycerol, 50% buffer), and the dilution listed (e.g., 1:500) is the final dilution. Thus, for example, we calculated a 1:250 dilution of the 1:2 working stock to obtain the final 1:500 dilution.

[d] The total duration of incubation (in hours) is listed, followed by the temperature at which the incubation proceeded. In many cases, the duration is expressed as a range, based on the exact parameters of reactions run on separate occasions.

[e] Phospho-ERK1/2 antibodies recognize the phosphoryl modifications of p44/42 MAP kinases on residues Thr^{202} and Tyr^{204} (Thr^{183} and Tyr^{185} in rat ERK2).

[f] According to the supplier's information, this affinity-purified secondary antibody displayed minimal cross-reactivity with bovine, chicken, goat, guinea pig, Syrian hamster, horse, human, mouse, rat, or sheep serum proteins.

[g] According to the supplier's information, this affinity-purified secondary antibody displayed minimal cross-reactivity with bovine, chicken, goat, guinea pig, Syrian hamster, horse, human, rabbit, or sheep serum proteins.

[h] According to the supplier's information, this affinity-purified secondary antibody displayed minimal cross-reactivity with chicken, guinea pig, Syrian hamster, horse, human, mouse, rabbit, or rat serum proteins.

[i] For some, but not all, reactions using this combination of reagents, 4,6 diamidino-2-phenylindole dihydrochloride (DAPI) was used as a counterstain.

[j] Lot #19 or #27 (run by SDC); Lot #30 (run by VIN)

[k] Lot #131748 (run by VIN)

[l] Lot #2029625 (run by SDC); Lot #3736685 (run by VIN)

[m] Lot #107814 (run by VIN)

[n] Lot #1103102 (runs by SDC, VIN)

[o] Lot #NG1825168 (run by SDC); Lot #3233120 (run by VIN)

[p] Lot #103972 (run by SDC); Lot #116978 (run by VIN)

[q] Lot#1159932 (run by SDC)

Table 1 Abbreviations: A488, Alexa 488; A647, Alexa 647; ChAT, choline acetyltransferase; CST, Cell Signaling Technology, Inc.; DBH, dopamine beta-hydroxylase; Dk, donkey; ERK1/2, extracellularly-regulated kinases 1 and 2; Gt, goat; (H+L), immunoglobulin heavy and light chains; IgG, immunoglobulin G; JIL, Jackson ImmunoResearch Labs; M, MilliporeSigma; Mono, monoclonal; Ms, mouse; na, not applicable; Poly, polyclonal; Rb, rabbit; RT, room temperature; TF, Thermo Fisher.

to the original primary antibodies. Thus, immunofluorescent staining for DBH was conducted using sections containing the *nucleus of solitary tract (>1840)* (NTS) (to ensure DBH was present) selected from the saline-treated animal case. Visual confirmation of the presence of the NTS was performed using surrounding white matter landmarks made visible under dark-field illumination (Olympus BX63 microscope, ×10 magnification objective lens; *see Section 2.6.1 for details*). The primary mouse anti-DBH antibody was used in conjunction with both a Cy3-labeled donkey anti-rabbit IgG, and an Alexa 647-conjugated donkey anti-goat IgG. The Alexa 488-conjugated streptavidin reagent was also added to the reaction. The primary antibody incubations lasted 18 h at 4 °C, the secondary antibody incubations for 5 h at room temperature, and the incubation of Alexa 488-conjugated streptavidin for 1 h at room temperature. Similar experiments were conducted for anti-pERK1/2, anti-DBH, and anti-ChAT using selected sections containing the *nucleus of the solitary tract (>1840)* (NTS), *locus ceruleus (Wenzel & Wenzel, 1812)* [83] (LC), *dorsal motor nucleus of vagus nerve (>1840)* (DMX), and *hypoglossal nucleus (>1840)* (XII) from a 2-DG-treated subject (#K10-026).

2.4.2.4 Control experiments to test for nonspecific binding of secondary antibodies to tissue sections. To ensure that secondary antibodies were not producing labeling patterns as a result of a direct and non-specific binding to endogenous proteins in the tissue, we performed our fluorescence immunohistochemistry on a subset of tissue sections for which the primary antibodies were not included in the reaction sequence. To keep consistency across controls, we selected tissue sections from a 2-DG treated subject (#K10-026) that was comparable to those selected for the saline-treated subject tested in *Section 2.4.2.3*. The secondary antibodies were reacted as a cocktail, and consisted of the Cy3-labeled donkey anti-rabbit IgG, the biotinylated donkey anti-mouse IgG, and the Alexa 647-labeled donkey anti-goat IgG listed in **Table 1**. Sections were incubated at 4°C for 18 h in blocking solution (to mimic the reaction duration ordinarily used for the primary antibody step) and 5 h in the secondary antibody cocktail at room temperature.

2.4.2.5 Checks for tissue autofluorescence. To verify that unlabeled tissue sections did not exhibit any endogenous fluorescence contributing to the signal observed, sections containing the *locus ceruleus (Wenzel & Wenzel, 1812)* [83] (LC) were first selected by carefully checking for tissue sections containing the structure as observed under dark-field illumination. Cryoprotectant was removed from sections in a series of 5 × 5 washes in TBS in a netted well tray. Sections were removed from the netted well tray, mounted onto Superfrost™ slides, and allowed to air-dry for 1 h under light-protected conditions. The slides were coverslipped using bicarbonate-buffered glycerol mounting solution and sealed with clear nail polish around the edges of the slide. Photomicrographs were then taken using an Olympus BX63 microscope at ×10 and ×20 magnifications to check for observable signal in the tissue.

2.4.2.6 Checks for binding of Streptavidin-Alexa 488 to endogenous biotin in tissue. We aimed to account for any endogenous binding of streptavidin used to stain the biotinylated secondary antibodies used in this study. As before, sections containing the LC were selected under dark-field illumination, rinsed of cryoprotectant with TBS (5 × 5 washes), and transferred to a 24-well plate containing Alexa 488-conjugated streptavidin solution for 1 h at room temperature. Sections were then rinsed again (5 × 5) in TBS, mounted onto Superfrost™ slides, and allowed to dry for 1 h. Slides were as before coverslipped and sealed with nail polish. Photomicrographs were again taken using an Olympus BX63 microscope at ×10 and ×20 magnifications to check for observable signal in the tissue.

2.5 Nissl staining of the Reference (R) tissue series

The *R series* of tissue sections (adjacent to those that underwent immunohistochemical staining) was washed 5 × 5 in TBS and mounted onto gelatin-coated slides, dehydrated in ascending concentrations of ethanol (50%, 70%, 95%, 100%) and defatted with xylene. Sections were then rehydrated and stained with a 0.25% w/v thionine solution (sold as "thionin acetate" by Sigma-Aldrich; MW 287.34 g/mol; cat #T7029; ([94], p. 151); [95]). A 0.4% glacial acetic acid solution was used to remove excess thionine and the tissue slides were dehydrated in ascending concentrations of ethanol solutions (50%, 70%, 95%, 100% × 3), and then cleared in mixed-isomer xylenes before being coverslipped using DPX mountant for bright-field microscopic observation (*Section 2.6.1*).

2.6 Microscopy and photomicrography

2.6.1 Bright-field microscopy. A total of 93 *R series* (Nissl-stained) tissue sections, for a subset of saline- and 2-DG-treated subjects (n = 2 and 3, respectively), were photographed under bright-field illumination using an Olympus BX63 light microscope with an X-Y-Z motorized stage and an attached DP74 color CMOS camera (cooled, 20.8 MP pixel-shift, 60 fps) (Olympus America, Inc., Waltham, MA, USA). Image acquisition was carried out using cellSense™ Dimension software (Version 2.3; Olympus) installed on a Hewlett Packard PC workstation. The software was used to drive the motorized stage and generate tiled and stitched wide-field mosaic photomicrographs of the entire tissue section using a ×10 magnification objective lens (Olympus UPlanSApo, N.A. 0.40, FN 26.5 mm). Stitching was performed with a 15% overlap of individual images.

2.6.2 Epifluorescence and dark-field microscopy. Selected tissue sections from subjects receiving saline or 2-DG were photographed using epifluorescence illumination. Identifying information was first obscured on all tissue slides by a team member (AMK), and the sections were then photographed by another team member (GPT) who was thus blind to the treatment groups. Photography was carried out using an Axio Imager M.2 upright epifluorescence microscope (Carl Zeiss, Inc., Thornwood, NY, USA) equipped with an X-Y-Z motorized stage and a 100 W halogen light source. The appropriate filter cubes were used to detect the immunofluorescence of the sections in separate non-interfering channels, which was captured by a EXi Blue monochrome camera (Teledyne QImaging, Inc., Surrey, British Columbia, Canada) driven by Volocity software (versions 6.0.0–6.1.1; Quorum Technologies, Puslinch, Ontario, Canada) installed on a Mac Pro computer (Apple Corp., Cupertino, CA, USA). Single fields of view and ×20-magnification (Plan-Apochromat objective lens; N.A., 0.8) wide-field mosaics of individual fields of view (stitched with 20–40% overlap) were acquired within Volocity and exported as uncompressed TIFF files. These photomicrographs were also exported as compressed JPEG files for conference presentation of preliminary results [86, 87]. ROIs were photographed for each subject from the left and right sides of the *rhombic brain (His, 1893)* [21] (RB), and included the *locus ceruleus (Wenzel & Wenzel, 1912)* [83], *area postrema (>1840)*, *nucleus of the solitary tract, medial part (>1840)*, *dorsal motor nucleus of vagus nerve (>1840)*, and *hypoglossal nucleus (>1840)*. Care was taken to ensure that all photomicrographs were captured under similar illumination conditions. For certain sections where the companion *R series* tissue was damaged or otherwise unavailable for reference, a photomicrograph was taken – under dark-field illumination – of the fluorescence tissue series in order to obtain fiducial landmarks to help delineate cytoarchitectural boundaries and to determine the atlas level assignment of the tissue section (*e.g.*, see **Fig. 2A-i**).

2.6.3 Confocal microscopy. For selected *rhombic brain (His, 1893)* [21] (RB) tissue sections, additional imaging was performed using a Zeiss LSM 700 laser scanning confocal system connected to a Zeiss Observer.Z1 inverted fluorescence microscope (Carl Zeiss, Inc., Thornwood, NY, USA), located in the Cellular Characterization and Biorepository Core Facility of the Border Biomedical Research Center at UT El Paso. The system is equipped with four solid-state lasers, including those at 488-nm, 555-nm, and 639-nm wavelengths, which were used to detect Alexa 488, Cy3, and Alexa 647 fluorophore signals, respectively. The microscope was driven by Zen 2009 software (release version 6.0 SP2; version 6.0.0.303; Carl Zeiss Microimaging GmbH). Under a *Continuous* scan mode, we used the lookup table *Range Indicator* in the software to guide *Gain (Master)* and *Digital Offset* adjustments to keep the image signal spread over the dynamic range of the detector, and to prevent missing pixels or pixel saturation as a result of under- or overexposed regions of tissue, respectively.

Once it was determined that the signal was within the detector's dynamic range, sequential unidirectional scans of the tissue were taken using Plan-Neofluar objective lenses of ×10 (N.A., 0.3; Ph1), ×20 (N.A., 0.5), or ×40 (N.A., 1.3; oil) magnification. Pinhole settings were kept at or close to 1 Airy unit [96] for each channel, defined as the width of the point-spread function for that channel; however, for images used for co-localization analysis, the pinholes were adjusted above or below the 1 Airy unit setting so that the widths of the optical sections for each channel were matched in the axial (z) dimension to ensure accurate comparison of signals [97]. With a few exceptions, frame sizes were set to 2048 × 2048 pixels. Image sizes were 618.9 μm × 618.9 μm (pixel size = 0.30 μm). Scanning was performed at a slow scan speed (setting: 4) with 16 frames averaged over a scan time of ~36 minutes (~12 min/channel). Scans were exported as full-resolution uncompressed TIFF files and imported onto artboards in Adobe Illustrator CC (version 25.0; Adobe Systems, Inc., San Jose, CA, USA) to prepare figures for

this study.

2.6.4 Visualization of far-red fluorescent signals. For preparation of certain photomicrographs of ChAT-immunolabeled cells in the far-red channel, which were acquired from tissue displaying a faded fluorescence, brightness and contrast were enhanced in Adobe Photoshop to help the reader visually differentiate the faint cells from background and to aid the reader in assessing patterns in two-channel images; these changes, which were applied to the whole image in each instance, are noted in the caption of each relevant figure. For these images, along with the remaining images shown in this study, care was taken that all acquisition and post-acquisition parameters were identical for images displayed together from control and 2-DG treatment groups, in keeping with community standards (*e.g.*, [98]).

2.6.5 Checks for fluorescence crosstalk. A number of quality-control checks, which are also recommended as community standards (*e.g.*, [97, 99]) were performed to evaluate crosstalk (bleed-through) of the fluorescence signals we detected in this study.

2.6.5.1 Evaluating crosstalk at the level of fluorescence labeling. Three approaches were employed – two precautionary and one empirical – to help exclude the possibility that secondary antibody-fluorophore combinations cross-reacted with primary antibodies they were not meant to target. First, for our three target antigens (DBH, pERK1/2, ChAT), we used primary antibodies produced in host organisms that were far apart from one another in taxonomic relatedness (mouse, rabbit, and goat; respectively) so cross-reactivity would be minimized. Second, we employed affinity-purified secondary antibodies that were preadsorbed by the supplier against the sera of the other host organisms of secondaries used in our cocktail (*i.e.*, organism cross-adsorbed secondary antibodies). *Footnotes f–h* of **Table 1** provide details on these cross-adsorption screens. For example, the donkey anti-goat IgG we used was cross-adsorbed with sera from mouse, rat and rabbit; among other taxonomic groups (**Table 1**, *footnote h*). Third, we performed control experiments to test for cross-reactivity. For example, tissue reacted with the rabbit anti-pERK1/2 antibody was incubated with an intentionally-mismatched secondary-fluorophore combination (*e.g.*, biotinylated donkey anti-mouse IgG, followed by streptavidin-Alexa 488; or donkey anti-goat IgG conjugated to Alexa 647). For all of these reactions, cross-reactivity was never observed.

2.6.5.2 Evaluating crosstalk under epifluorescence imaging. At the level of our epifluorescence microscopy and imaging workflow, we performed single-label immunohistochemical experiments of tissues collected from saline- and 2-DG-treated subjects to ascertain whether an individual signal did not bleed through into the other channels. Some pre-existing single-labeled material (supplied by M. Peveto) was also helpful in this regard. We performed this check by examining each signal within its assigned channel as well as in the other two channels we were capturing. No bleed-through was observed for any of the signals in our epifluorescence system.

2.6.5.3 Evaluating crosstalk under confocal imaging. We also used our core facility's confocal system to photograph the tissues processed for single-label immunohistochemistry (*described above in Section 2.5.5.2*) to check for cross-talk in that system. We performed additional checks by laser-scanning our triple-labeled material under conditions where the automated sequence of stepwise laser-enabled excitations was reconfigured to allow for individual lasers to be deactivated and the empty channels scrutinized for any tell-tale signals of crosstalk resulting from any fluorophores excited by the remaining active laser [97]. In one instance, we found that the solid-state 550-nm laser produced a red-channel signal (phospho-ERK1/2) that bled through in the far-red channel (ChAT). Additional checks ruled out this as bleed-through from excitation crosstalk of the Cy3 and Alexa-647 fluorophores. Rather, the bleed-through was due to emission crosstalk for the filters configured on the microscope itself. Therefore, to eliminate bleed-through caused by this cross-talk within the configured workflow, the sequence for photographing/scanning triple-labeled material was altered so that the 488-nm and 555-nm lasers performed their sequential scans for the first two channels, and the tissue was photographed in the far-red channel separately.

2.7 Spatial analyses and tabulation

2.7.1 Sampled regions. For this initial characterization of immunofluorescent labeling patterns in saline- and 2-DG-treated subjects, we sampled selected regions in the *rhombic brain (His, 1893)* [21] (RB) at three selected rostrocaudal levels **(Figure 1)**. Specifically, the tissue sections we examined were sampled at inferred anteroposterior stereotaxic coordinates of –9.80 mm from Bregma (β) (corresponding to Level 51 of BM4.0), –13.44

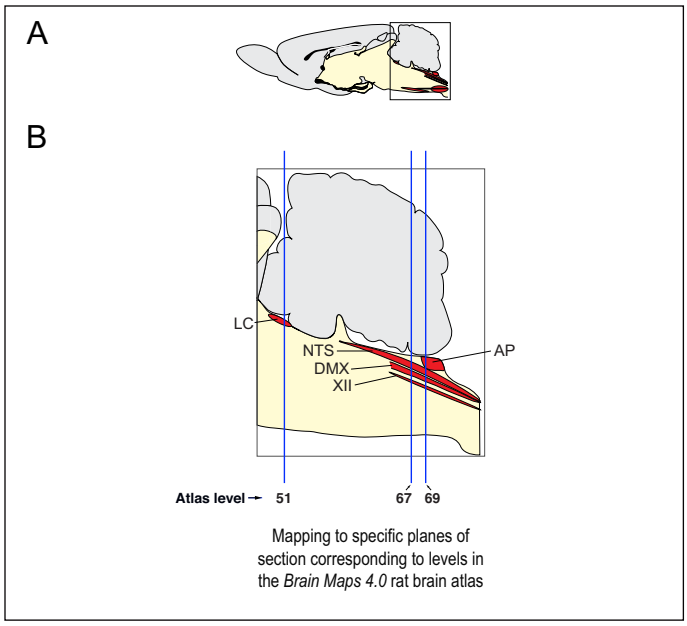

Figure 1. Overview of tissue sampling employed for the experimental dataset. **(A)** A sagittal-plane view of the rat brain, adapted from the *Brain Maps 4.0 (BM4.0)* open-access rat brain atlas [82], which is the spatial model we used in this study. **(B)** An enlargement is presented of the boxed outline shown in **(A)**, which provides details concerning the portions of the *rhombic brain (His, 1893)* [21] (RB) we studied (*shaded in red*). These include the *locus ceruleus (Wenzel & Wenzel, 1912)* [83] (LC), *area postrema (>1840)* (AP), *nucleus of solitary tract (>1840)* (NTS), *dorsal motor nucleus of vagus nerve (>1840)* (DMX), and *hypoglossal nucleus (>1840)* (XII). Portions of these structures were identified in tissue sections as closely registered to specific atlas levels from the *BM4.0* reference (*shown as vertical blue lines*). See the methods section for details.

mm from β (Level 67), and –13.76 from β (Level 69). Our analyses included observations of immunofluorescent patterns in portions of the *locus ceruleus (Wenzel & Wenzel, 1912)* [83] (LC), *area postrema (>1840)*, *nucleus of solitary tract (>1840)* (NTS), *dorsal motor nucleus of vagus nerve (>1840)* (DMX), and *hypoglossal nucleus (>1840)* (XII).

2.7.2 Plane-of-section analysis, regional parcellations and atlas level assignments. To determine whether the tissue sections were at the rostrocaudal locations that corresponded to the atlas levels we aimed to sample, we performed a plane-of-section analysis for each tissue section collected. We have briefly reported on this type of analysis for Fos-immunoreactive tissue under conditions of fasting and re-feeding [100], and note here additional details germane to the present study (for a more thorough review of this topic, please consult Simmons & Swanson [101]).

First, all *R series* tissue was evaluated for its suitability to help determine cytoarchitectonic boundaries by documenting the condition of each tissue section on a spreadsheet. Sections deemed suitable for use were photographed as described in *Section 2.6.1*. Team members (GPT, JSP) provisionally assigned an atlas level to the section by closely examining and documenting the nearest-neighbor spatial relations of identifiable cell groups in the *R series* photomicrographs and compared these with regions within the *Brain Maps 4.0* atlas. The criteria used to assign a given region of interest (ROI) in a tissue section to a specific atlas level is detailed below (*Sections 2.7.2.1–2.7.2.3*). In situations where two-closely spaced sections corresponded to the same atlas level, only one of the sections was deemed the best to represent distribution patterns for that atlas level (*i.e.*, only one section and its labeling patterns were used to map patterns to that particular level).

Once initial assignments were made to all *R series* photomicrographs, they were migrated into Adobe Illustrator (AI) 2022 and annotated manually. A transparent data layer overlay was created for each photomicrograph and boundaries were drawn around relevant cell groupings identifiable in the Nissl-stained patterns. The left and right sides of the sections were also carefully noted to allow for accurate registration of Nissl-defined boundaries with tissue series processed for immunofluorescence. This was achieved by recording asymmetry in the shapes of the tissue hemispheres, especially in certain key areas (*e.g.*, area between the pyramidal tracts; cross-sectional

profiles of ventrally-located blood vessels investing the tissue). In the progress of performing these annotations and parcellations, team members revisited the tabulation of the original atlas assignments and, when deemed necessary, revised them on the basis of their improved familiarity with the spatial characteristics of the tissue. This iterative process, which is crucial to allow ample time for and which is necessary to ensure both accuracy and precision, is noted here as a critical part of this workflow. For instances where a Nissl-stained section was missing or damaged and could not be used to gather information to help with plane-of-section analysis and atlas level assignments, the chemoarchitecture of the fluorescently-labeled tissue series and its associated fiducials were used instead. In some cases, visualization of the fluorescently-labeled tissue section under dark-field illumination was sufficient to provide team members with important fiducials to make the determinations needed. Below, the specific criteria and considerations used to determine correct spatial context for each ROI is noted.

2.7.2.1 Determining atlas level 51. The *locus ceruleus (Wenzel & Wenzel, 1912)* [83] (LC) is a highly-compact cell group of obliquely arranged neurons that lie adjacent to the *floor of fourth ventricle (Reil, 1807–1808)* [102] (V4f), medial to the *midbrain nucleus of trigeminal nerve (>1840)* (MEV), and ventromedial to the *parabrachial nucleus (>1840)* (PB); and is situated in the larger *pontine central gray general (Swanson, 2004)* [103] (PCGg). The adjacent cytoarchitecture of the MEV and the myeloarchitecture of the *superior cerebellar peduncle (Procháska, 1800)* [104] (scp), a fiber tract dividing the PB subnuclei, were key landmarks for determining atlas level and accurate comparison of this region between sections of different brains. In rostral portions of the LC, the cell group was observed to tightly wrap around the lateral border of the *fourth ventricle, principal part (Swanson, 2018)* [71] (V4), then to slightly separate from the margin ventrally in more caudal segments (as depicted in atlas level 51).

The overall shape and height of V4 are also useful indicators of atlas level; however, these are less reliable when dorsal-ventral tilt during sectioning is a known issue, which can elongate or shorten the height of ventricular space in the tissue section. Due to a significant distance between the left and right sides of the region, medial–lateral tilt during sectioning can result in atlas assignment asymmetry between the two sides of the section. In some cases, the plane of section prevented the team member from selecting both left and right-side LC regions, since one of them fell before or after level 51. LC cell groups with a regional boundary that closely matched the LC boundary delineation at atlas level 51 were analyzed. LC ROIs that were determined to be more rostral or caudal than atlas level 51 were not considered here.

The team member marked the brightly-fluorescing perikaryon profiles that had a clearly visible nucleus or closely resembled a segment of a neuron that was consistent in appearance with the cellular morphology of the LC [105]. A perikaryon profile was identified as double-labeled if it appeared yellow in the merged-channels image or, if this was not clear due to one channel obscuring the other, then if it also appeared in both single-channel images. A labeled profile was determined to display only pERK1/2 immunoreactivity or only DBH immunoreactivity by confirming the absence of signal in the other channel for that profile.

2.7.2.2 Determining atlas level 67. Rostrally, towards what would be *BM4.0* levels 64 and 65, the chemoarchitecture of the *nucleus of solitary tract (>1840)* (NTS) and *dorsal motor nucleus of vagus nerve (>1840)* (DMX) overlap and they appear to share a ventromedial border. Further caudally, however, at atlas level 67, the chemo- and cytoarchitecture of the NTS and DMX are more clearly discernible from one another. The V-shaped *floor of fourth ventricle (Reil, 1807–1808)* [102] (V4f) in this area can be a diagnostic fiducial for comparing these dorsomedially-situated structures between tissue sections. The ventricular opening is much more confined at level 68 as the wider space at level 67 narrows caudally into the *central canal (Bellingeri, 1823)* [106] (C). The *hypoglossal nucleus (>1840)* (XII) neighbors the DMX medially, and its large motor neurons could be identified by ChAT immunolabeling. Moreover, the proximity of XII neurons to those of the DMX were indicative of atlas level, since the borders of the XII and DMX are closer at 67 than at more rostral atlas representations.

The DBH-labeled axonal fibers, in contradistinction, appeared to confine themselves primarily within the borders of the *nucleus of solitary tract, medial part (>1840)* (NTSm) and were used in combination with the descending white matter fibers of the *solitary tract (>1840)* (ts), to localize the NTSm when an adjacent Nissl-stained section was not used. A few stray DBH+ fibers and an occasional DBH+ perikaryon profile were

observed lateral to the descending ts fibers; note, however, that we did not include the *nucleus of solitary tract, lateral part (>1840)* (NTSl) in our mapping analysis, but general observations of labeling in this structure were recorded. The reviewer marked each brightly-fluorescing small- to moderately-sized perikaryon profile of the NTS that contained a visible nucleus. Less vibrant or slightly out-of-focus profiles were marked by the reviewer if the perikaryon profile was distinguishable or if the labeled elements displayed features of the other clearly-identifiable DBH-labeled perikaryon profiles, such as a similar perikaryal size or long axonal extensions.

2.7.2.3 Determining atlas level 69. Atlas level 69 was determined, in the main, by the presence of the *area postrema (>1840)* (AP) dorsal to the DMX and NTS. At level 69, the AP extends laterally and is mostly flat along its dorsal border. At this level, the DMX presents as a large, blimp-shaped cell group that decreases in cellular area and vertically flattens in more caudal representations. Proceeding caudally, the AP takes on a rounder shape as it reduces in size and this shape is a reliable visual cue for the determination of a rostral or caudal AP-containing section. Perikaryon profiles were carefully marked along the border of the NTS and AP so as to not include those found in the AP in our analysis of the NTS.

2.7.3 Standardized mapping. Images of immunolabeled tissue sections were imported into Adobe Illustrator (AI) and aligned precisely with the data layer containing the photomicrograph of the corresponding adjacent *R series* Nissl-stained tissue section that served as a cytoarchitectural reference (*described in Sections 2.4.1 and 2.5*). Region boundaries that had been drawn over the Nissl-photograph data layer were then superimposed on the underlying fluorescence image, enabling each image set to be registered to the proper level of the *Brain Maps 4.0 (BM4.0)* open-access atlas [71].

To plot immunolabeled elements onto *BM4.0* atlas templates in AI, fluorescently-labeled fiber tracts and perikaryon profiles were traced and marked with circles and line segments, respectively on a separate data layer. If these representations shared a common region boundary (*i.e.*, if they were all within the same region), they were grouped together in their layer. This layer was then copied and pasted as a collective set of drawn elements into an underlying data layer containing the corresponding atlas level template with the corresponding brain region. This import of drawn elements was achieved by aligning the grouped elements to be in as close of a registration as possible with the bounded regions on the map. Alignments generally consisted of rotating the drawn patterns to orient correctly with the map's regional boundaries. In this manner, maps of the DBH-, ChAT-, and phospho-ERK1/2-immunoreactive signals were created for each subject. As team members became more proficient in recognizing the cytoarchitecture of RB cell groups and their morphological variability, revised maps were generated in cases where an alternate section was determined to be a better representation of the atlas level. Previous maps were thus reworked or re-created when it was decided that they inaccurately represented the numbers of cells displaying signal or which had an erroneous atlas level assignment.

2.7.4 Region-delimited quantitation and assessment of signal co-localization.

2.7.4.1 Rationale for counting methods. A few points regarding our counting procedures are noted here. First, in keeping with recommendations furnished by Saper [107], we note here our reasons for choosing the particular counting procedures we employed in this study. The goal of our counting efforts was not to provide an unbiased, global estimate of cell population size within any particular brain structure. Nor was it to provide a formal stereological assessment of absolute cell counts or densities. Rather, the goal was to compare the presence of the cellular activation marker, phospho-ERK1/2, in portions of brain regions with a defined rostrocaudal location and a fairly uniformly-comparable set of cytoarchitectonic boundaries between two experimental groups. Thus, we placed deliberate constraints upon our analysis by selecting regions of interest (ROIs) based on cytoarchitectonic criteria. By doing so, we could perform counts on comparable rostrocaudal levels between groups. Thus, the cytoarchitecture – constrained by plane-of-section analysis and Nissl-/chemoarchitecture-based criteria – was the primary informer of the ROI boundaries we used between groups to perform counts.

Second, the counts in our study are, strictly speaking, those of cell profiles, rather than cells themselves, since approaches used here cannot determine whether the total numbers of profiles sampled correspond directly to total cell counts; indeed, the two metrics are rarely equivalent [108]. Nevertheless, given that the ROIs we compared between groups were constrained to similar locations along the anteroposterior axis and, therefore,

also had similar cytoarchitectural boundaries, we reasoned that the relative comparison between median profile counts (and not median cell counts per se) would still accurately reveal differences in cellular activation between treatments. To this end, we also corrected for oversampling errors in our profile counts, as described in *Section 2.7.4.3*.

2.7.4.2 Counting procedures. Immunolabeled perikaryon profiles were manually counted and annotated in a manner similar to that reported previously by one of us [66], but digital transparent overlays were utilized rather than acetate sheets affixed to printed hard copies of the images. Specifically, images of sections with ROIs corresponding to *BM4.0* atlas levels 51, 67, and 69 were opened in Adobe Illustrator (AI) 2022 and arranged into files containing the superimposed merged-channel and single-channel images, each in a separate layer. Two additional layers were created for the manual annotation of DBH- and pERK1/2-labeled perikaryon profiles.

To mark the locations of DBH-labeled perikaryon profiles, the reviewer made visible the layer containing the single-channel image corresponding to DBH immunofluorescence, and used the *Ellipse Tool* to place white-colored ellipses over labeled perikaryon profiles in the DBH layer. Keeping the layer containing DBH perikaryon profile markings visible, the team member toggled the single-channel pERK1/2 image on and off, determining if each DBH+ perikaryon profile was single or double-labeled based on the profile's visibility in one or both channels, respectively.

To record the double-labeled perikaryon profiles, the *Smart Guides* "snap-to-center" function in AI was used to place a black ellipse on exactly the centroid coordinate of the DBH+ profile marking on a 'pERK1/2 + DBH' sublayer of the 'pERK1/2' layer. When all co-labeled perikaryon profiles were identified in this manner, the pERK1/2 single-channel image was used to record profiles displaying only signal for pERK1/2 in a sublayer called 'pERK1/2 only'. For annotations of images corresponding to levels 67 and 69 of *BM4.0*, the ChAT immunolabel readily identified the cholinergic motor neurons of the DMX; thus, the reviewer did not include DBH+ or pERK1/2+ perikaryon profiles in the vicinity of the NTS that were also ChAT+.

To obtain the perikaryon profile counts, the layer or sublayer was selected and the number of objects within that layer was recorded. The number of pERK1/2 + DBH perikaryon profiles and pERK1/2-only profiles were added to determine the total number of pERK1/2-labeled profiles, and the number of pERK1/2 + DBH perikaryon profiles was subtracted from the total number of DBH+ profiles to determine the number of DBH-only profiles.

2.7.4.3 Correction of oversampling error. We adapted the method of Abercrombie [109] to correct for overestimation of our perikaryon profile counts. To perform this correction, we made two measurements: the cell diameter and section thickness. To measure cell diameter, two tissue sections representing two subjects from each treatment group were randomly selected for cell diameter estimation. As described in *Section 2.6.2*, images from these sections were captured using a ×20-magnification objective lens (Plan-Apochromat; N.A., 0.8) on our Zeiss AxioImager M.2 microscope and were examined within Volocity software. The Measurements tool within Volocity was used to measure cell type-specific profiles. Two perpendicular lines were drawn across the long and short diameters of each sampled perikaryon profile and the total line lengths (in µm) were recorded in a spreadsheet. Ten randomly-selected cell profiles were measured on each section and the average of the longer diameter of these cell profiles was used as an estimation of cell diameter. The mean perikaryal lengths were calculated for the DBH+ profiles of the LC and NTS, the non-DBH-expressing phospho-ERK1/2+ profiles in the NTS, and the ChAT+ profiles in the DMX.

Second, we used the ×100-magnification objective lens (U Plan S-Apo, oil; N.A., 1.40; working distance, 0.13 mm) on our Olympus BX63 system (*described in Section 2.6.1*) to determine the average thickness of our tissue sections after immunohistochemical processing was completed. To perform this measurement, we opened a live window in cellSense™ Dimension software and, under epifluorescence illumination, opened the fluorescence channel coding for DBH-immunoreactivity (either red or green, depending on the reaction sets summarized in **Table 1**). A group of DBH+ cells was brought into focus and the *z*-axis positions of the stage (in µm) provided by the software for the top- and bottom-most focal planes containing in-focus neurons were recorded and averaged between groups. The optical thickness of six tissue sections for each subject (n = 11) were recorded in this manner.

The average section thickness measures for each subject were pooled and averaged by treatment group (saline: n = 5 subjects; 2-DG: n = 6 subjects). With the above two measures now in hand, a cell-type correction factor was calculated for each ROI based on Abercrombie's formula [109]:

$$P = A(M/(L+M))$$

where P = the corrected profile counts, A = the raw profile counts, M = section thickness (in μm), and L = the average length of the perikaryon profile (in μm). The correction factors for each ROI were calculated for each subject and averaged for each treatment group. Perikaryon profile counts in the LC were corrected by multiplying total perikaryon profile counts with the DBH+ cell-type correction factor. Similarly, perikaryon profile counts of all the cell types in the DMX were corrected by multiplying total perikaryon profile counts with the ChAT+ cell-type correction factor. For the NTS, however, we observed a notable size difference between cell types. For example, at *BM4.0* level 69, the average NTS area estimations for DBH+ and pERK1/2+ single-labeled perikaryon profiles are 146 mm^2 and 96 mm^2, respectively. Thus, for the Abercrombie correction to be performed accurately, we estimated a weighted correction factor for each cell type based on the relative abundance of each cell type in the NTS. Once all data were corrected for across ROIs and subjects, the corrected perikaryon profile counts were the measures used for statistical analysis and graphical presentation.

2.7.5 Statistical analysis. The pERK1/2+, DBH+ and ChAT+ bilateral perikaryon profiles within the LC, NTSm and DMX were tallied on the sections corresponding to *BM4.0* atlas levels 51, 67, and 69. The average of the bilateral perikaryon profile counts [(left side counts + right side counts)/2] for each region, from each of the saline- and 2-DG-treated rats, was considered as a representative number of immunoreactive cells. The number of cells from each brain was used as a dependent variable, with saline or 2-DG treatment as the independent variable for statistical and exploratory data analyses. A Shapiro-Wilk test [110] was performed to determine the Gaussian distribution of the dependent variable in each treatment group. Phospho-ERK1/2+ perikaryon profile counts in the NTSm at levels 67 and 69 in 2-DG-treated rats did not meet the Gaussian distribution assumption at a *p*-value of 0.05. Since the distributions were not normal, and to be consistent throughout the study, non-parametric statistical tests were used to analyze all differences in profile counts across the sampled brain regions in this study.

Significance of the difference in the distributions of immunoreactive perikaryon profile counts between saline- and 2-DG-treated rats was analyzed for each region using the Wilcoxon Rank Sum test, with two-sided significance [111, 112]. A *p*-value less than or equal to 0.05 was considered statistically significant. False discovery rate was controlled by calculating Benjamini-Hochberg [113] adjusted *p*-values, with an FDR of 5% or below considered as statistically significant. Effect sizes were calculated and used to interpret the magnitude of the difference between saline- and 2-DG-treated subjects. Effect sizes of 0.1 to less than 0.3, 0.3 to less than 0.5, and greater than or equal to 0.5 were categorized as small, moderate, and large magnitudes, respectively. *RStudio* (R, version 3.6.2) [114] with *rstatix* [115] and *ggplot2* [116] packages were used for statistical analysis and to construct box plots and pie charts.

3. Results

The results of this study are divided into two main parts. First, rostral *Rhombic brain (His, 1893)* [21] (RB) data for saline- and 2-DG-treated subjects are presented, specifically for the *locus ceruleus (Wenzel & Wenzel, 1912)* [83] (LC). Second, caudal RB data are considered; similarly comparing labeling patterns for the two groups for the *nucleus of solitary tract (>1840)* (NTS) and *dorsal motor nucleus of vagus nerve (>1840)* (DMX). For each part, individual subjects are first showcased to focus on paired comparisons of histological results, individual patterns of immunoreactivities in atlas maps, and morphological considerations of the signals. This is followed by group-level statistical comparisons of immunoreactive perikaryon profile counts between saline- and 2-DG-treated subjects and specific measures of cellular co-localization of immunoreactive signals.

3.1. Cellular activation profiles in the LC for saline- and 2-DG-treated subjects

3.1.1 Representative results in single pairs of subjects.

3.1.1.1 Phospho-ERK1/2-immunoreactive patterns mapped to Level 51. **Figure 2** shows the mapped distributions of phospho-ERK1/2-immunoreactive neurons in a portion of the LC that we sampled from subjects

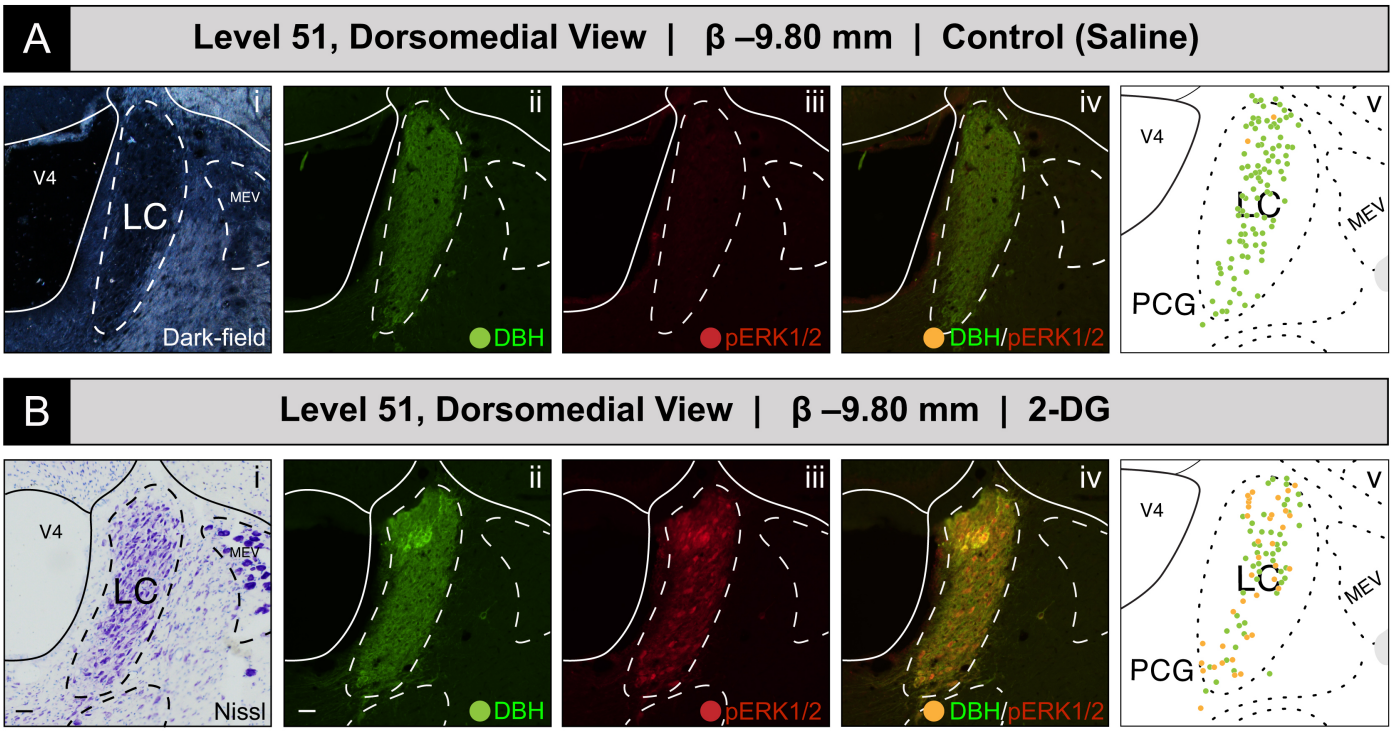

Figure 2. Increased recruitment of *locus ceruleus (Wenzel & Wenzel, 1912)* [83] (LC) neurons 15 min after intravenous 2-deoxy-D-glucose (2-DG) administration, as deduced from a comparison of LC perikaryon profiles in coronal-plane tissue sections from saline- **(A)** and 2-DG-treated **(B)** subjects. **(A, i–iv)**: Subject K10-012 (saline-treated). The LC of the right hemisphere, as visible in a dark-field image **(A-i)**, was immunostained for DBH (*green*; **A-ii**) and for the activation marker, phospho-ERK1/2 (*red*; **A-iii**), but displayed virtually no signal for the latter molecule. **(B, i–iv):** Subject K10-026 (2-DG-treated). In contrast, this subject displayed robust phospho-ERK1/2-immunoreactive signal in the LC **(B-iii)**, the boundaries of which were determined using a Nissl-stained tissue section from an adjacent tissue series collected from the same subject (bright-field photomicrograph shown in **B-i**). The maps in **A(v)** and **B(v)** are maps of the LC from the *BM4.0* reference atlas [82]. Scale bars in **A-i/B-i** and **A-ii/B-ii** each mark 20 µm, and apply to the rest of the photomicrographs shown in this figure. Note for **A-i** that the dark-field image of the same tissue reacted with immunofluorescence was used to identify boundaries for the LC in the brain of subject K10-012, rather than an adjacent Nissl-stained section, which was damaged during tissue processing.

---

receiving intravenous saline or 2-DG injection. To identify the appropriate rostrocaudal locations of the tissue sections in both groups, we were guided by fiducial landmarks within the tissue, either visualized in the same section under dark-field illumination **(Fig. 2A-i)**, or within a thionine-stained section from an adjacent series of tissue collected from the same subject (*i.e.*, *R series*; *see Methods*) **(Fig. 2B-i)**. The reference tissue allowed us to map the locations of the profiles observed in the fluorescence images to Level 51 of the *BM4.0* atlas [82]. Saline treatment was not associated with an appreciable number of phospho-ERK1/2+ perikaryon profiles in the LC **(Fig. 2A-iii)**. In contrast, a robust elevation in the numbers of phospho-ERK1/2+ perikaryon profiles was observed following 2-DG treatment **(Fig. 2B-iii)**. Virtually all of the phospho-ERK1/2 immunoreactivity appeared to be within DBH-immunoreactive neurons **(Fig. 2B-iv)**, a cellular phenotype well-documented to be abundant in this structure (*e.g.*, [105, 117–121]); these double-labeled perikaryon profiles were mapped as *gold-colored* circle glyphs on the corresponding atlas map **(Fig. 2B-v)**. At this level for this subject, all phospho-ERK1/2+ profiles appeared to be double-labeled for DBH-immunoreactivity, since none appeared to contain only the single label for phospho-ERK1/2 alone.

3.1.1.2 Phospho-ERK1/2+ and DBH+ perikaryon profiles at other levels of the LC. Although we did not formally chart patterns of immunoreactivity to *BM4.0* atlas templates for tissue sections containing the LC at levels other than Level 51, we did observe phospho-ERK1/2+ profiles throughout the LC at all rostrocaudal levels containing this structure, primarily within 2-DG-treated subjects. For example, for another 2-DG-treated subject (#K10-027), perikaryon profiles in the LC again showed robust immunoreactivity for the activation marker in tissue sections just caudal to that mapped at Level 51 **(Figure 3)**. Specifically, at a rostrocaudal location that maps

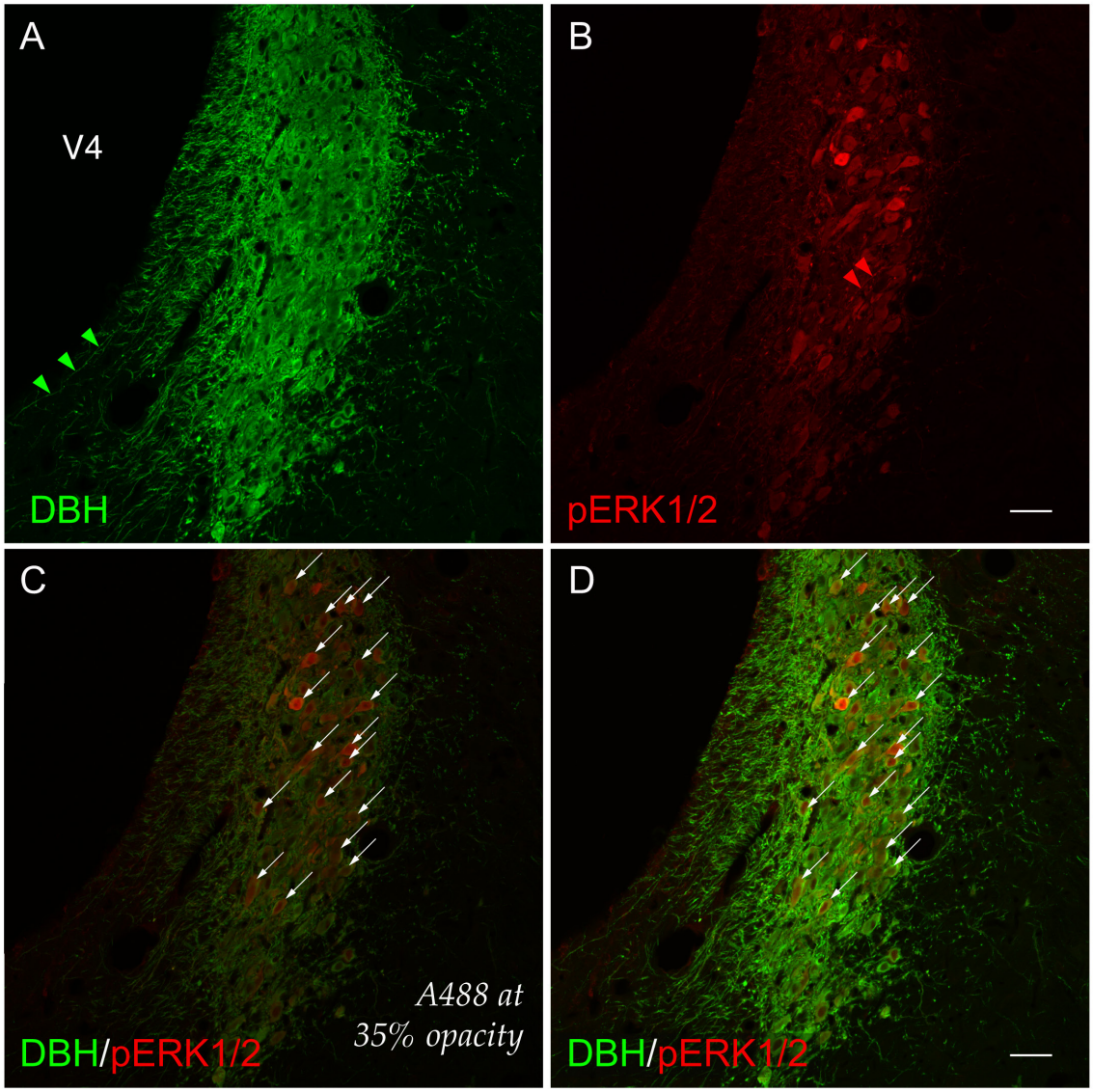

Figure 3. A higher-magnification view (cf. Fig. 2) of cellular activation observed in the *locus ceruleus (Wenzel & Wenzel, 1812)* (LC) [83] 15 min after 2-DG administration. Subject K10-027. **(A)** LC perikaryon profiles labeled for dopamine β-hydroxylase (DBH, *green*), and **(B)** phospho-ERK1/2 (pERK1/2, *red*) appear to co-label the same perikaryon profiles (**D**, *arrows*). **(C)** Co-labeled perikaryon profiles in the LC (identically marked by *arrows* as in **D**) with the A488 (*green*) channel set at 35% opacity renders visible the subtle, graded activation profiles of phospho-ERK1/2+ signal. *Arrowheads* (*green* in **A**; *red* in **B**) mark single-labeled neurites immunoreactive for DBH or pERK1/2, respectively. Scale bars in **B and D** mark 50 μm and apply to all photomicrographs.

~480 μm further caudally to a tissue plane that falls between *BM4.0* atlas levels 52 and 53, phospho-ERK1/2+ perikaryon profiles were again evident, especially in those situated dorsally within the structure **(Fig. 3B)**. Viewed under the higher power of a ×20 magnification objective lens and captured as a single-plane confocal scan, the DBH-immunoreactive signal could be observed within perikarya and neurite extensions, as has been reported by others [117–121]. Some of these neurites were oriented in parallel to the lateral margin of the *fourth ventricle principal part (Swanson, 2018)* (V4) **(Fig. 3A)**. Although double-labeled perikaryon profiles are evident at this level **(Fig. 3D)**, the relative abundance, brightness and saturation of the Alexa-488 fluorescence swamped the dimmer Cy3 signal of the phospho-ERK1/2 immunoreactivity in these profiles. These patterns were more readily observable if the opacity of the Alexa-488 signal was set to 35% without altering the Cy3 signal (**Fig. 3C**; compare profiles marked by arrows in panels **C** and **D**). In the double-labeled neurons, the presence of phospho-ERK1/2 immunoreactivity in the nuclear compartment of some perikarya was clearly evident, with a notable absence of fluorescent signal marking the presence of the nucleolus in many of these profiles **(Fig. 3D)**.

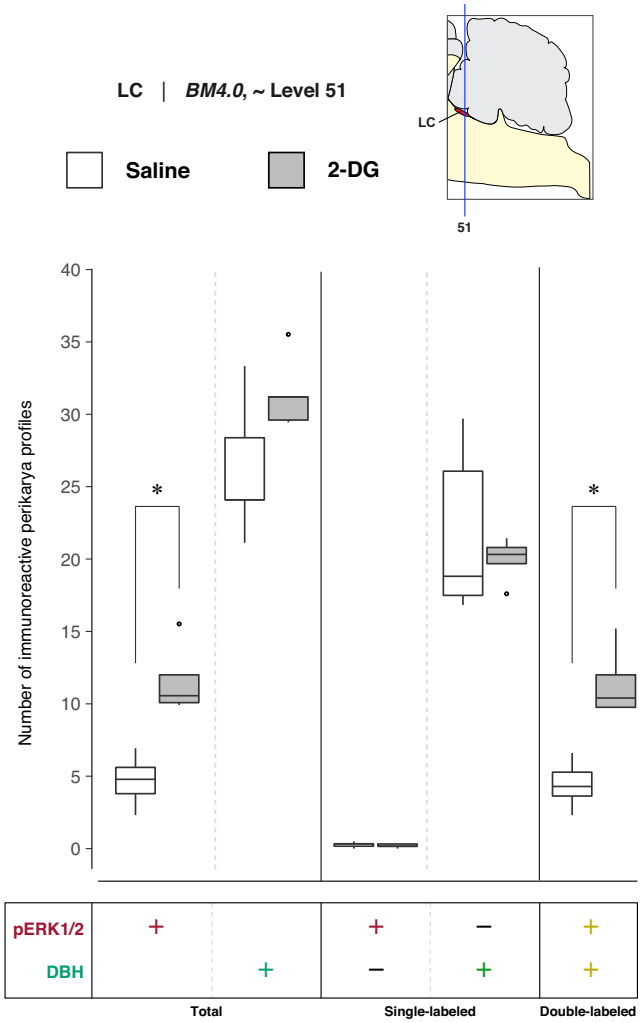

Figure 4. Increased recruitment of *locus ceruleus (Wenzel & Wenzel, 1812)* (LC) [83] neurons 15 min after 2-DG administration. Abercrombie-corrected [109] perikaryon profile counts from both saline- and 2-DG-treated subjects are represented as box plots displaying the total numbers of phospho-ERK1/2- or DBH-immunoreactive profiles, or only the single- and double-labeled profiles, from tissue sections identified to be in register with *BM4.0* atlas level 51 (map, *upper right*). An asterisk (*) denotes statistical significance between groups, FDR-adjusted $p < 0.05$. See **Tables 2 & 3** for details.

3.1.2 Group-level effects of saline versus 2-deoxy-D-glucose administration on LC activation

3.1.2.1 Quantitative analysis of LC activation. To determine LC activation in association with saline and 2-DG treatments, pERK1/2- and DBH-immunoreactive perikaryon profiles were counted in the LC at *BM4.0* atlas level 51 for all subjects. **Figure 4** shows box plots of Abercrombie-corrected phospho-ERK1/2+ and DBH+ perikaryon profile counts and **Table 2** presents the descriptive statistics of our quantitative analysis.

Median numbers of phospho-ERK1/2-immunoreactive profiles in saline and 2-DG groups were 15 and 33, respectively **(Table 2)**, and the distributions in the two groups differed significantly (Wilcoxon statistic = 25, $n_1 = n_2 = 5$, FDR-adjusted $p < 0.05$; **Table 3**). Specifically, the number of pERK1/2-immunoreactive profiles displayed in the LC was significantly elevated for 2-DG- compared to saline-treated rats (**Fig. 4**, 'total' column (pERK1/2: +); FDR-adjusted $p < 0.05$; effect size: large; **Table 3**). Similarly, median numbers of double-labeled profiles in saline and 2-DG groups were 13 and 33, respectively **(Table 2)**, with distributions in the two groups that again were significantly different (Wilcoxon statistic = 25, $n_1 = n_2 = 5$, FDR-adjusted $p < 0.05$; **Table 3**). Thus, the double-labeled counts of LC profiles of 2-DG rats were elevated significantly compared to those of saline-treated rats (**Fig. 4**, 'double-labeled' column (pERK1/2, DBH: both +); effect size: large; **Table 3**). In contrast, there were no statistically significant differences in DBH perikaryon profile counts between saline- and 2-DG-treated rats

Table 2. Summary of descriptive statistics for LC perikaryon profiles at Atlas Level 51

Region	Cell phenotype	Saline				2-DG			
		n	Median	Q1	Q3	n	Median	Q1	Q3
LC (~51)	pERK1/2^{+}	5	14.5	11.5	17	5	33	31.5	37.5
	DBH^{+}	5	73	73	86	5	97.5	92.5	97.5
	pERK1/2^{+} & DBH^{-}	5	1	0.5	1	5	0.5	0.5	1
	pERK^{-} & DBH^{+}	5	57	53	79	5	63.5	61.5	65
	pERK^{+} & DBH^{+}	5	13	11	16	5	32.5	30.5	37.5

Table 3. Summary of non-parametric test statistics and effect sizes for LC perikaryon profiles at Atlas Level 51

Region	Cell phenotype	Sample size		Wilcoxon Rank-Sum test			Wilcoxon effect size	
		Saline	2-DG	Test statistic	*p*-value	FDR-adjusted *p*-value	Effect size	Magnitude*
LC (~51)	pERK1/2^{+}	5	5	25	**0.01**	**0.03**	**0.83**	large
	DBH^{+}	5	5	21	0.09	0.22	0.56	large
	pERK1/2^{+} & DBH^{-}	5	5	6.5	0.24	0.45	0.40	moderate
	pERK1/2^{-} & DBH^{+}	5	5	14	0.83	0.45	0.10	small
	pERK1/2^{+} & DBH^{+}	5	5	25	**0.01**	**0.03**	**0.83**	large

* 0.1 to < 0.3 – small, 0.3 to < 0.5 – moderate, and > or = 0.5 – large

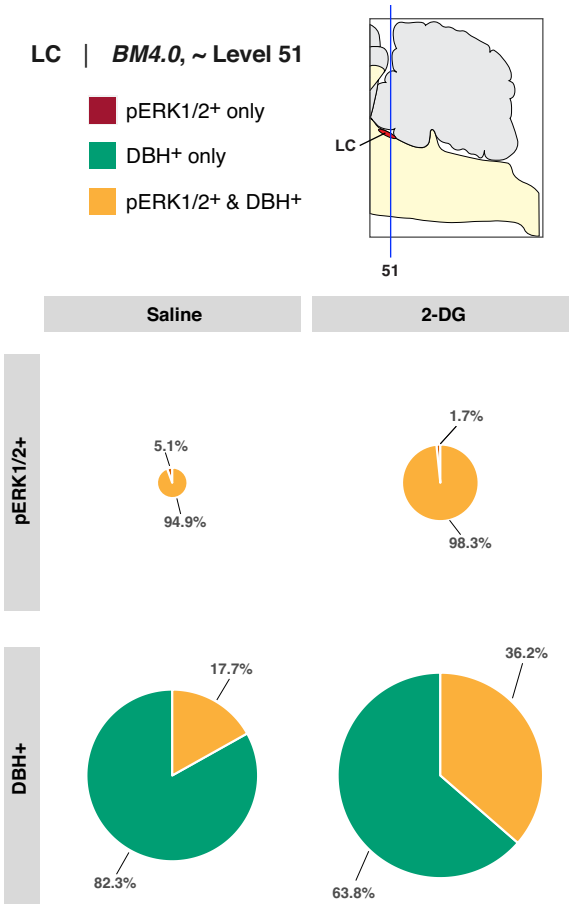

Figure 5. Relative percent differences of perikaryon phenotypes in *locus ceruleus (Wenzel & Wenzel, 1912)* [83] (LC) region in saline- and 2-DG-treated subjects. Relative percentages of single- and double-labeled perikaryon profiles were calculated for pERK1/2+ (*top row*) and DBH+ (*bottom row*) cell types in each treatment group and displayed as pie charts. Charts are paneled with treatment group as column and perikarya type as row. The size of each pie chart was scaled according to its corresponding total Abercrombie-corrected [109] perikaryon profile number. For example, the 2-DG group pERK1/2+ pie chart (*top right panel*) has a larger diameter than the saline group pERK1/2+ pie chart (*top left panel*), corresponding to the Abercrombie-corrected perikaryon profile numbers presented in **Figure 4**. Note the similarity in the yellow-colored portion of the pie, in terms of relative proportions to the whole, in the top row between treatment groups.

(**Fig. 4**, 'total' column (DBH: +) and 'single-labeled' column (DBH: +, pERK1/2: –); see also **Table 3**). **Figure 4** shows the statistical comparisons between saline- and 2-DG-treated animals for neurons displaying phospho-ERK1/2 in the LC.

3.1.2.2 Relative differences in the numbers of DBH-immunoreactive perikarya in the LC of saline- and 2-DG-treated subjects. To determine whether 2-DG treatment was associated with changes in the numbers of DBH-immunoreactive neurons in the LC, the relative percentages of Abercrombie-corrected single (pERK1/2+ only or DBH+ only) and double-labeled (pERK1/2+ & DBH+) perikaryon profiles were calculated for saline and 2-DG groups, and visualized as pie charts in **Figure 5**. Consistent with our microscopic observations, a majority of the pERK1/2+ perikaryon profiles in LC were identified to be DBH+ in both saline- (94.9%) and 2-DG-treated (98.3%) rats (**Fig. 5**, pERK+ row, pERK1/2+ & DBH+; *yellow-colored fraction*). For the total numbers of DBH+ perikaryon profiles, a higher percentage of pERK1/2+ profiles were observed in the LC of 2-DG- (36.2%) than saline-treated (17.7%) rats (**Fig. 5**, DBH+ row, pERK1/2+ & DBH+, *yellow-colored fraction*).

3.2. Cellular activation profiles in the NTS and DMX for saline- and 2-DG-treated subjects

3.2.1 Representative results in single pairs of subjects at atlas level 67

3.2.1.1 Phospho-ERK1/2-immunoreactive patterns mapped to Level 67. **Figure 6** shows the mapped distributions of phospho-ERK1/2-immunoreactive signal in activated NTS and DMX neurons following saline or 2-DG administration. Saline treatment was not associated with a substantial amount of phospho-ERK1/2-immunopositive perikaryon profiles in the NTS at Level 67 **(Fig. 6A-iii)**. In comparison, 2-DG treatment was associated with a marked increase in phospho-ERK1/2 immunoreactive perikaryon profiles within the NTSm **(Fig. 6B-iii)**. This elevation correlated to both single-labeled phospho-ERK1/2 profiles and those double-labeled for DBH-immunoreactivity **(Fig. 6B-vi)**, that were represented as *red- and yellow-colored circle glyphs*, respectively, on the corresponding atlas map **(Fig. 6B-v)**.

ChAT-immunopositive neurons in the DMX, depicted in *blue*, displayed low levels of basal activation in saline-treated subjects **(Fig. 6A-vii)**, and appear as *magenta circles* on the atlas maps when also immunoreactive for phospho-ERK1/2. Activity levels in the DMX were elevated following 2-DG treatment **(Fig. 6B-vii)**, although not to a significant degree; however, intensity of the phospho-ERK1/2 immunoreactive signal appeared to be more prominent in 2-DG-treated subjects. In some instances, ChAT-labeled perikaryon profiles were observed to also be DBH-immunopositive, shown as *neon green circles*, and represented as *black circles* when immunoreactive for all three markers. In contrast, no phospho-ERK1/2 immunoreactivity was observed in the *hypoglossal nucleus (>1840)* (XII), and few or no DBH-immunoreactive fibers were observed within the *nucleus of solitary tract, lateral part (>1840)*.

3.2.2 Group-level effects of saline versus 2-deoxy-D-glucose administration on NTS and DMX activation at BM4.0 Atlas level 67

3.2.2(a) Quantitative analysis of NTS activation at level 67. To determine NTS activation in association with saline and 2-DG treatments, pERK1/2- and DBH-immunoreactive perikaryon profiles were counted in the NTS at BM4.0 atlas level 67 for all subjects (n_{saline}= 6, $n_{2\text{-}DG}$= 5). **Figure 7** shows box plots of Abercrombie-corrected phospho-ERK1/2+ and DBH+ perikaryon profile counts. **Table 4** presents the descriptive statistics of our quantitative analysis and test statistics of all the comparisons are presented in **Table 5**.

Median numbers of pERK1/2-immunoreactive profiles in saline and 2-DG groups were 1.7 and 6.1, respectively **(Table 4)**, and the distributions in the two groups differed significantly (Wilcoxon statistic = 30, FDR-adjusted $p < 0.05$; **Table 5**). The number of pERK1/2-immunoreactive profiles within the NTS significantly increased following 2-DG treatment as compared to saline-treated controls (**Fig. 7**, 'total' column (pERK1/2: +); FDR-adjusted $p < 0.05$; effect size: large; **Table 5**). The median numbers of double-labeled profiles in saline and 2-DG groups were 0.2 and 1.9, respectively **(Table 4)**, that maintained significantly different distributions between groups (Wilcoxon statistic = 29, FDR-adjusted $p < 0.05$; **Table 5**). The elevated counts observed in 2-DG-treated rats translated across single- (**Fig. 7**, 'single-labeled' column (pERK1/2: +, DBH: –); FDR-adjusted $p < 0.05$; effect size: large; **Table 5**) and dual-labeled perikaryon profile counts (**Fig. 7**, 'double-labeled' column

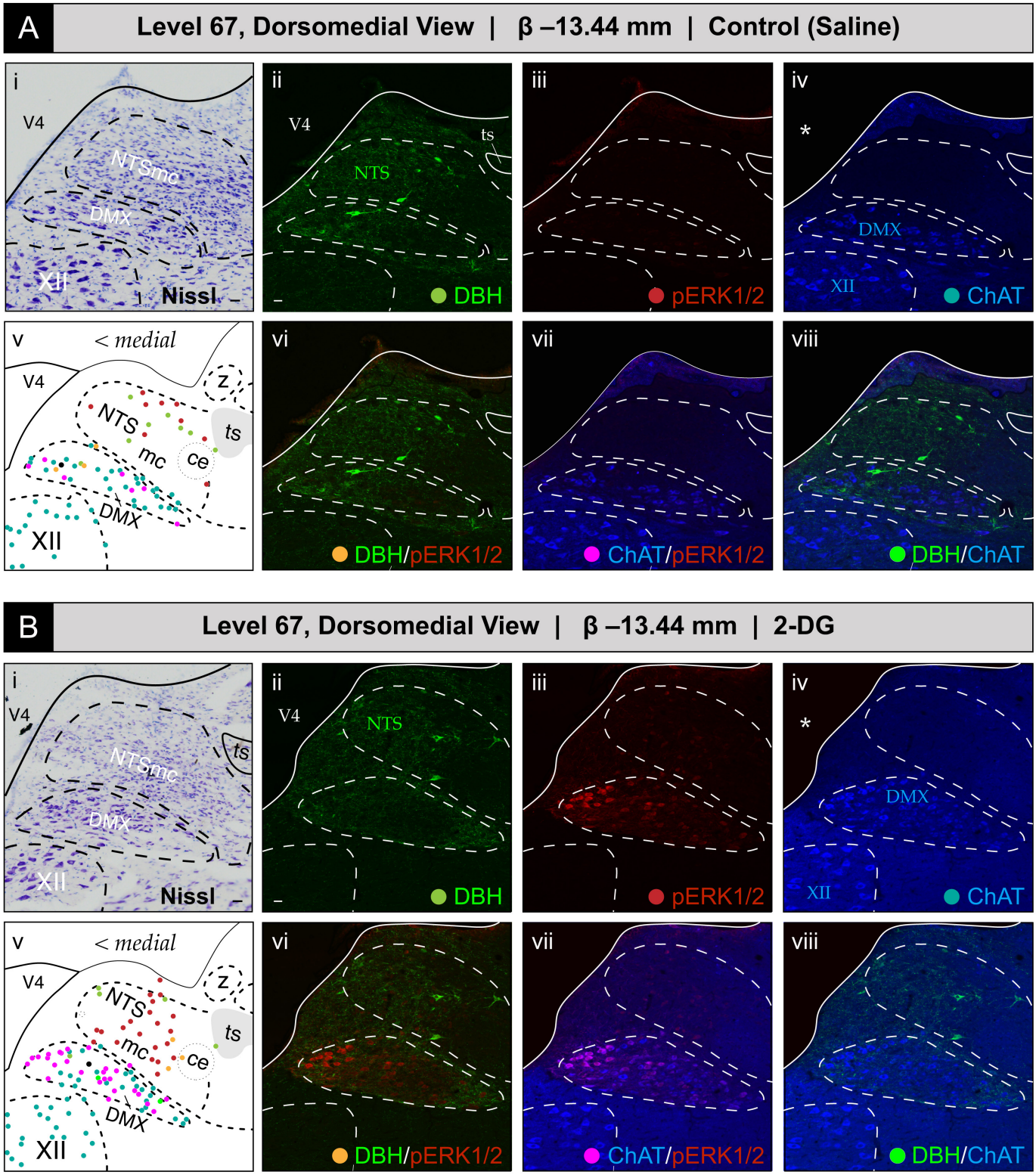
A
Level 67, Dorsomedial View | β –13.44 mm | Control (Saline)
i
V4
NTSmc
DMX
XII
Nissl
ii
V4
ts
NTS
DBH
iii
pERK1/2
iv
*
DMX
XII
ChAT
v
< medial
V4
z
NTS
ts
mc
ce
DMX
XII
vi
DBH/pERK1/2
vii
ChAT/pERK1/2
viii
DBH/ChAT
B
Level 67, Dorsomedial View | β –13.44 mm | 2-DG
i
V4
ts
NTSmc
DMX
XII
Nissl
ii
V4
NTS
DBH
iii
pERK1/2
iv
*
DMX
XII
ChAT
v
< medial
V4
z
NTS
ts
mc
ce
DMX
XII
vi
DBH/pERK1/2
vii
ChAT/pERK1/2
viii
DBH/ChAT

Figure 6 (*on previous page*). Glycemic challenge is associated with the recruitment of dorsal *medulla (Winslow, 1733)* [37] (MY) neurons mapped to atlas level 67 of *Brain Maps 4.0 (BM4.0)* [82]. Cytoarchitecture- and chemoarchitecture-based spatial analysis of distributed phosphorylated MAP kinase (pERK1/2) signal within dorsal RB neurons at the level of the *nucleus of solitary tract (>1840)* (NTS) (Level 67 in the *BM4.0* rat brain atlas). **(A, B)** The panels display bright-field Nissl photomicrographs **(i)**, single- **(ii–iv)** and dual-channel **(vi–viii)** fluorescence images, and *BM4.0* atlas maps **(v)** for saline- **(A)** and 2-DG-treated **(B)** subjects of individual immunoreactivity patterns for dopamine β-hydroxylase (DBH, *green*), phospho-ERK1/2 (pERK1/2, *red*) and choline acetyltransferase (ChAT, *blue*). The patterns fall near and within the boundaries for the NTS, *dorsal motor nucleus of vagus nerve (>1840)* (DMX), and *hypoglossal nucleus (>1840)* (XII). Note that the NTS label is colored *green* to signify its boundary determination using the pattern of immunoreactivity observed for DBH in the green channel, and DMX and XII labels are colored *blue* to signify their boundary determinations using ChAT-immunoreactive signal in the far-red channel. Tissue is shown in the coronal plane. Scale bars in **(i)** and **(ii)**, which mark 20 µm, and the medial orientation noted for the maps in **(v)**, apply to all photomicrographs. *Asterisks* in **A-iv** and **B-iv** mark the locations of masks placed over the ventricular space using Adobe Photoshop, to cover visually-distracting autofluorescence observed under the far-red channel from the mounting medium; this mask is used for all images containing far-red (*blue-colored*) signal (thus, this also applies to **A-vii/viii** and **B-vii/viii**). Headers for **A** and **B** note the inferred anteroposterior stereotaxic coordinate, expressed as millimeters from the Bregma (β) skull suture. See the list of abbreviations at the end of this article for a description of those marked on the maps.

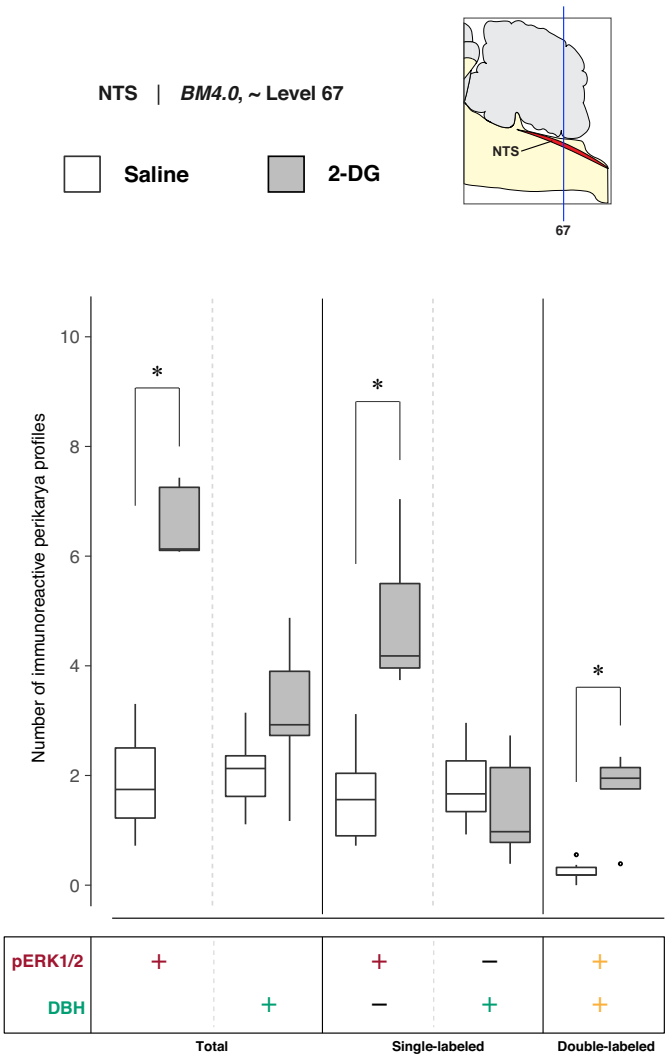

Figure 7. Increased recruitment of *BM4.0* atlas level 67-registered *nucleus of solitary tract (>1840)* (NTS) neurons 15 min after 2-DG administration. Abercrombie-corrected [109] perikaryon profile counts from both saline- and 2-DG-treated subjects are represented as box plots displaying the total numbers of phospho-ERK1/2- or DBH-immunoreactive profiles, or only the single- and double-labeled profiles, from tissue sections identified to be in register with *BM4.0* atlas level 67 (map, *upper right*). An asterisk (*) denotes statistical significance between groups, FDR-adjusted $p < 0.05$. See **Tables 4 & 5** for details.

Table 4. Summary of descriptive statistics for NTS and DMX perikaryon profiles at Atlas Level 67

Region	Perikarya phenotype	Saline				2-DG			
		n	Median	Q1	Q3	n	Median	Q1	Q3
NTS (~67)	pERK1/2^{+}	6	1.7	1.2	2.5	5	6.1	6.1	7.2
	DBH^{+}	6	2.1	1.6	2.3	5	2.9	2.7	3.9
	pERK1/2^{+} & DBH^{-}	6	1.6	0.9	2.0	5	4.2	4.0	5.5
	pERK1/2^{-} & DBH^{+}	6	1.7	1.3	2.3	5	1.0	0.8	2.1
	pERK1/2^{+} & DBH^{+}	6	0.2	0.2	0.3	5	1.9	1.7	2.1
DMX (~67)	pERK1/2^{+}	6	5.4	3.3	6.1	5	6.1	4.5	8.7
	ChAT^{+}	6	14.9	13.9	15.6	5	15.2	10.7	15.4
	DBH^{+}	6	0.3	0.2	0.3	5	0.9	0.7	1.0
	pERK1/2^{+}, ChAT^{-}, & DBH^{-}	6	0	0	0	5	0	0	0
	pERK1/2^{-}, ChAT^{+}, & DBH^{-}	6	9.4	8.1	10.7	5	6.5	5.2	8.5
	pERK1/2^{-}, ChAT^{-}, & DBH^{+}	6	0	0	0	5	0	0	0
	pERK1/2^{+}, ChAT^{+}	6	5.4	3.3	6.1	5	6.1	4.5	8.7
	pERK1/2^{+}, DBH^{+}	6	0	0	0	5	0	0	0
	ChAT^{+}, DBH^{+}	6	0.3	0.2	0.3	5	0.9	0.7	1.0
	pERK1/2^{+}, ChAT^{+}, & DBH^{-}	6	5.2	3.3	6.0	5	6.1	4.4	8.6
	pERK1/2^{-}, ChAT^{+}, & DBH^{+}	6	0.2	0.04	0.2	5	0.9	0.7	0.9
	pERK1/2^{+}, ChAT^{-}, & DBH^{+}	6	0	0	0	5	0	0	0
	pERK1/2^{+}, ChAT^{+}, & DBH^{+}	6	0.2	0.03	0.2	5	0.2	0	0.2

(pERK1/2: +, DBH: +); FDR-adjusted $p < 0.05$; effect size: large; **Table 5**). Saline- and 2-DG-treated rats did not significantly differ in the total DBH-immunoreactive profile counts (**Fig. 7**, 'total' column (DBH: +); see also **Table 5**).

3.2.2(b) Relative differences in the numbers of DBH-immunoreactive perikarya in the NTS at level 67 of saline- and 2-DG-treated subjects. To determine whether 2-DG treatment was associated with changes in the numbers of DBH-immunoreactive neurons in the NTS at level 67, relative percentages of Abercrombie-corrected single- (pERK1/2+ only or DBH+ only) and double-labeled (pERK1/2+ & DBH+) perikaryon profiles were calculated for saline and 2-DG groups and visualized as pie charts in **Figure 8**. In contrast to relative percentages observed in the LC at atlas level 51, the majority of the pERK1/2+ perikaryon profiles in the NTS at level 67 were identified to be DBH– in both saline- (86.9%) and 2-DG-treated (74%) rats (**Fig. 8**, pERK+ row, pERK1/2+ only; *maroon-colored fraction*). For total numbers of DBH+ perikaryon profiles, a higher percentage of pERK1/2+ profiles were observed in the NTS of 2-DG- (55%) than saline-treated (11.9%) rats (**Fig. 8**, DBH+ row, pERK1/2+ & DBH+; *yellow-colored fraction*).

3.2.2(c) Quantitative analysis of DMX activation at level 67 and relative differences in the numbers of DBH- and ChAT-immunoreactive perikarya. To determine DMX activation in association with saline and 2-DG treatments, pERK1/2-, ChAT-, and DBH-immunoreactive perikaryon profiles were counted in the DMX at *BM4.0* atlas level 67 for all but one subject (n_{saline}= 6, $n_{2\text{-}DG}$= 5; tissue for one 2-DG-treated subject, K10-008, was not available at this level). **Figure 9** shows box plots of Abercrombie-corrected phospho-ERK1/2+, ChAT+, and

Table 5. Summary of non-parametric test statistics and effect sizes for NTS and DMX perikaryon profiles at Atlas Level 67

Region	Perikarya phenotype	Sample size		Wilcoxon Rank-Sum test			Wilcoxon effect size	
		Saline	2-DG	Test statistic	*p*-value	FDR-adjusted *p*-value	Effect size	Magnitude*
NTS (~ 67)	pERK1/2$^+$	6	5	30	**<0.01**	**0.02**	0.83	large
	DBH$^+$	6	5	23	0.17	0.38	0.44	moderate
	pERK1/2$^+$ & DBH$^-$	6	5	30	**<0.01**	**0.02**	0.83	large
	pERK1/2$^-$ & DBH$^+$	6	5	10	0.41	0.67	0.28	small
	pERK1/2$^+$ & DBH$^+$	6	5	29	**0.01**	**0.02**	0.78	large
DMX (~67)	pERK1/2$^+$	6	5	18.5	0.58	0.71	0.19	small
	ChAT$^+$	6	5	14	0.93	1.00	0.05	small
	DBH$^+$	6	5	25.5	0.06	0.19	0.59	large
	pERK1/2$^+$, ChAT$^-$, & DBH$^-$	6	5	NA	NA	NA	NA	NA
	pERK1/2$^-$, ChAT$^+$, & DBH$^-$	6	5	4.5	0.07	0.19	0.58	large
	pERK1/2$^-$, ChAT$^-$, & DBH$^+$	6	5	NA	NA	NA	NA	NA
	pERK1/2$^+$, ChAT$^+$	6	5	18.5	0.58	0.71	0.19	small
	pERK1/2$^+$, DBH$^+$	6	5	NA	NA	NA	NA	NA
	ChAT$^+$, DBH$^+$	6	5	25.5	0.06	0.19	0.59	large
	pERK1/2$^+$, ChAT$^+$, & DBH$^-$	6	5	18.5	0.58	0.71	0.19	small
	pERK1/2$^-$, ChAT$^+$, & DBH$^+$	6	5	25	0.08	0.19	0.56	large
	pERK1/2$^+$, ChAT$^-$, & DBH$^+$	6	5	NA	NA	NA	NA	NA
	pERK1/2$^+$, ChAT$^+$, & DBH$^+$	6	5	16	0.92	1.00	0.06	small

* 0.1 to < 0.3 – small, 0.3 to < 0.5 – moderate, and > or = 0.5 – large

DBH+ perikaryon profile counts for these eleven subjects. **Tables 4 and 5** present the descriptive statistics and test statistics, respectively, of all comparisons at this level for these subjects. Although we observed treatment-associated differences in Abercrombie-corrected profiles displaying pERK1/2+ immunoreactivity in the DMX at *BM4.0* atlas level 67 **(Fig. 6)**, the numbers of profiles (single-, double-, or triple-labeled) did not differ between saline- and 2-DG-treated rats (see **Fig. 9** and **Table 5**). Similarly, no differences were observed in the numbers of ChAT+ and DBH+ perikaryon profiles between treatment groups.

In the absence of significant changes in the number of DMX perikaryon profiles, the relative percentages of Abercrombie-corrected single-, double-, and triple-labeled profiles were calculated for saline and 2-DG groups, and visualized as pie charts in **Figure 10**. The majority of the pERK1/2+ perikaryon profiles in the DMX at level 67 were identified to be ChAT+ in both saline- (97.7%) and 2-DG-treated (97.8%) rats (**Fig. 10**, pERK+ row, pERK1/2+ & ChAT+; *magenta-colored fraction*). Interestingly, for the total number of ChAT+ perikaryon profiles, the percentage of pERK1/2+ & ChAT+ double-labeled perikaryon profiles appears to be greater in 2-DG- (45%) than saline-treated (33.9%) rats.

3.2.3 Representative results in single pairs of subjects at atlas level 69

3.2.3.1 Phospho-ERK1/2-immunoreactive patterns mapped to Level 69. **Figure 11** shows the mapped distributions of phospho-ERK1/2 activation in NTS and DMX neurons at level 69 following saline or 2-DG administration. Saline treatment was not associated with considerable levels of phospho-ERK1/2 immunoreactive perikaryon profiles in the NTS at level 69 **(Fig. 11A-iii)**. Conversely, 2-DG treatment corresponded to pronounced levels of the activation marker in comparable tissue sections **(Fig. 11B-iii)**. Saline treatment was associated with a low amount of basally activated ChAT-immunopositive perikarya that dimly emitted phospho-ERK1/2 signal in the DMX at level 69 **(Fig. 11A-vii)**. Similar to level 67, the total numbers of phospho-ERK1/2-immunoreactive perikaryon profiles, and relative brightness of the fluorescent signal, increased to a slight extent following 2-DG administration **(Fig. 11B-vii)**. In both groups, fewer ChAT-immunoreactive profiles that were also DBH-

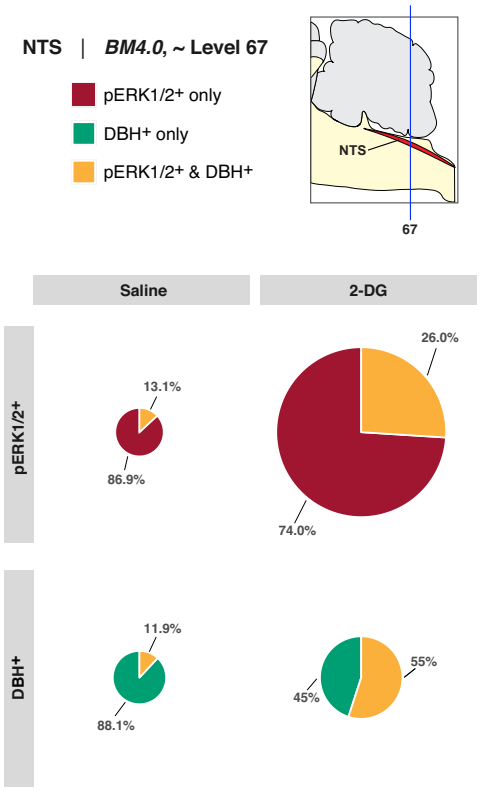

Figure 8. Relative percent differences of perikarya phenotypes in *BM4.0* atlas level 67-registered *nucleus of solitary tract (>1840)* (NTS) in saline- and 2-DG-treated subjects. Relative percentages of single- and double-labeled perikaryon profiles were calculated for pERK1/2+ (*top row*) and DBH+ (*bottom row*) cell types in each treatment group and displayed as pie charts. Charts are paneled with treatment group as column and cell type as row. The size of each pie chart was scaled according to its corresponding total Abercrombie-corrected [109] perikaryon profile number. For example, the 2-DG group pERK1/2+ pie chart (*top right panel*) has a larger diameter than the saline group pERK1/2+ pie chart (*top left panel*), corresponding to the Abercrombie-corrected perikaryon profile number presented in **Figure 7**. Note the high percentage of pERK1/2+-only perikaryon profiles in the top row in both saline- and 2-DG-treated rats.

immunopositive, or triple-labeled, were observed at this level. A few phospho-ERK1/2-immunoreactive profiles were found in the NTSco, but not in the NTSl or XII.

Figure 12 presents confocal images of tissue sections that better showcase the elevated numbers of perikaryon profiles displaying pERK1/2 immunoreactivity within the NTS and DMX of 2-DG-treated subjects as compared to those receiving saline vehicle. Increased numbers of perikaryon profiles co-labeled with DBH, and those expressing only pERK1/2, were observed in the NTS in association with 2-DG treatment **(Fig. 12B"-ii)**. Within the DMX, saline-treated subjects displayed few pERK1/2-immunoreactive profiles that mostly populated the medial portion of the nucleus **(Fig. 12A"-ii)**. 2-DG treatment was associated with minor elevations in pERK1/2 immunoreactivity within the DMX that did not appear to show a preferential distribution through the nucleus **(Fig. 12B"-ii)**.

3.2.4 Group-level effects of saline versus 2-deoxy-D-glucose administration on NTS and DMX activation at BM4.0 atlas level 69

3.2.4(a) Quantitative analysis of NTS activation at level 69. To determine NTS activation in association with saline and 2-DG treatments, pERK1/2- and DBH-immunoreactive perikaryon profiles were counted in the NTS at *BM4.0* atlas Level 69 for saline- (n=6) and 2-DG-treated (n=4) subjects. **Figure 13** shows box plots of Abercrombie-corrected phospho-ERK1/2+ and DBH+ perikaryon profile counts. **Table 6** presents the descriptive statistics of our quantitative analysis and test statistics of all the comparisons were presented in **Table 7**.

Median numbers of pERK1/2-immunoreactive profiles in saline and 2-DG groups were 3.6 and 8.3, respectively **(Table 6)**, and the distributions in the two groups differed significantly (Wilcoxon statistic = 24,

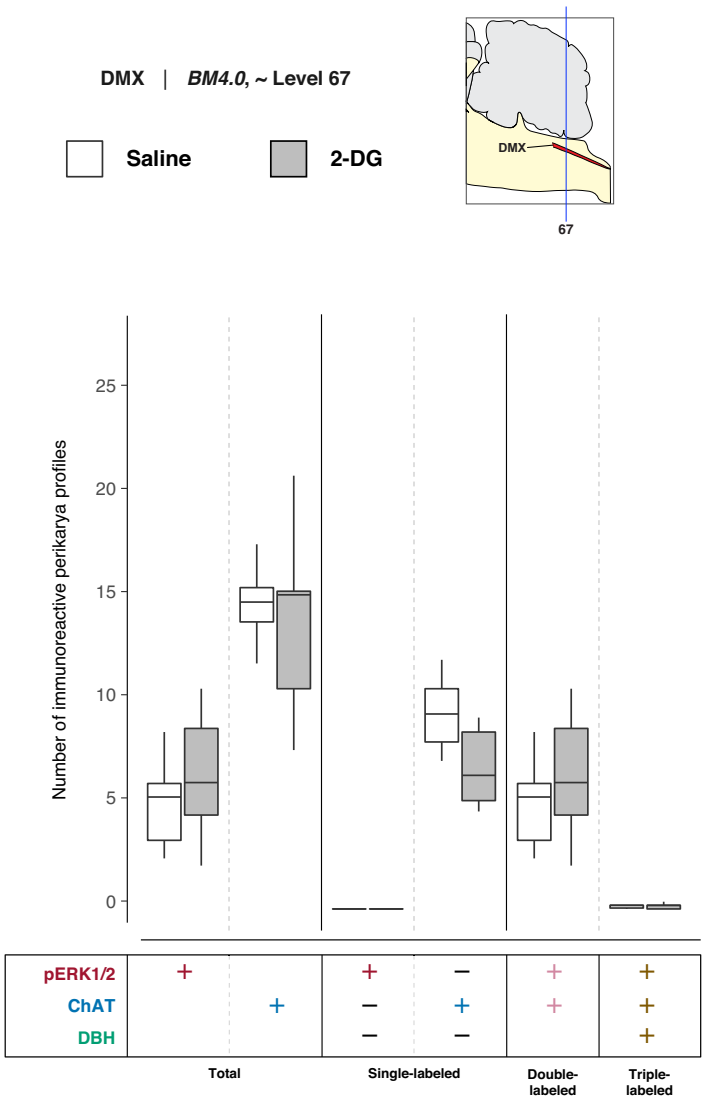

Figure 9. 2-DG administration is not associated with an alteration of activation patterns in *dorsal motor nucleus of vagus nerve (>1840)* (DMX) perikaryon profiles registered to *BM4.0* atlas level 67. Abercrombie-corrected [109] perikaryon profile counts from both saline- and 2-DG-treated subjects are represented as box plots displaying the total numbers of phospho-ERK1/2- or ChAT- or DBH-immunoreactive profiles, or only the single-, double-, and triple-labeled profiles, from tissue sections identified to be in register with *BM4.0* atlas level 67 (map, *upper right*). Differences in the numbers of perikaryon profiles were not significant; see **Tables 4 & 5** for a statistical summary.

FDR-adjusted $p < 0.05$; effect size: large; **Table 7**). The number of pERK1/2-immunoreactive profiles within the NTS significantly increased following 2-DG treatment as compared to saline-treated controls (**Fig. 13**; 'total' column (pERK1/2: +); FDR-adjusted $p < 0.05$; effect size: large; **Table 7**). The median numbers of double-labeled profiles in saline and 2-DG groups were 0.8 and 2.9, respectively **(Table 6)**, that again were significantly different (Wilcoxon statistic = 24, FDR-adjusted $p < 0.05$; effect size: large; **Table 7**). Total numbers of DBH-labeled profiles (**Fig. 13**, 'total' column (DBH: +); see also **Table 7**) did not significantly vary between treatment groups.

3.2.4(b) 2-DG-treatment associated relative changes in perikarya phenotype composition of NTS at level 69. To identify 2-DG treatment associated changes in perikarya phenotype composition in the NTS at level 69, relative percentages of Abercrombie-corrected single (pERK1/2+ only or DBH+ only) and double-labeled (pERK1/2+ & DBH+) perikaryon profiles were calculated for saline and 2-DG groups, and visualized as pie charts in **Figure 14**. Similar to the relative percentages observed in the NTS region at atlas level 67, a majority of the pERK1/2+ perikaryon profiles were identified to be DBH– in both saline (74.8%) and 2-DG (62.7%) treated rats (**Fig. 14**, pERK+ row, pERK1/2+ only; *maroon-colored fraction*). Consistent with level 67 NTS perikaryon

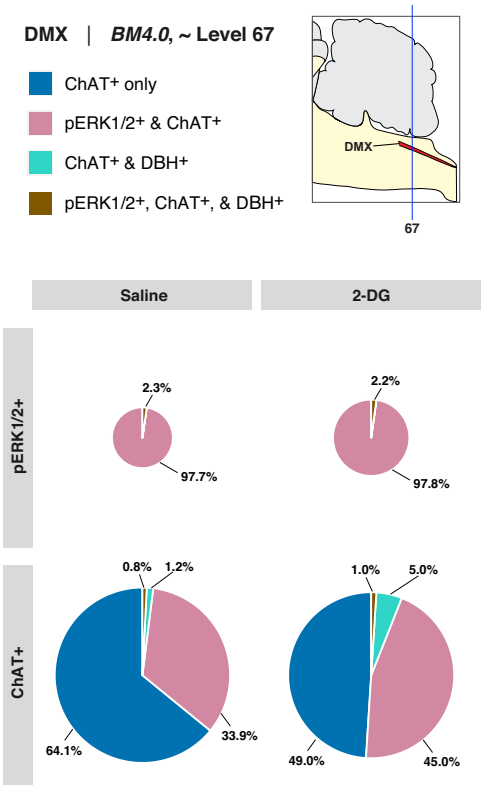

Figure 10. Relative percent differences of perikaryon phenotypes in *BM4.0* atlas level 67-registered *dorsal motor nucleus of vagus (>1840)* (DMX) in saline- and 2-DG-treated subjects. Relative percentages of single-, double-, and triple-labeled perikaryon profiles were calculated for pERK1/2+ (*top row*) and ChAT+ (*bottom row*) cell types in each treatment group and displayed as pie charts. Charts are paneled with treatment group as column and cell type as row. The size of each pie chart was scaled according to its corresponding total Abercrombie-corrected [109] perikaryon profile number.

---

profile relative percentages, in DBH+ perikaryon profiles, a higher percentage of pERK1/2+ cell profiles was observed in the NTS region of 2-DG (27.7%) than saline (9.2%) treated rats (**Fig. 14**, DBH+ row, pERK1/2+ & DBH+; *yellow-colored fraction*).

3.2.4(c) Quantitative analysis of DMX activation and relative changes in perikarya phenotype composition at level 69. To determine DMX activation in association with saline and 2-DG treatments, pERK1/2-, ChAT-, and DBH-immunoreactive perikaryon profiles were counted in the DMX at *BM4.0* atlas level 69 for saline- (n=6) and 2-DG- (n=4) treated subjects. **Figure 15** shows box plots of Abercrombie-corrected phospho-ERK1/2+, ChAT+, and DBH+ perikaryon profile counts. **Table 6** presents the descriptive statistics and test statistics of all the comparisons were presented in **Table 7**. Median numbers of phospho-ERK1/2-immunoreactive profiles in saline and 2-DG groups were 8.8 and 8.5, respectively **(Table 6)**, and the distributions in the two groups were not statistically different (Wilcoxon statistic = 11.5 , FDR-adjusted p = 1; **Table 7**). The total numbers of ChAT-labeled profiles (**Fig. 15**, 'total' column (ChAT: +); see also **Table 7**) or ChAT-labeled profiles also immunopositive for DBH (**Fig. 15**; see also **Table 7**) did not vary significantly between treatment groups. Thus, triple-labeled perikaryon profile counts (**Fig. 15**, 'triple-labeled' column; see also **Table 7**) were not significantly different between groups.

In the absence of the significant changes in the number of DMX perikaryon profiles, the relative percentages of Abercrombie-corrected single-, double-, and triple-labeled profiles were calculated for saline and 2-DG groups, and visualized as pie charts in **Figure 16**. Similar to the level 67 results, the majority of the pERK1/2+ perikaryon profiles in the DMX at level 69 were identified to be ChAT+ in both saline (99.7%) and 2-DG- (100%) treated rats (**Fig. 16**, pERK+ row, pERK1/2+ & ChAT+; *magenta-colored fraction*). However, for total ChAT+ perikaryon profiles, the percentage of pERK1/2+ & ChAT+ double-positive perikaryon profiles appears to be greater in 2-DG- (53.5%) than saline-treated (43.6%) rats, but the difference is not as prominent as for the relative percentages at level 67.

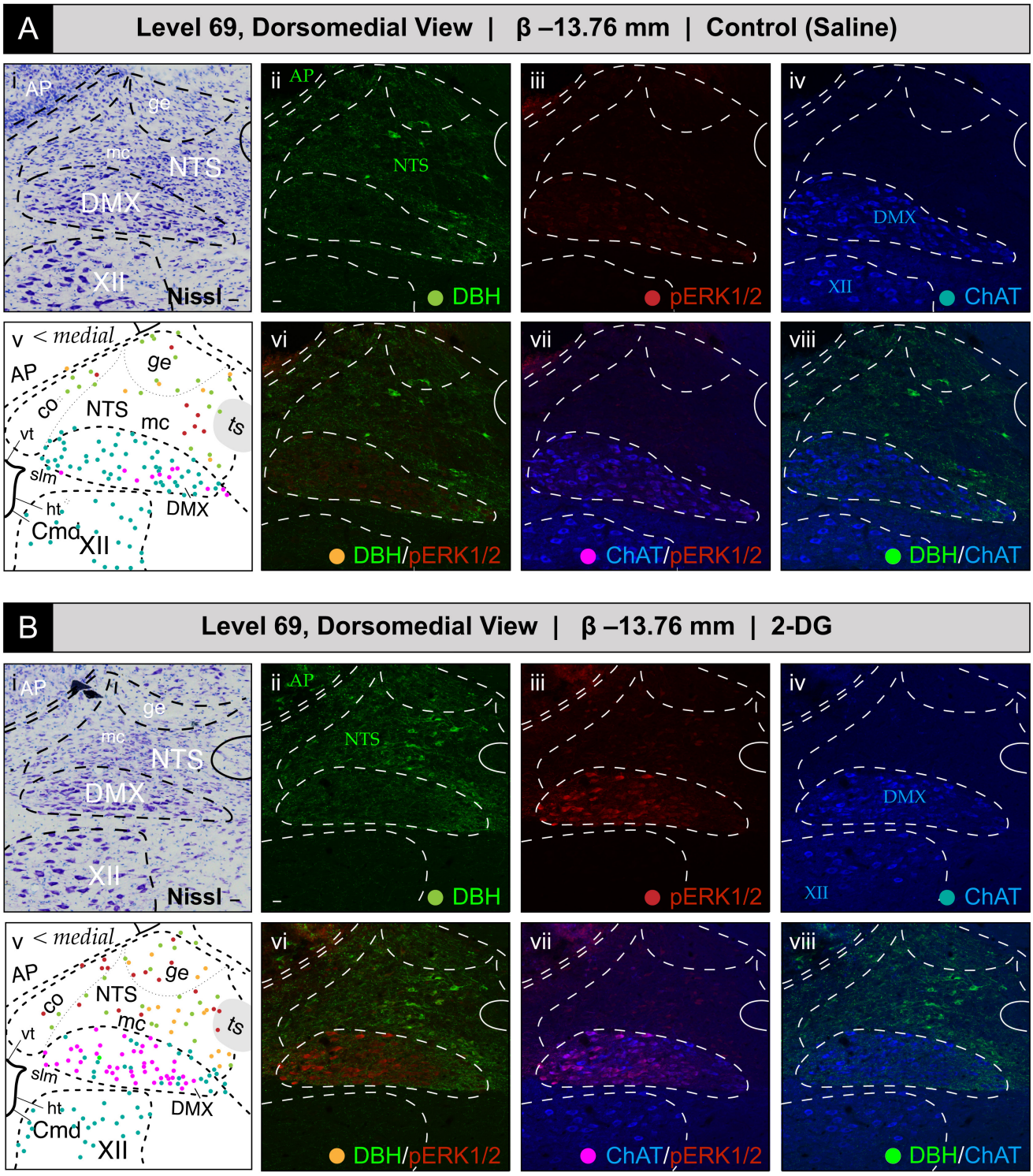

Figure 11. Glycemic challenge is associated with the recruitment of dorsal *medulla (Winslow, 1733)* [37] (MY) neurons mapped to atlas level 69 of *Brain Maps 4.0 (BM4.0)* [82]. Cytoarchitecture- and chemoarchitecture-based spatial analysis of distributed phosphorylated MAP kinase (pERK1/2) signal within dorsal RB neurons at the level of the *area postrema (>1840)* (AP) (Level 69 in the *BM4.0* rat brain atlas). **(A, B)** The panels display bright-field Nissl photomicrographs **(i)**, single- **(ii–iv)** and dual-channel **(vi–viii)** fluorescence images, and *BM4.0* atlas maps **(v)** for saline- **(A)** and 2-DG-treated **(B)** subjects of individual immunoreactivity patterns for dopamine β-hydroxylase (DBH, *green*), phospho-ERK1/2 (pERK1/2, *red*) and choline acetyltransferase (ChAT, *blue*). The patterns fall near and within the boundaries for the AP, *nucleus of solitary tract (>1840)* (NTS), *dorsal motor nucleus of vagus nerve (>1840)* (DMX), and *hypoglossal nucleus (>1840)* (XII). Note that the AP and NTS labels are colored *green* to signify their boundary determinations using the pattern of immunoreactivity observed for DBH in the green channel, and DMX and XII locations are labeled in *blue* to signify their boundary determinations using ChAT-immunoreactive signal in the far-red channel. Tissue is shown in the coronal plane. Scale bars in **(i)** and **(ii)**, which mark 20 µm, and the medial orientation noted for the maps in **(v)**, apply to all photomicrographs. Headers for **A** and **B** denote the inferred anteroposterior stereotaxic coordinate, expressed as millimeters from the Bregma (β) skull suture. See the list of abbreviations at the end of this article for a description of those marked on the maps.

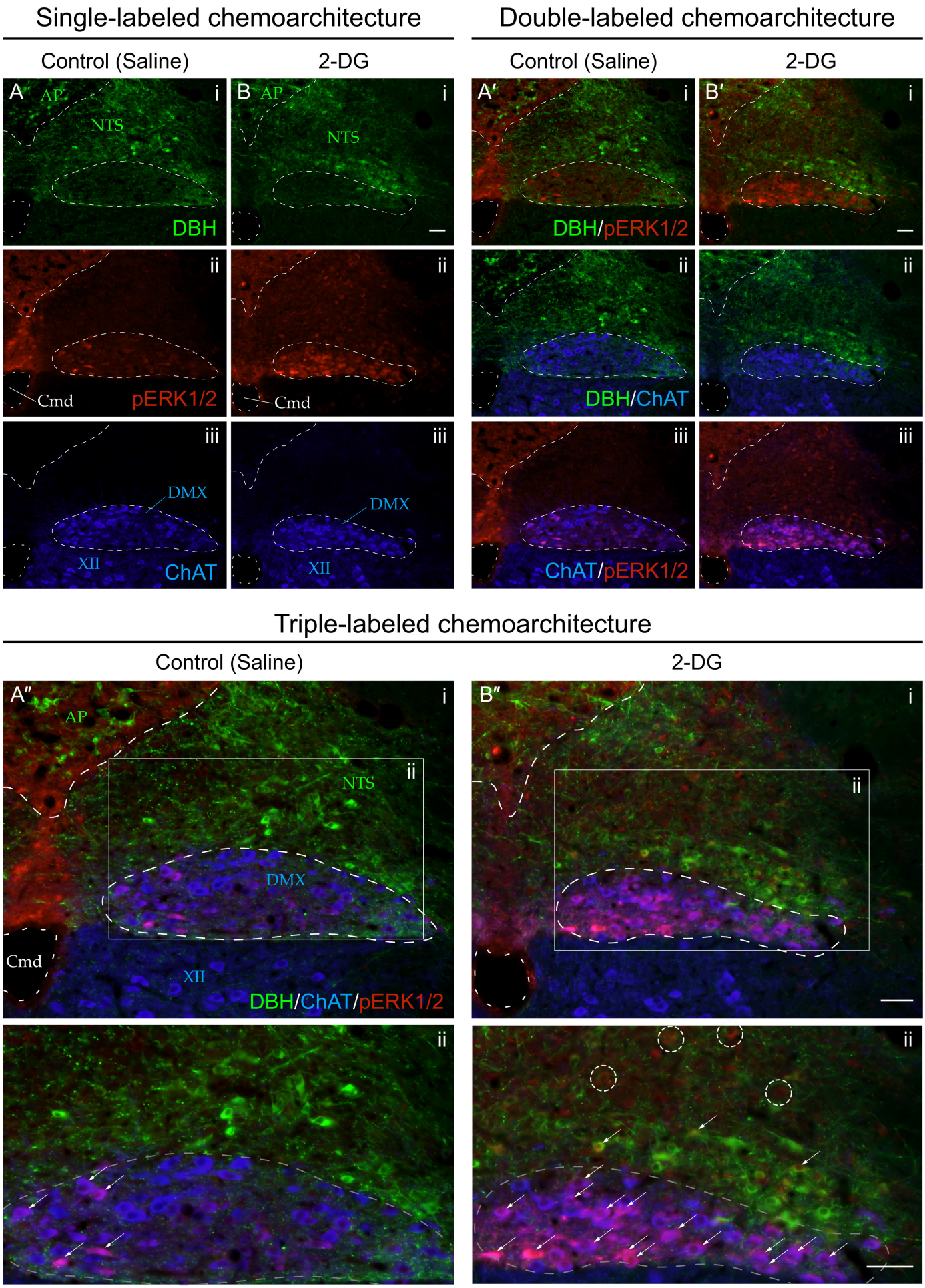
Single-labeled chemoarchitecture
Double-labeled chemoarchitecture
Control (Saline)
2-DG
Control (Saline)
2-DG
A
AP
NTS
DBH
B
AP
NTS
A′
DBH/pERK1/2
B′
Cmd
pERK1/2
Cmd
DBH/ChAT
DMX
XII
ChAT
DMX
XII
ChAT/pERK1/2
Triple-labeled chemoarchitecture
Control (Saline)
2-DG
A″
AP
NTS
DMX
Cmd
XII
DBH/ChAT/pERK1/2
B″

Figure 12 (*on previous page*). Increased recruitment of dorsal *medulla (Winslow, 1733)* [37] (MY) neurons 15 min after intravenous 2-deoxy-D-glucose (2-DG) administration relative to saline-treated subjects. Single-channel **(A, B)**, dual-channel **(A', B')**, and triple-channel **(A", B")** coronal-plane images, from saline- **(A, A', A")** and 2-DG-treated **(B, B', B")** subjects, of individual immunoreactivity patterns for dopamine β-hydroxylase (DBH; *green*), phospho-ERK1/2 (pERK1/2; *red*) and choline acetyltransferase (ChAT; *blue*) in the *area postrema (>1840)* (AP), *nucleus of solitary tract (>1840)* (NTS), *dorsal motor nucleus of vagus nerve (>1840)* (DMX), and *hypoglossal nucleus (>1840)* (XII), in the vicinity of the *central canal of medulla (>1840)* (Cmd). Note that the AP and NTS labels are colored *green* to signify their boundary determinations using the pattern of immunoreactivity observed for DBH in the green channel, and DMX and XII locations are labeled in *blue* to signify their boundary determinations using ChAT immunoreactive signal in the far-red channel. See the methods section for more details. Phospho-ERK1/2 immunoreactivity (*red*) is also present in NTS perikaryon profiles of unidentified phenotype (see *dashed circles* in **B".ii**) in 2-DG-treated but not saline-treated subjects.

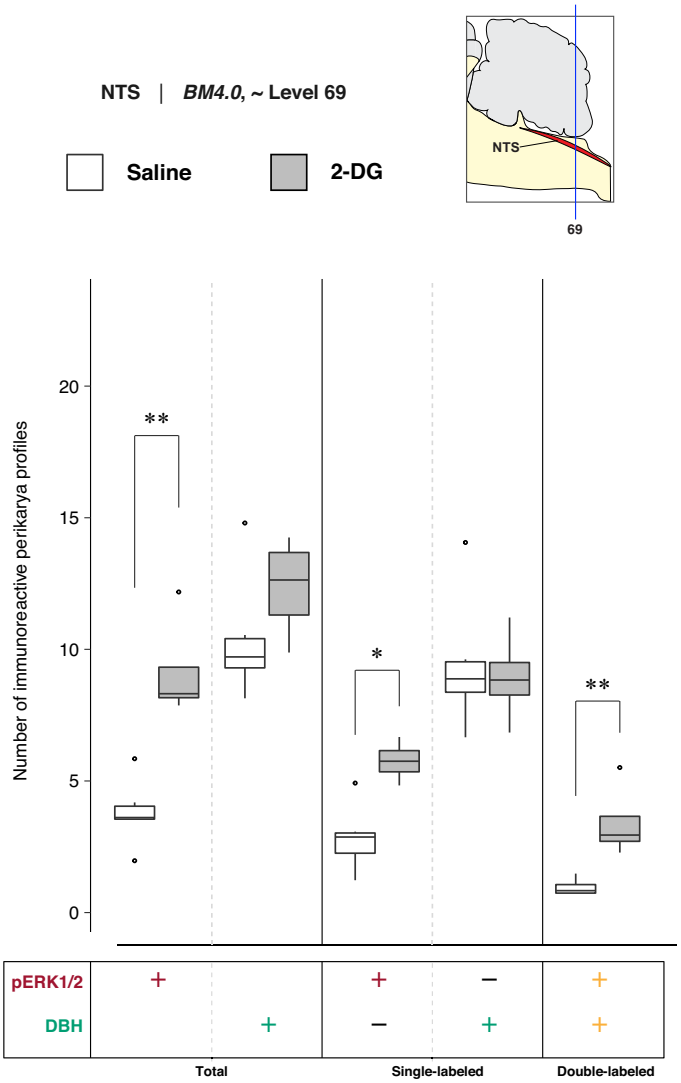

Figure 13. 2-DG administration is associated with a marked alteration of activation patterns in *nucleus of solitary tract (>1840)* (NTS) perikaryon profiles registered to *BM4.0* atlas level 69. Abercrombie-corrected [109] perikaryon profile counts from both saline- and 2-DG-treated subjects are represented as box plots displaying the total numbers of phospho-ERK1/2- or DBH-immunoreactive profiles, or only the single- and double-labeled profiles, from tissue sections identified to be in register with *BM4.0* atlas level 69 (map, *upper right*). An asterisk (*) denotes statistical significance between groups, FDR-adjusted $p < 0.05$. See **Tables 6 & 7** for details.

Table 6. Summary of descriptive statistics for NTS and DMX perikarya profiles at atlas level 69

Region	Perikarya phenotype	Saline				2-DG			
		n	Median	Q1	Q3	n	Median	Q1	Q3
NTS (~69)	pERK1/2^{+}	6	3.6	3.5	4.0	4	8.3	8.3	9.3
	DBH^{+}	6	9.7	9.3	10.4	4	12.6	11.3	13.7
	pERK1/2^{+} & DBH^{-}	6	2.9	2.2	3.0	4	5.7	5.3	6.1
	pERK1/2^{-} & DBH^{+}	6	8.9	8.4	9.5	4	8.8	8.3	9.5
	pERK1/2^{+} & DBH^{+}	6	0.8	0.7	1.1	4	2.9	2.7	3.6
DMX (~69)	pERK1/2^{+}	6	8.8	8.0	9.6	4	8.5	6.9	11.2
	ChAT^{+}	6	20.9	20.3	21.4	4	17.0	16.2	18.8
	DBH^{+}	6	0.1	0	0.1	4	0	0	0.04
	pERK1/2^{+}, ChAT^{-}, & DBH^{-}	6	0	0	0	4	0	0	0
	pERK1/2^{-}, ChAT^{+}, & DBH^{-}	6	11.9	11.5	12	4	8.0	7.5	8.8
	pERK1/2^{-}, ChAT^{-}, & DBH^{+}	6	0	0	0	4	0	0	0
	pERK1/2^{+}, ChAT^{+}	6	8.8	8.0	9.6	4	8.5	6.9	11.2
	pERK1/2^{+}, DBH^{+}	6	0	0	0	4	0	0	0
	ChAT^{+}, DBH^{+}	6	0.8	0	0.1	4	0	0	0.04
	pERK1/2^{+}, ChAT^{+}, & DBH^{-}	6	8.0	9.6	1.6	4	6.9	11.2	4.4
	pERK1/2^{-}, ChAT^{+}, & DBH^{+}	6	0.8	0	0.1	4	0	0	0.04
	pERK1/2^{+}, ChAT^{-}, & DBH^{+}	6	0	0	0	4	0	0	0
	pERK1/2^{+}, ChAT^{+}, & DBH^{+}	6	0	0	0	4	0	0	0

Table 7. Summary of non-parametric test statistics and effect sizes for NTSm/DMX perikaryon profiles at Atlas Level 69

Region	Cell phenotype	Sample size		Wilcoxon Rank-Sum test		Wilcoxon effect size	
		Saline	2-DG	Test statistic	*p*-value	Effect size	Magnitude*
NTSm (~ 69)	pERK1/2^{+}	6	4	24	**0.01**	0.82	large
	DBH^{+}	6	4	18	0.24	0.40	moderate
	pERK1/2^{+}, DBH^{-}	6	4	22.5	**0.03**	0.71	large
	pERK1/2^{-}, DBH+	6	4	11	0.91	0.07	small
	pERK1/2^{+}, DBH^{+}	6	4	24	**0.01**	0.82	large
DMX (~69)	pERK1/2^{+}	6	4	11.5	1.00	0.03	small
	ChAT^{+}	6	4	8	0.45	0.27	small
	DBH^{+}	6	4	8.5	0.46	0.27	small
	pERK1/2^{+}, ChAT^{-}, DBH^{-}	6	4	NA	NA	NA	NA
	pERK1/2^{-}, ChAT^{+}, DBH^{-}	6	4	3	0.07	0.60	large
	pERK1/2^{-}, ChAT^{-}, DBH^{+}	6	4	NA	NA	NA	NA
	pERK1/2^{+}, ChAT^{+}	6	4	11.5	1.00	0.03	small
	pERK1/2^{+}, DBH^{+}	6	4	NA	NA	NA	NA
	ChAT^{+}, DBH^{+}	6	4	8.5	0.46	0.27	small
	pERK1/2^{+}, ChAT^{+}, DBH^{-}	6	4	11.5	1.00	0.03	small
	pERK1/2^{-}, ChAT^{+}, DBH^{+}	6	4	8.5	0.46	0.27	small
	pERK1/2^{+}, ChAT^{-}, DBH^{+}	6	4	NA	NA	NA	NA
	pERK1/2^{+}, ChAT^{+}, DBH^{+}	6	4	10	0.54	0.25	small

* 0.1 to < 0.3 – small, 0.3 to < 0.5 – moderate, and > or = 0.5 – large

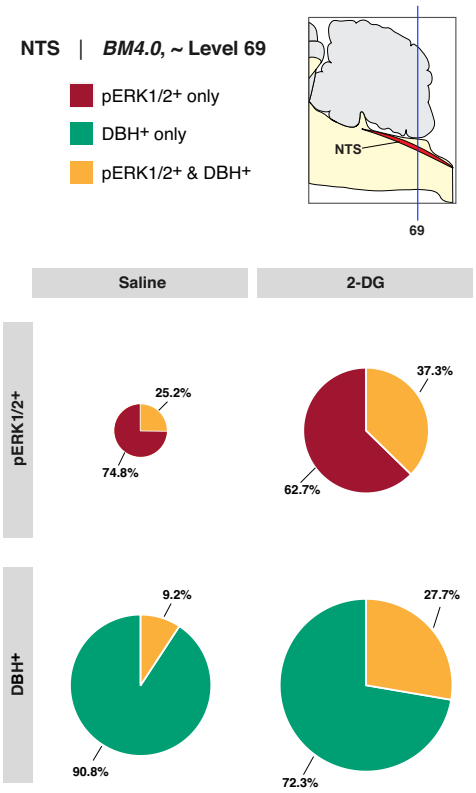

Figure 14. Relative percent changes of perikaryon profile phenotypes in *BM4.0* atlas level 69- registered n*ucleus of solitary tract (>1840)* (NTS) 15 min after 2-DG administration. Relative percentages of single and double-labeled perikarya profiles were calculated for pERK1/2+ (*top row*) and DBH+ (*bottom row*) perikaryon types in each treatment group and displayed as pie charts. Charts are paneled with treatment group as column and perikarya type as row. The size of each pie chart was scaled according to its corresponding total Abercrombie-corrected [109] perikaryon profile number. For example, the 2-DG group's pERK1/2+ pie chart (*top right panel*) has a larger diameter than the saline group pERK1/2+ pie chart (*top left panel*), corresponding to the Abercrombie-corrected perikaryon profile number presented in **Figure 13**. Notice the high percentage of pERK1/2+ only perikarya in the top row in both saline- and 2-DG-treated rats.

4. Discussion

In this study, we found that an intravenous glycemic challenge, 2-deoxy-D-glucose (2-DG), is associated with the rapid activation of *rhombic brain (His, 1893)* (RB) [21] neurons, specifically those in the *locus ceruleus (Wenzel & Wenzel, 1812)* (LC) [83] and *nucleus of solitary tract (>1840)* (NTS). These were sampled and mapped to discrete rostrocaudal levels of the *Brain Maps 4.0* open-access rat brain atlas [82]. The activation was encoded by elevations in the numbers of perikaryon profiles displaying immunoreactivity for the phosphorylated forms of ERK1/2 in these regions within 15 minutes of the challenge. These activated neurons included catecholaminergic and non-catecholaminergic neurons, some of which also displayed basal levels of activation in saline-treated subjects. Below, we discuss these findings in relation to the relevant physiology and anatomy of neural circuits engaged during feeding and glycemic counterregulation.

4.1 Physiological considerations

The activation of neural circuits during glycemic challenge, as with other systems-level processes, can be observed and measured at multiple scales, with careful considerations across these scales providing a convergence of evidence in support of the conclusions one draws for the whole system. Here, we consider multiscale questions for our measured readout (phospho-ERK1/2 immunoreactivity), our chosen stimulus (2-DG injection), and their coupling in the brain, with an eye towards an accounting of how these components, when considered together, provide evidence that the brain is mounting a physiological response to a glycemic challenge, a response that has spatiotemporal components that can be reliably tracked.

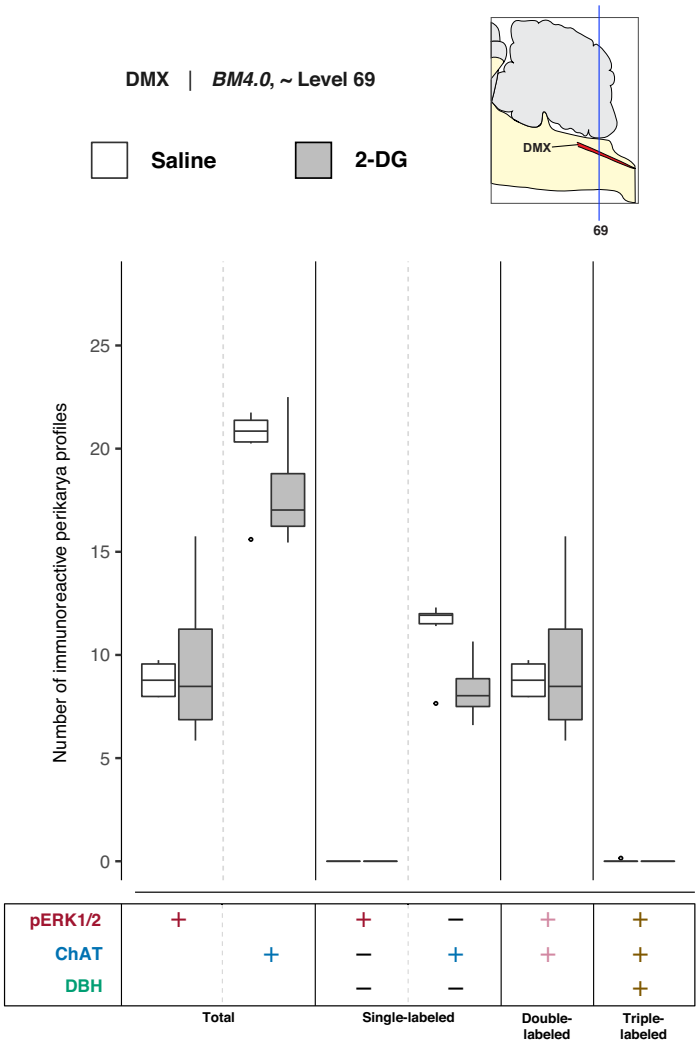

Figure 15. 2-DG administration does not alter the activation patterns in *dorsal motor nucleus of vagus nerve (>1840)* (DMX) perikaryon profiles registered to *BM4.0* atlas level 69. Abercrombie-corrected [91] perikaryon profile counts from both saline- and 2-DG-treated subjects are represented as box plots displaying the total numbers of phospho-ERK1/2- or ChAT- or DBH-immunoreactive profiles, or only the single-, double-, and triple-labeled profiles, from tissue sections identified to be in register with *BM4.0* atlas level 69 (map, *upper right*). Cell profile differences were not significant; see **Tables 6 & 7** for a statistical summary.

4.1.1 Phospho-ERK1/2 as rapid trackers of neuronal activation

As with most phenomenological concepts in science (pp 3–5 of [122]), the term 'activation' means different things under different contexts. In the brain, activation could refer to any of myriads of changes in structural or functional conditions, including, to name just a few: neuronal firing rates, intracellular Ca^{2+} metabolism, neurotransmission, gene transcription, protein translation or post-translational modifications. Whether such measures of activation always reflect relevant physiological changes underlying a given function or set of functions has been the subject of much discussion [78, 79, 123–128].

Here, we refer to 'activation' as a change in the phosphorylation status of mitogen-activated protein (MAP) kinases in *rhombic brain (His, 1893)* [21] (RB) neurons in association with 2-DG treatment. MAP kinases (EC 2.7.11.24) comprise protein kinases catalyzing a hierarchical, multi-tiered regulatory cascade of phosphorylation events [129]. Components of the ERK subfamily of MAP kinases have been localized within the RB structures we examined here, including the LC, NTS and DMX [130]. Phosphorylation of ERK1/2 kinases at residues within a Thr–X^{aa}–Tyr dual-phosphorylation motif in the enzyme activation loop (in human: Thr^{202} and Tyr^{204}; in rat: Thr^{183} and Tyr^{185}) has been demonstrated to be essential for catalytic activity [131]. The use of phospho-specific antibodies against MAP kinase is an established method of indirectly identifying a catalytically active enzyme

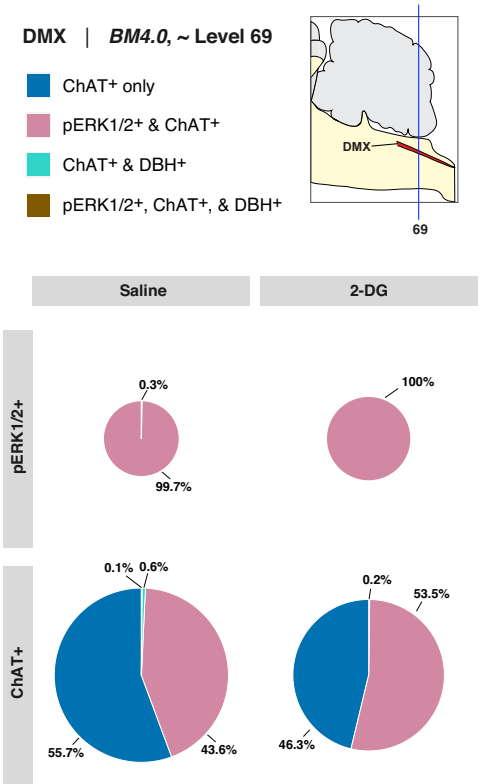

Figure 16. Relative percent changes of perikaryon phenotypes in the *BM4.0* atlas level 69-registered *dorsal motor nucleus of vagus nerve (>1840)* (DMX) 15 min after 2-DG administration. Relative percentages of single-, double-, and triple labeled perikarya profiles were calculated for pERK1/2+ (*top row*) and ChAT+ (*bottom row*) perikaryon types in each treatment group and displayed as pie charts. Charts are paneled with treatment group as column and perikaryon type as row. The size of each pie chart was scaled according to its corresponding total Abercrombie-corrected perikaryon profile numbers.

---

[132], although the phosphorylated residues bound and detected by these antibodies are, technically, products of phosphorylation reactions catalyzed by the MAP kinases hierarchically upstream of the immunolabeled enzyme [132].

Importantly, although we define activation here in terms of phosphorylation state changes, we do not measure phosphorylation per se, but the numbers of neurons displaying changes in immunoreactive signal for phosphorylated MAP kinases. The phospho-specific antibodies are selective for labeling only the phosphorylated and not the unphosphorylated forms of the enzyme. Thus, this labeling reflects activation of a pool of MAP kinase molecules, as observed from accumulated immunoreactive signals in the perikaryon, and at times the nucleus, of the imaged cell profile.

We observed greater numbers of phospho-ERK1/2+ neuronal profiles in the LC at level 51 and NTSm at levels 67 and 69 in 2-DG-treated subjects relative to saline-treated control subjects. The physiological significance of this alteration in the numbers of neurons immunoreactive for phospho-ERK1/2 is not known at this time. However, we infer from these changes that greater numbers of neurons are being 'recruited' to perform physiologically-relevant activities in the face of this glycemic challenge. In support of this view, three lines of evidence suggest that the increases reflect a change in the overall signaling status of LC and NTSm neurons to initiate *de novo* changes in gene expression and/or changes in neuronal firing rates in response to 2-DG administration. These sets of evidence will be considered in order of their decreasing relevance to the context of glycemic challenge.

First, we have previously shown that, in association with glycemic challenges such as intravenous delivery of insulin or 2-DG, phospho-ERK1/2 reliably tracks cellular activation within the *paraventricular hypothalamic nucleus (>1840)* (PVH) and *arcuate hypothalamic nucleus (>1840)* [66–69, 71]. Furthermore, under these

conditions, at least where we have established it for the *parvicellular division (>1840)* of the PVH, phospho-ERK1/2 not only tracks cellular activation during these challenges, but likely plays a causal role in downstream processes engaged by these challenges, such as recruitment of transcription factors, induction of certain gene expression patterns, and increases in neuronal firing rates [69, 72]. Thus, it seems reasonable to consider the possibility that under the same glycemic challenges the phospho-ERK1/2 observed in RB neurons may also serve similar functions. However, the links in the chain of evidence required to establish a causal role for phospho-ERK1/2 in RB neuronal responses to glycemic challenge, as it has been established for PVH responses to these challenges [70], have yet to be forged.

Second, outside of our studies of phospho-ERK1/2 in association with glycemic challenge in the RB, these enzymes have been studied under other contexts in this subdivision of the brain. For example, in the LC, ERK1/2 tracks cellular activation associated with pain-related anxiety in male arthritic rats [133] and appears to contribute to tonic inhibition of LC neurons under certain experimental conditions [134]. Optogenetic stimulation of hypocretin/orexin-expressing neurons in the hypothalamus triggers elevations in biochemically detectable phospho-ERK1 and 2 in LC tissue homogenates [135]. In the NTS, phospho-ERK1/2 mediates the suppressive effects of cholecystokinin or a melanocortin receptor agonist on food intake [136, 137]. In other RB regions, including those that correspond to the functionally-defined rostroventrolateral medulla, the ERK pathway is involved in urotensin-induced increases in sympathetic vasomotor tone [138]. Thus, throughout portions of the RB, phosphorylated ERK1/2 appear to participate within causal chains of signal transduction that link stimuli to appropriate physiological responses. This line of evidence, therefore, supports a similar role for ERK1/2 under conditions of glycemic challenge.

Finally, the more general question of whether phospho-ERK1/2 elevations correlate with other increases in 'activation', such as elevated firing rates for neurons or increased signaling cascades leading to gene expression, has been systematically addressed by Fields and colleagues in a number of incisive studies using dorsal root ganglion neurons as a model system. From these studies, they have established that ERK1/2 tracks action potential firing of neurons with a fairly high fidelity and coordinates transcriptional networks [139–142].

Taken together, these three lines of evidence offer us with independent but conceptually integrable sets of experimental results suggesting that the phosphoryl modifications of ERK1/2 kinases, under these experimental conditions, constitute an intracellular biochemical process that rapidly and reliably tracks our intervention. Moreover, they support the notion that not only are they tracking our intervention, they could be involved in mediating the physiologically meaningful responses to it. Having established this framework for our measured response, it is the nature of the intervention we used which concerns us next.

4.1.2 Intravenous 2-deoxy-D-glucose as a physiologically-relevant glycemic challenge

While phospho-ERK1/2 is well-positioned as a reliable readout of glycemic challenge, is 2-DG a physiologically-relevant stimulus for producing such a challenge? Historically, Warburg's discovery of aerobic glycolysis in tumors [143, 144] contributed to the great interest in utilizing glycolytic inhibitors, such as 2-deoxy-D-glucose (2-DG), as a means to impair tumor glucose utilization [*e.g.*, 145, 146], an interest that led to its use as a treatment for cancer patients [147]. This strategy of impairing glucose utilization also found currency in other clinical domains, most notably in using 2-DG to assess physiological counterregulatory responses in humans [148] and other animals [149–151]. At the scale of the intact living organism, 2-DG has also been used as a means to experimentally induce food intake [73, 150–156], a behavioral response that is influenced by time of day [154], diet [155], and nutritional status [156]. Notwithstanding that feeding and glucoregulatory control circuits are likely components of overlapping but nonredundant neural systems, the effects of 2-DG on both counterregulatory processes and food intake have been established well enough to provide justification of its continued utility for exploring these systems at this scale.

This assertion is further supported by studies of 2-DG that have been performed at the cellular or cell-free (isolated biochemical) scales. In particular, enzyme kinetics studies, each conducted under distinct experimental starting conditions, provide a striking convergence of circumstantial or direct evidence that 2-DG is an inhibitor of glycolysis [157–160]. The main nodal points for direct 2-DG binding — and the inhibition of glycolysis it causes

— appear to be at reaction steps catalyzed by hexokinase (EC 2.7.1.1) [157, 159, 160] and glucose-6-phosphate isomerase (GPI; EC 5.3.1.9) [158]. Although 2-DG has been empirically determined to bind with a lower affinity to brain hexokinase than glucose does ($K_m = 2.7 \times 10^{-5}$ mol/L for 2-DG vs. 8×10^{-6} mol/L for glucose [157]), Lineweaver-Burk [161] analyses applied to assay measurements of hexokinase kinetics revealed that 2-DG serves as a competitive inhibitor of the enzyme in the presence of varying concentrations of glucose, but not Mg-ATP [159]. Kidney-derived GPI, in contrast, has been shown in a cell-free system to be a principal target of 2-DG-6-PO_4 [158], which is produced by hexokinase in the presence of 2-DG. Taken together, the data indicate that there are multiple primary modes to block glycolysis by 2-DG. Moreover, allosteric feedback inhibition of hexokinase by 2-DG-6-PO_4 could serve as a secondary block of the pathway [158]. Targeted inhibition at these steps appears to be reflected in the disposition of glucose utilization *in vivo* [162], and hexokinase isoforms of the glucokinase family (EC 2.7.1.2) are expressed in the brain, and have recently been found to be critical for glucoprivic feeding triggered by 2-DG [163]. Thus, biochemical and physiological evaluations of 2-DG actions support its role in impairing glucose utilization.

Yet, despite the evidence for its direct role as a glycolysis inhibitor, evidence has also been gradually accumulating for more complex actions of 2-DG that occur alongside and perhaps as a consequence of its actions on intermediary metabolism. Early work using isolated peripheral nerve preparations demonstrated an inhibitory effect of 2-DG on electrogenic activity of the sodium-potassium pump in firing nerve [164, 165], and 2-DG appears to have observable effects on neural electrical activity more centrally, by triggering extrasynaptic GABA release which results in tonic GABA currents in central neurons at the network level, and inhibition of KATP channels in single neurons [166]. These observations have important clinical implications for individuals who are placed on a ketogenic diet to treat seizures [167]. Thus, aside from and/or perhaps as a result of 2-DG actions on glycolysis, neuronal and circuit-level electrophysiology is altered in the brain. Considered together with recently reported observations that brain endothelial cells undergo aerobic glycolysis (as described above for tumors) and that 2-DG can alter blood-brain-barrier transcellular transport mechanisms and permeability in these cells [168], it would appear that the effects of systemic 2-DG injection are diverse and complex. While here we have briefly just enumerated those effects that still fall within the contexts of glycemic challenge and inhibition of metabolism, we now consider below effects that appear somewhat distinct from these contexts.

4.1.3 Stimulus-response coupling: 2-DG coupling with phospho-ERK and alternate coupling relationships and associations

In this study, we provide evidence of an association between 2-DG administration and increases in the numbers of observable cells in our sample that display immunoreactive phospho-ERK1/2. There are compelling reasons, discussed above, supporting the physiological relevance of using 2-DG as a glycemic challenge and the reliability of the ensuing phospho-ERK1/2 responses to track this challenge. Nevertheless, invoking cause-effect relationships between external stimuli and intracellular signaling cascades is challenging (*e.g.*, see Ref. [169]), and the linkage between the two in our study awaits further strengthening and should be considered here as an initial characterization of a stimulus-response relationship. Many questions remain. 2-DG, for example, is a mannose, and as such, it can profoundly affect cells by altering their complement of glycosylated proteins [170, 171], which could alter the sensitivity or responses of cells being studied here. Thus, 2-DG could be coupled to glycosylation signaling processes independent of its glycolytic targets or downstream effects on electrical signaling or blood-brain-barrier permeability. 2-DG can also trigger a mild hypothermia and hypotension when given systemically [172, 173], responses we did not measure in our study. It is not clear if these physiological changes engage the same *rhombic brain (His, 1893)* neuronal populations that glycemic challenge does, although one laboratory has insightfully examined the populations engaged by hypotension and glucoprivation ([173]; *see Section 4.2 for more on this*).

Along similar lines, the argument that 2-DG can trigger multiple physiological conditions finds a counterpoint from our observations, thus far reported only in preliminary form [85, 87], that phospho-ERK1/2 can be triggered in the same *rhombic brain (His, 1893)* [21] (RB) regions by multiple glycemic challenges. Specifically, we have reported that intravenous injection of insulin can trigger phospho-ERK1/2 in the LC [85] much as 2-DG does in the present study. These findings provide compelling support for the idea that the coupling

of 2-DG to phospho-ERK1/2 is encoding a physiological response to changes in glycemic status. Our work also builds upon earlier work conducted by the Watts laboratory demonstrating that numbers of phospho-ERK1/2-immunoreactive neurons are elevated in the NTS and DMX in association with low concentrations of blood glucose and also exhibit a time-of-day difference in peak expression [68]. Thus, phospho-ERK1/2 does appear to track closely with glycemic challenges in portions of the RB, although it is now clear that there are other key molecules that may contribute to glucosensing or mark the presence of glucosensing neurons (*e.g.*, AMP kinase [174, 175]; GLUT2 transporter [28]; phospho-TH [176]). The activation of these molecules is likely only salient in specific places in the RB and under varying conditions, encoding glycemic and other processes in a manner germane to the subsystems the molecules serve. One could imagine that they essentially represent context-specific combinatorial codes – an emergent "biodigital jazz" [177] that allows a dynamic encoding of ever-changing events (also see Refs. [79, 142, 178]). We now discuss the physiological importance of such encoding in the RB in relation to our results.

4.1.4 Physiological significance

Keeping in mind the previous discussion concerning the reliability of our measured readout, the relevance of 2-DG as a glycemic challenge, and how well the two might be coupled, we turn now to consider the functional importance of our results. First, we consider the rapid recruitment of LC neurons observed after 2-DG challenge. Given the role the LC plays in controlling wakefulness, arousal and cognition (*e.g.*, Refs. [179, 180]), this recruitment can be integrated conceptually within the broader framework of producing or resetting arousal state during glycemic challenge, perhaps as a means to assist the organism in awareness of nutrient and/or energy deficit. If true, this may reflect a recruitment of a set of LC-connected circuits that allows the organism to mount a larger-scale resetting of behavioral state, in parallel to the circuits transmitting signals encoding glucosensing and counterregulatory responses being handled also or exclusively by other *rhombic brain (His, 1893)* [21] structures, such as the NTS and DMX. Such functional dichotomy may help explain observations that hypoglycemia unawareness can be reversed in insulin-dependent diabetics without effectively reversing impaired glucose counterregulation [181]. Perhaps the neural systems producing these distinct clinical signs of energy deficit are also distinct, or at least partly so. It is clear, however, from recent evidence for a modular organization of neural elements in the LC [182, 183] that this structure is well-suited to handling both sets of information to effect both outcomes. That the LC can receive information about glucose deficit is supported by electrophysiological evidence, in the mouse, that neurons in the rostral ventrolateral medulla, known to be activated by hypoglycemia and many other physiological conditions, can monosynaptically activate LC neurons by releasing glutamate [184].

However, the LC also figures prominently in a bevy of studies demonstrating that its neurons are highly sensitive to perturbations caused by hypoxia or hypercapnia, adjusting their excitability to conserve energy under such conditions (*e.g.*, [185–188]). The literature therefore indicates that LC neurons may be multimodally responsive to a variety of physiological perturbations, not just those that affect glycemic status. The elevated numbers of neurons immunolabeled for phospho-ERK1/2 in the LC of 2-DG-treated subjects may reflect a generalized mechanism of activation for the neurons of this structure, one that is not necessarily encoding signals exclusive to changes in glycemic status.

This may also be true for the NTSm. Like the LC, cells within this structure appear to be responsive to hypoxia and hypercapnia [186]. On the other hand, much evidence also indicates that NTS neurons actively respond to changes in glycemic status [189–191]. They possess ATP-sensitive potassium channels which appear to confer glucosensing capabilities to them [190]. These neurons depolarize in response to low extracellular glucose, but not in the presence of high glucose [191]. Thus, the phospho-ERK1/2-immunoreactivity we observed in NTS perikaryon profiles may reflect activation of glucosensing elements.

4.2 Anatomical considerations

In this study, we undertook an initial mapping of the precise locations in the *rhombic brain (His, 1893)* [21] (RB) where glycemic challenge could result in the rapid recruitment of neuronal populations, many of which play critical roles in arousal state, autonomic control and nutrient sensing [192, 193]. We identified the LC at level 51, and the NTSm and DMX at levels 67 and 69, as harboring elevated levels of phospho-ERK1/2-immunoreactive

neurons, which were identified as being either catecholaminergic or non-catecholaminergic. Below, we discuss these principal findings in relation to our methodologies and also in relation to the known anatomy of the RB.

4.2.1 Standardized mapping of activation patterns in the brain

A key goal of this study was to build upon and expand the prevailing literature by explicitly mapping patterns of neuronal activation to glycemic challenge using a standardized rat brain atlas. As we have argued previously [80, 194–196], the use of a standardized atlas to formally map cellular distributions affords investigators with the ability to examine multiple spatial datasets in a form that facilitates their direct comparison. We opted, as with all of our spatial mapping efforts for the rat (*e.g.*, Refs. [194, 196, 197]), to utilize the open-access rat brain atlas of Swanson [82], which is accompanied by a defined nomenclature that is traceable to the primary literature.

4.2.1.1 Comparison with other phospho-ERK1/2 patterns. By mapping the patterns of immunoreactivity that we observed to this reference space, we can align and interrelate our datasets with those of our own and of other laboratories that have mapped their datasets to the same atlas. For example, the Watts laboratory has shown [68] that at plasma glucose levels < 3.15 mM, increased numbers of phospho-ERK1/2-immunoreactive cells are present within the NTS and the DMX at rostrocaudal locations that fall within levels 65–66, 68–69, and 69–70 of the *Brain Maps 4.0* atlas. Importantly, at plasma glucose levels > 3.15 mM, the numbers of cells that display such immunoreactivity were much fewer by comparison. In the present study, 2-DG was utilized as the glycemic challenge, which increases plasma glucose levels while decreasing glucose utilization. Consistent with the findings of the Watts laboratory, then, the activation we observed at these atlas levels may be attributable to decreases in glucose utilization rather than hyperglycemia per se.

4.2.1.2 Comparison with certain Fos activation patterns. Moreover, other activation has been noted and mapped at or near to the atlas levels we report here. For example, peripheral injection of the GLP-1 receptor agonist, exendin-4, triggers Fos expression in the rat LC and NTSm, in neuronal populations mapped to atlas levels 52, 66, 70, and 71 [198]. On those same levels, GLP-1 immunoreactive cells and fibers were also mapped and localized to NTS subregions and surrounding areas that were largely non-overlapping with the Fos-immunoreactive neurons. Similarly, we observed increases in Fos-immunoreactive NTSm neurons (and notably, virtually no DMX neurons) at atlas level 69 in animals allowed to feed for 2 hours after an imposed 40 hr fast, as compared to subjects that were fasted for 40 hrs but not allowed to feed again [194]. This level of the NTSm is the same level in the present study where we observed neurons to be recruited by our glycemic challenge. Thus, data gathered by our laboratory from two separate studies indicate that the NTSm, at atlas level 69, contains neurons responsive to refeeding or glycemic challenge. It remains to be determined whether the same neurons can be activated in this region by both perturbations.

4.2.1.3 Reconciling chemoarchitecture with activation profiles. In the present study, we conducted atlas-based mapping on a subset of cases and found phospho-ERK1/2 immunoreactivity in catecholaminergic neurons of the LC and NTS, and cholinergic (ChAT+) and/or catecholaminergic (DBH+) neurons in the DMX. We also found perikaryon profiles that did not display immunoreactivities for either one of these phenotypes in the NTS. It is also unclear if these are neuronal profiles; indeed, the NTS has glucosensing astrocytes critical for counterregulatory responses [26, 27].

4.2.2 Alignment of activation patterns with connectivity data in the brain

The patterns of activation that we document here can also be placed in register with known neural connection patterns established by neuroanatomical tract-tracing experiments that have been mapped using the *Brain Maps 4.0* [82] framework or its earlier iterations.

4.2.2.1 Descending connections from hypothalamic regions. For example, the rat LC at level 51 reportedly receives input from a brain region, designated as MnPO by the authors [199], which corresponds essentially identically with the *median preoptic nucleus (Loo, 1931)* [200] (MEPO) in *Brain Maps 4.0* [82]. Using the *BM4.0* framework, these investigators carefully charted the axonal boutons and terminal fields of anterogradely-labeled fibers from injections of 10-kDa biotinylated dextran amine (BDA) [201] into this structure. Clearly-identifiable axons and boutons at the light-microscope level were observed in the LC (see Fig. 7a–c in Ref. [199]), which were found to closely appose tyrosine hydroxylase-immunoreactive cells of the LC (see their Fig. 7a,b). These

projections were displayed on digital templates accompanying the second edition of *Brain Maps* [202], and their existence was confirmed by injection of a retrograde tracer into the LC. The retrograde pattern of labeling, interestingly, revealed labeled cells not only in the MEPO, but also in extrahypothalamic regions, including the *bed nuclei of terminal stria, anterior division, oval nucleus (Ju & Swanson, 1989)* [203] (BSTov; see their Fig. 8f'), a region which has been previously reported in preliminary communications [79, 204, 205] as also displaying elevations of phospho-ERK1/2-immunoreactive neurons following 2-DG administration. Collectively, these nascent observations would indicate that the atlas-based mapping of MEPO→LC and BSTov→LC connections, together with our atlas-based mapping of BSTov [79, 204, 205] and LC activation (Refs. [85–89]; the present study) in association with 2-DG treatment, reveals a larger set of neural connections that may participate in relaying descending information to the LC that could be salient during glycemic challenge. This is also supported by evidence for a set of connections to the LC, albeit sparse, that have been reported from the *lateral hypothalamic area, juxtaventromedial region, dorsal zone (Swanson, 2004)* [103] LHAjvd [206]. These connections, however, invest the NTS more heavily, as shown in maps of regions of the NTS slightly more caudal to the level we mapped here (see their Fig. 4, panels AAA and BBB).

4.2.2.2 Connections with peripheral targets. Although the connections between peripheral organs and neuronal populations in the *rhombic brain (His 1893)* [21] (RB) have been intensively studied, few have traced and mapped these connections in the rat using the *Brain Maps* atlas framework in its various editions. However, Garcia-Luna *et al*. [76] have provided an elegant demonstration of the power of atlas-based mapping using this spatial model to help register peripheral nervous system connections with neuronal populations in the RB. Specifically, these colleagues have shown that vagal sensory endings innervating the wall of the hepatic portal and superior mesenteric veins make multi-order connections with neuronal populations in the *dorsal motor nucleus of vagus nerve (>1840)* (DMX). Furthermore, they showed that injections of viral tracer into the left nodose ganglion of rats produced transsynaptic labeling that, as a function of survival time, progressively reached NTS glial cells (24 h), and AP, NTS and DMX neurons (48 and 72 h).

Importantly, the patterns and distributions were charted by Garcia-Luna et al. [76] within *BM4.0* atlas space, some of the atlas levels of which are the same as those we show here that produce elevations in MAP kinase recruitment following glycemic challenge. Specifically, our maps at atlas levels 67 and 69 contain data in register with patterns in their study showing that PMV wall injections of the transsynaptic viral tracer, the H129 strain of HSV-1, infects primarily cholinergic and also a few catecholaminergic neurons in the DMX. Given the compact size of this structure and high cell-packing density of neurons there, it is reasonable to hypothesize that the phospho-ERK1/2-immunoreactive neurons we observed both in saline- and 2-DG-injected subjects in this structure include those that process afferent information from these peripheral vessels. Our findings also complement those of Garcia-Luna et al. [76]; namely, that most of these activated neurons are cholinergic. We also confirm their observation that a small percentage of neurons also double-label for ChAT- and DBH-immunoreactivities.

5. Conclusions

Our results indicate that there are rapidly activating neurons, and perhaps glial elements, that are engaged within 15 minutes of glycemic challenge in *rhombic brain (His, 1893)* [21] regions. These include neurons of the *locus ceruleus (Wenzel & Wenzel, 1812)* [83] and those in the *nucleus of solitary tract, medial nucleus (>1840)*. Some but not all these neurons are catecholaminergic. Importantly, we mapped these neurons to standardized atlas templates from *Brain Maps 4.0*, an open-access rat brain atlas that allows for data from multiple labs to be compared with one another. We discuss how our datasets match up with those showing neural connections atlas-mapped to these regions from the hypothalamus or periphery. Open questions that remain include the exact organization of the extended networks served by these activated systems, whether there are subsystems that allow for the body to adequately switch its anaerobic versus oxidative capacity [141], and whether this switch in metabolism in the face of glycemic challenge allows the organism to switch macronutrient diets accordingly [45] and to tailor its ability to counterregulate and/or ingest additional food to gain energy. These initial maps are an important step towards a global brain-wide assessment of cellular responses to glycemic challenges, which may

allow for more refined clinical or therapeutic interventions for those individuals experiencing complications as a result of iatrogenic hypoglycemia.

Author Contributions: Experimental conception and design: AMK. Project management: AMK, RHT, GPT, SB. Surgeries and in vivo experiments: LJA, AMK. Perfusions and histology: LJA, AA/SDC, GS. Tissue Inventory: AMK, GPT, AA, SDC. Immunohistochemistry: SDC, VIN. Microscopy and imaging: GPT, AMK, SDC. Cytoarchitectonic analysis and atlas-based mapping: GPT, JSP. Quantitative and exploratory data analyses: SB, GPT, JSP, AMK. Artboard construction: AMK, GPT, VIN, SB. Research funding procurement: AMK, RHT. Research supervision and training: AMK, GPT, RHT, SB, LJA, VIN. Conference presenters: GPT, JSP, SDC, AA/GS. Manuscript preparation: AMK, GPT, SB, VIN with final checks from all co-authors. All authors have read and agreed to the published version of the manuscript.

Funding: This work was supported by funds awarded to AMK from the National Institutes of Health (NIH) (DK081937, GM109817, GM127251). LJA and AA were supported by awards from the USC Undergraduate Research Assistance Program (awarded to AMK, and also jointly to AMK and RHT) and the Rose Hills Foundation (to AMK). SDC was supported by the NIH-funded UTEP SMART MIND program (R25DA033613; PI: L. E. O'Dell). GPT and JSP are 2022 Fellows of the UTEP ASPIRE Program funded by the National Science Foundation (PI: B. Flores; Co-PIs: M. O. Montes, J. I. Villalobos). This project was also supported by the NIH-funded Border Biomedical Research Center at UTEP (U54MD007592).

Institutional Review Board Statement: The animal study protocol was approved by the Institutional Animal Care and Use Committee of The University of Southern California (protocol code 11249 approved on August 26, 2009).

Data Availability Statement: All relevant protocols and data are contained within the article.

Acknowledgments: We are grateful to Dr. Alan G. Watts and Graciela Sanchez-Watts (USC) for allowing the generous use of their surgical and laboratory spaces during the early stages of this project, Dr. Larry W. Swanson (USC) and Cathleen Crayton for facilitating weekly discussions of our group in Dr. Swanson's research space and for the use of his laboratory for tissue processing, and Dr. Ted Berger (USC) for use of his laboratory. Tiffanie Nham, Michael Zobel, and Jordan Michaels participated in valuable discussions. Jeannie Y. Zhang, Danielle Goodrich, Michael Zobel, Ellen M. Walker, Evangelina Espinoza, Kenichiro Negishi and Marina Peveto provided valuable technical assistance or datasets, and Dr. Anne Jokiaho (USC) graciously facilitated access to legacy records at USC. AMK and RHT thank Dr. David Glasgow in the USC Undergraduate Education Office for his support of our students. We also thank Dr. Armando Varela-Ramirez for his assistance in the Cellular Characterization and Biorepository Core Facility of the UTEP Border Biomedical Research Center and Dr. Larry W. Swanson for clarifications concerning his atlas nomenclature. All *BM4.0* atlas maps were modified and/or reproduced with permission under the conditions outlined by a Creative Commons BY-NC 4.0 license. The authors express their appreciation for the valuable digital resources provided by the Internet Archive and The University and State Library of Saxony-Anhalt in Halle, Germany. AMK and GPT dedicate this study to the memory of the late Dr. Sue Ritter (Washington State University), for her pioneering and systematic investigations of hindbrain mechanisms of glucoregulatory control. AMK thanks his friends at DSB for their support during the final stages of this project.

Conflicts of Interest: The authors declare no conflict of interest. The funders had no role in the design of the study; in the collection, analyses, or interpretation of data; in the writing of the manuscript, or in the decision to publish the results.

Abbreviations

AP	*area postrema (>1840)*
DMX	*dorsal motor nucleus of vagus nerve (>1840)*
LC	*locus ceruleus (Wenzel & Wenzel, 1812)*
LDT	*laterodorsal tegmental nucleus (>1840)*
MEV	*midbrain nucleus of trigeminal (>1840)*
MY	*medulla (Winslow, 1733)*
NTS	*nucleus of solitary tract (>1840)*
NTSce	*nucleus of solitary tract, central subzone (>1840)*
NTSco	*nucleus of solitary tract, commissural part (>1840)*
NTSge	*nucleus of solitary tract, gelatinous subzone (>1840)*
NTSl	*nucleus of solitary tract, lateral part (>1840)*
NTSm	*nucleus of solitary tract, medial part (>1840)*
NTSmc	*nucleus of solitary tract, medial part, caudal zone general, caudal subzone (>1840)*
NTSmcg	*nucleus of solitary tract, medial part, caudal zone general (>1840)*
PB	*parabrachial nucleus (>1840)*
PCG	*pontine central gray (>1840)*
PCGg	*pontine central gray general (Swanson, 2004)*
PGRN	*paragigantocellular reticular nucleus (>1840)*
PGRNl	*paragigantocellular reticular nucleus, Lateral part (>1840)*
RB	*rhombic brain (His, 1893)*
scp	*superior cerebellar peduncle (Procháska, 1800)*
ts	*solitary tract (>1840)*
V4f	*floor of fourth ventricle (Reil, 1807–1808)*
XII	*hypoglossal nucleus (>1840)*
z	*nucleus z (>1840)*

References

1. Cryer, P.E. Banting Lecture: Hypoglycemia: the limiting factor in the management of IDDM. *Diabetes* **1994,** *43*, 1378–1389. https://doi.org/10.2337/diab.43.11.1378
2. Hirsch, I.B. Insulin analogues. *New Engl J Med* **2005,** *352*, 174–183. https://doi.org/10.1056/NEJMra040832
3. Leese, G.P.; Wang, J.; Broomhall, J.; Kelly, P.; Marsden, A.; Morrison, W. *et al*. Frequency of severe hypoglycemia requiring emergency treatment in type 1 and type 2 diabetes: a population-based study of health service resource use. *Diabetes Care* **2003,** *26*, 1176–1180. https://doi.org/10.2337/diacare.26.4.1176
4. Cryer, P.E. Mechanisms of sympathoadrenal failure and hypoglycemia in diabetes. *J Clin Invest* **2006,** *116*, 1470–1473. https://doi.org/10.1172/JCI28735
5. Cryer, P.E. Hypoglycemia: Still the limiting factor in the glycemic management of diabetes. *Endocr Prac* **2008,** *14*(6), 750–756. https://doi.org/10.4158/EP.14.6.750
6. Cryer, P.E. Hierarchy of physiological responses to hypoglycemia: Relevance to clinical hypoglycemia in Type I (Insulin Dependent) Diabetes Mellitus. *Horm Metab Res* **1997,** *29*(3), 92–96. https://doi.org/10.1055/s-2007-978997
7. Cryer, P.E. Mechanisms of hypoglycemia-associated autonomic failure and its component syndromes in diabetes. *Diabetes* **2005,** *54*, 3592–3601. https://doi.org/10.2337/diabetes.54.12.3592
8. Smith, D.; Amiel, S.A. Hypoglycaemia unawareness and the brain. *Diabetologia* **2002,** *45*, 949–958.
9. Senthilkumaran, M.; Zhou, X.-F.; Bobrovskaya, L. Challenges in modelling hypoglycaemia-associated autonomic failure: A review of human and animal studies. *Int J Endocrinol* **2016,** Article 9801640. https://doi.org/10.1155/2016/9801640
10. McCrimmon, R. Consequences of recurrent hypoglycaemia on brain function in diabetes. *Diabetologia* **2021,** *64*, 971–977. https://doi.org/10.1007/s00125-020-05369-0
11. Hevener AL, Bergman RN, Donovan CM. Portal vein afferents are critical for the sympathoadrenal response to hypoglycemia. *Diabetes* **2000,** *49*, 8–12. https://doi.org/10.2337/diabetes.49.1.8
12. Frizzell R.T.; Jones, E.M.; Davis, S.N.; Biggers, D.W.; Myers, S.R.; Connolly, S.C. *et al*. Counterregulation during hypoglycemia is directed by widespread brain regions. *Diabetes* **1993,** *42*, 1253–1261. https://doi.org/10.2337/diab.42.9.1253
13. Routh, V.H.; Donovan, C.M.; Ritter, S. Hypoglycemia detection. *Trends Endocrinol Metab* **2012,** *3*(4), 47–87. https://doi.org/10.1210/team.9781936704200.ch2
14. Tesfaye, N.; Seaquist, E.R. Neuroendocrine responses to hypoglycemia. *Ann N Y Acad Sci* **2010,** *1212*, 12–28. https://doi.org/10.1111/j.1749-6632.2010.05820.x
15. Watts, A.G.; Kanoski, S.E.; Sanchez-Watts, G.; Langhans, W. The physiological control of eating: signals, neurons, and networks. *Physiol Rev* **2022,** *102*(2), 689–813. https://doi.org/10.1152/physrev.00028.2020
16. Carus, C.G. Versuch einer Darstellung des Nervensystems und Insbesondere des Gehirns nach ihrer Bedeutung, Entwickelung und Vollendung im thierischen Organismus. Breitkopf und Härtel: Leipzig, 1814. Available online at the Internet Archive: https://archive.org/details/versucheinerdar00carugoog/page/n5/mode/2up. Last accessed on 4 Jun 2022.
17. Ritter, S.; Li, A.J.; Wang, Q.; Dinh, T.T. The value of looking backward: the essential role of the hindbrain in counterregulatory responses to glucose deficit. *Endocrinol* **2011,** *152*(11), 4019–4032. https://doi.org/10.1210/en.2010-1458
18. Donovan, C.M.; Watts, A.G. Peripheral and central glucose sensing in hypoglycemic detection. *Physiol (Bethesda)* **2014,** *29*(5), 314–324. https//doi.org/10.1152/physiol.00069.2013
19. Chan, O.; Sherwin, R.S. Is there cross talk between portal and hypothalamic glucose-sensing circuits? *Diabetes* **2014,** *63*(8), 2617–2619. https://doi.org/10.2337/db14-0755
20. Verberne, A.J.M.; Sabetghadam, A.; Korim, W.S. Neural pathways that control the glucose counterregulatory response. *Front Neurosci* **2014,** *8*, 38. https://doi.org/10.3389/fnins.2014.00038
21. His, W. Vorschläge zur Eintheilung des Gehirns. Archiv für Anatomie und Entwickelungsgeschichte 1893, [no volume indicated] pp. 172–179. Available at Google Play: https://play.google.com/books/reader?id=ff7fqzGSX7QC&pg=GBS.PA172&hl=en. Last accessed on 2 Jul 22.

22. DiRocco, R.J.; Grill, H.J. The forebrain is not essential for sympathoadrenal hyperglycemic response to glucoprivation. *Science* **1979**, *204*(4397), 1112–1114. https://doi.org/10.1126/science.451558
23. Mizuno, Y.; Oomura, Y. Glucose responding neurons in the nucleus tractus solitarius of the rat: In vitro study. *Brain Res* **1984,** *307*, 109–116. https://doi.org/10.1016/0006-8993(84)90466-9
24. Dallaporta, M.; Himmi, T.; Perrin, J.; Orsini, J.-C. Solitary tract nucleus sensitivity to moderate changes in glucose level. *NeuroReport* **1999,** *10*(12), 2657–2660. https://doi.org/10.1097/00001756-199908200-00040
25. Yettefti, K.; Orsini, J.-C.; Perrin, J. Characteristics of glycemia-sensitive neurons in the nucleus tractus solitarii: Possible involvement in nutritional regulation. *Physiol Behav* **1997,** *61*(1), 93–100. https://doi.org/10.1016/S0031-9384(96)00358-7
26. Marty, N.; Dallaporta, M.; Foretz, M.; Emery, M.; Tarussio, D.; Bady, I. et al. Regulation of glucagon secretion by glucose transporter type 2 (glut2) and astrocyte-dependent glucose sensors. *J Clin Invest* **2005,** *115*(12), 3545–3553. https://doi.org/10.1172/JCI26309
27. Klip, A.; Hawkins, M. Desperately seeking sugar: glial cells as hypoglycemia sensors. *J Clin Invest* **2005,** *115*(12), 3403–3405. https://doi.org/10.1172/JCI27208
28. Lamy, C.M.; Sanno, H.; Labouèbe, G., Picard, A.; Magnan, C.; Chatton, J.-Y. et al. Hypoglycemia-activated GLUT2 neurons of the nucleus tractus solitarius stimulate vagal activity and glucagon secretion. *Cell Metab* **2014,** *19*(3), 527–538. https://doi.org/10.1016/j.cmet.2014.02.003
29. Boychuk, C.R.; Gyarmati, P.; Xu, H.; Smith, B.N. Glucose sensing by GABAergic neurons in the mouse nucleus tractus solitarii. *J Neurophysiol* **2015,** *114*(2), 999–1007. https://doi.org/10.1152/jn.00310.2015
30. Parker, L.M.; Kumar, N.N.; Lonergan, T.; McMullan, S.; Goodchild, A.K. Distribution and neurochemical characterization of neurons in the rat ventrolateral medulla activated by glucoprivation. *Brain Struct Funct* **2015,** *220*(1), 117–134. https://doi.org/10.1007/s00429-013-0642-3.
31. Roberts, B.L.; Zhu, M.; Zhao, H.; Dillon, C.; Appleyard, S.M. High glucose increases action potential firing of catecholamine neurons in the nucleus of the solitary tract by increasing spontaneous glutamate inputs. *Am J Physiol Regul Integr Comp Physiol* **2017,** *313*, R229–R239. https://doi.org/10.1152/ajpregu.00413.2016
32. Pitra, S.; Smith, B.N. Musings on the wanderer: What's new in our understanding of vago-vagal reflexes? VI. Central vagal circuits that control glucose metabolism. *Am J Physiol Gastrointest Liver Physiol* **2021,** *320*, G175–G182. https://doi.org/10.1152/ajpgi.00368.2020
33. Garfield, A.S.; Shah, B.P.; Madara, J.C.; Burke, L.K.; Patterson, C.M.; Flak, J. et al. A parabrachial-hypothalamic cholecystokinin neurocircuit controls counterregulatory responses to hypoglycemia. *Cell Metab* **2014,** *20*(6), 1030–1037. https://doi.org/10.1016/j.cmet.2014.11.006
34. de Araujo, I.E. Expanding the brain glucosensing territory. *Cell Metab* **2014,** *20*(6), 933–935. https://doi.org/10.1016/j.cmet.2014.11.013
35. Kakall, Z.M.; Nedoboy, P.; Farnham, M.M.J.; Pilowsky, P.M. Activation of μ-opioid receptors in the rostral ventrolateral medulla blocks the sympathetic counterregulatory response to glucoprivation. *Am J Physiol Regul Integr Comp Physiol* **2018,** *315*(6), R1115–R1122. https://doi.org/10.1152/ajpregu.00248.2018
36. Sato, M.; Minabe, S.; Sakano, T.; Magata, F.; Nakamura, S.; Watanabe, Y. et al. Morphological analysis of the hindbrain glucose sensor-hypothalamic neural pathway activated by hindbrain glucoprivation. *Endocrinol* **2021,** *162*(9), 1–18. https://doi.org/10.1210/endocr/bqab125
37. Winslow, J.B. An Anatomical Exposition of the Structure of the Human Body, translated from the French Original [1732] by G. Douglas. London: Prevost, 1733. Available online at the Internet Archive: https://archive.org/details/anatomicalexposi00wins/page/n9/mode/2up. Last accessed on 2 Jul 22.
38. Ritter, S.; Taylor, J.S. Vagal sensory neurons are required for lipoprivic but not glucoprivic feeding in rats. *Am J Physiol (Regul Integr Comp Physiol)* **1990,** *258*(6), R1395–R1401. https://doi.org/10.1152/ajpregu.1990.258.6.R1395
39. Ritter, S.; Dinh, T.T. 2-Mercaptoacetate and 2-deoxy-D-glucose induce Fos-like immunoreactivity in rat brain. *Brain Res* **1994,** *641*, 111–120. https://doi.org/10.1016/0006-8993(94)91822-8.
40. Ritter, S.; Ritter, J.B.; Cromer, L. 2-deoxy-D-glucose and mercaptoacetate induce different patterns of macronutrient ingestion. *Physiol Behav* **1999,** *66*(4), 709–715. https://doi.org/10.1016/S0031-9384(99)00009-8

41. Ritter, S.; Dinh, T.T.; Zhang, Y. Localization of hindbrain glucoreceptive sites controlling food intake and blood glucose. *Brain Res 2000, 856*, 37–47. https://doi.org/10.1016/S0006-8993(99)02327-6.
42. Sanders, N.M.; Ritter, S. Repeated 2-deoxy-D-glucose-induced glucoprivation attenuates Fos expression and glucoregulatory responses during subsequent glucoprivation. *Diabetes* **2000,** *49*(11), 1865–1874. https://doi.org/10.2337/diabetes.49.11.1865
43. Ritter, S., Bugarith, K.; Dinh, T.T. Immunotoxic destruction of distinct catecholamine subgroups produces selective impairment of glucoregulatory responses and neuronal activation. *J Comp Neurol* **2001,** *432*, 197–216. https://doi.org/10.1002/cne.1097
44. Ritter, S.; Watts, A.G.; Dinh, T.T.; Sanchez-Watts, G.; Pedrow, C. Immunotoxin lesion of hypothalamically projecting norepinephrine and epinephrine neurons differentially affects circadian and stressor-stimulated corticosterone secretion. *Endocrinol* **2003,** *144*(4), 1357–1367. https://doi.org/10.1210/en.2002-221076
45. Li, A.-J.; Wang, Q.; Dinh, T.T.; Wiater, M.F.; Eskelsen, A.K.; Ritter, S. Hindbrain catecholamine neurons control rapid switching of metabolic substrate use during glucoprivation in male rats. *Endocrinol* **2013,** *154*(12), 4570–4579. https://doi.org/10.1210/en.2013-1589
46. Korim, W.S.; Farah, L.B.; McMullan, S.; Verberne, A.J.M. Orexinergic activation of medullary premotor neurons modulates the adrenal sympathoexcitation to hypothalamic glucoprivation. *Diabetes* **2014,** *63*, 1895–1906. https://doi.org/10.2337/db13-1073
47. Korim, W.S.; Llewellyn-Smith, I.J.; Verberne, A.J. Activation of medulla-projecting perifornical neurons modulates the adrenal sympathetic response to hypoglycemia: Involvement of orexin type 2 (OX2-R) receptors. *Endocrinol* **2016,** *157*(2), 810–819. https://doi.org/10.1210/en.2015-1712.
48. Sabetghadam, A.; Korim, W.S.; Verberne, A.J. Perifornical hypothalamic pathway to the adrenal gland: Role for glutamatergic transmission in the glucose counter-regulatory response. *Auton Neurosci* **2017,** *203*, 67–73. https://doi.org/10.1016/j.autneu.2017.02.002
49. Rogers, R.C.; McDougal, D.H.; Ritter, S.; Qualls-Creekmore, E.; Hermann, G.E. Response of catecholaminergic neurons in the mouse hindbrain to glucoprivic stimuli is astrocyte dependent. *Am J Physiol Regul Integr Comp Physiol* **2018,** *315*, R153–R164. https://doi.org/10.1152/ajpregu.00368.2017
50. Li, A.-i.; Wang, Q.; Ritter, S. Activation of catecholamine neurons in the ventral medulla reduces CCK-induced hypophagia and c-Fos activation in dorsal medullary catecholamine neurons. *Am J Physiol Regul Integr Comp Physiol* **2018,** *315*, R442–R452. https://doi.org/10.1152/ajpregu.00107.2018
51. Ritter, S.; Li, A.-i.; Wang, Q. Hindbrain glucoregulatory mechanisms: Critical role of catecholamine neurons in the ventrolateral medulla. *Physiol Behav* **2019,** *208*, 112568. https://doi.org/10.1016/j.physbeh.2019.112568
52. Li, A.-i.; Wang, Q.; Ritter, S. Repeated pharmacogenetic catecholamine neuron activation in the ventrolateral medulla attenuates subsequent glucoregulatory responses. *Diabetes* **2020,** *69*, 2747–2755. https://doi.org/10.2337/db20-0402
53. Senthilkumaran, M.; Bobrovskaya, L.; Verberne, A.J.M.; Llewellyn-Smith, I.J. Insulin-responsive autonomic neurons in rat medulla oblongata. *J Comp Neurol* **2018,** *526*(16), 2665–2682. https://doi.org/10.1002/cne.24523
54. Kuhlenbeck, H. Vorlesungen über das Zentralnervensystem der Wirbeltiere. Fischer: Jena, 1927.
55. Oomura, Y.; Ono, T.; Ooyama, H; Wayner, M.J. Glucose and osmosensitive neurones of the rat hypothalamus. *Nature* **1969,** *222*(5190), 282–284. https://doi.org/10.1038/222282a0
56. Oomura, Y.; Ooyama, H.; Sugimori, H.; Nakamura, T.; Yamada, Y. Glucose inhibition of the glucose-sensitive neurone in the rat lateral hypothalamus. *Nature* **1974,** *247*(5439), 284–286. https://doi.org/10.1038/247284a0
57. Oomura, Y; Yoshimatsu, H. Neural network of glucose monitoring system. *J Autonom Nerv Sys* **1984,** *10*(3–4), 359–372. https://doi.org/10.1016/0165-1838(84)90033-x
58. Routh, V.H.; Hao, L.; Santiago, A.M.; Sheng, Z.; Zhou, C. Hypothalamic glucose sensing: making ends meet. *Front Sys Neurosci* **2014,** *8*, Article 236, 1–13. https://doi.org/10.3389/fnsys.2014.00236
59. Tu, L.; Fukuda, M.; Tong, Q.; Xu, Y. The ventromedial hypothalamic nucleus: watchdog of whole-body glucose homeostasis. *Cell Biosci* **2022,** *12*(1), 71. https://doi.org/10.1186/s13578-022-00799-2
60. Zhou, C.; Teegala, S.B.; Khan, B.A.; Gonzalez, C.; Routh, V.H. Hypoglycemia: Role of hypothalamic glucose-inhibited (GI) neurons in detection and correction. *Front Physiol* **2018,** *9*, Article 192, 1–8. https://

doi.org/10.3389/fphys.2018.00192
61. Williams, R.H.; Alexopoulos, H.; Jensen, L.T.; Fugger, L.; Burdakov, D. Adaptive sugar sensors in hypothalamic feeding circuits. *Proc Natl Acad Sci USA* **2008,** *105*(33), 11975–11980. https://doi.org/10.1073/pnas.0802687105
62. Venner, A.; Karnani, M.M.; Gonzalez, J.A.; Jensen, L.T.; Fugger, L.; Burdakov, D. Orexin neurons as conditional glucosensors: Paradoxical regulation of sugar sensing by intracellular fuels. *J Physiol* **2011,** *589*(23), 5701–5708. https://doi.org/10.1113/jphysiol.2011.217000
63. Melnick, I.V.; Price, C.J.; Colmers, W.F. Glucosensing in parvocellular neurons of the rat paraventricular hypothalamus. *Eur J Neurosci* **2011,** *34*, 272–282. https://doi.org/10.1111/j.1460-9568.2011.07742.x
64. Korim, W.S.; Llewellyn-Smith, I.J.; Verberne, A.J.M. Activation of medulla-projecting perifornical neurons modulates the adrenal sympathetic response to hypoglycemia: Involvement of orexin type 2 (OX2-R) receptors. *Endocrinol* **2016,** *157*, 810–819. https://doi.org/10.121/en.2015-1712
65. Papazoglou, I.; Lee, J.-H.; Cui, Z.; Li, C.; Fulgenzi, G.; Bahn, Y.J. et al. A distinct hypothalamus-to-β cell circuit modulates insulin secretion. *Cell Metab* **2022,** *34*(2), 285–298.e7. https://doi.org/10.1016/j.cmet.2021.12.020
66. Khan, A.M.; Watts, A.G. Intravenous 2-deoxy-D-glucose injection rapidly elevates levels of the phosphorylated forms of p44/42 Mitogen-Activated Protein kinases (Extracellularly Regulated Kinases 1/2) in rat hypothalamic parvicellular paraventricular neurons. *Endocrinol* **2004,** *145*(1), 351–359. https://doi.org/10.1210/en.2003-0539
67. Khan, A.M.; Ponzio, T.A.; Sanchez-Watts, G.; Stanley, B.G.; Hatton, G.I.; Watts, A.G. Catecholaminergic control of mitogen-activated protein kinase signaling in paraventricular neuroendocrine neurons *in vivo* and *in vitro*: A proposed role during glycemic challenges. *J Neurosci* **2007,** *27*(27), 7344–7360. https://doi.org/10.1523/JNEUROSCI.0873-07.2007
68. Gorton, L.M.; Khan, A.M.; Bohland, M.; Sanchez-Watts, G.; Donovan, C.M.; Watts, A.G. A role for the forebrain in mediating time-of-day differences in glucocorticoid counterregulatory responses to hypoglycemia. *Endocrinol* **2007,** *148*(12), 6026–6039. https://doi.org/10.1210/en.2007-0194
69. Khan, A.M.; Kaminski, K.L.; Sanchez-Watts, G.; Ponzio, T.A.; Kuzmiski, J.B.; Bains, J.S.; Watts, A.G. MAP kinases couple hindbrain-derived catecholamine signals to hypothalamic adrenocortical control mechanisms during glycemia-related challenges. *J Neurosci* **2011,** *31*(50), 18479–18491. https://doi.org/10.1523/JNEUROSCI.4785-11.2011
70. Watts, A.G.; Khan, A.M. Identifying links in the chain: The dynamic coupling of catecholamines, peptide synthesis, and peptide release in hypothalamic neuroendocrine neurons. *Adv Pharmacol* **2013,** *68*, 421–444. http://dx.doi.org/10.1016/B978-0-12-411512-5.00020-8
71. Khan, A.M.; Walker, E.M.; Dominguez, N.; Watts, A.G. Neural input is critical for arcuate hypothalamic neurons to mount intracellular signaling responses to systemic insulin and deoxyglucose challenges in male rats: Implications for communication within feeding and metabolic control networks. *Endocrinol* **2014,** *155*(2), 405–416. https://doi.org/10.1210/en.2013-1480
72. Khan, A.M.; Walker, E.M.; Watts, A.G. Tracking the coupling of external signals to intracellular programs controlling peptide synthesis and release in hypothalamic neuroendocrine neurons. In *Stress: Neuroendocrinology and Neurobiology (Handbook of Stress, Volume 2)*; Fink, G., Ed.; Elsevier: Amsterdam, The Netherlands, **2017**; pp. 67–81. http://dx.doi.org/10.1016/B978-0-12-802175-0.00007-3
73. Aklan, I.; Atasoy, N.S.; Yavuz, Y.; Ates, T.; Coban, I.; Koksalar, F. *et al*. NTS catecholamine neurons mediate hypoglycemic hunger via medial hypothalamic feeding pathways. *Cell Metab* **2020,** *31*, 313–326. https://doi.org/10.1016/j.cmet.2019.11.016
74. Jokiaho, A.J.; Donovan, C.M.; Watts, A.G. The rate of fall of blood glucose determines the necessity of forebrain-projecting catecholaminergic neurons for male rat sympathoadrenal responses. *Diabetes* **2014,** *63*, 2854–2865. https://doi.org/10.2337/db13-1753
75. Bohland, M.; Matveyenko, A.V.; Saberi, M.; Khan, A.M.; Watts, A.G. Activation of hindbrain neurons is mediated by portal-mesenteric vein glucosensors during slow-onset hypoglycemia. *Diabetes* **2014,** *63*, 2866–2875. https://doi.org/10.2337/db13-1600
76. Garcia-Luna, C.; Sanchez-Watts, G.; Arnold, M.; de Lartigue, G.; DeWalt, N.; Langhans, W.; Watts, A. G. The

medullary targets of neurally conveyed sensory information from the rat hepatic portal and superior mesenteric veins. *eNeuro* **2021,** *8*(1) ENEURO.0419-20.2021, 1–20. https://doi.org/10.1523/ENEURO.0419-20.2021
77. Foster, N.N.; Azam, S.; Watts, A.G. Rapid-onset hypoglycemia suppresses Fos expression in discrete parts of the ventromedial nucleus of the hypothalamus. *Am J Physiol Regul Integr Comp Physiol* **2016,** *310*, R1177–R1185. https://doi.org/10.1152/ajpregu.00042.2016
78. Kovács, K.J. c-Fos as a transcription factor: a stressful (re)view from a functional map. *Neurochem Int* **1998,** *33*, 287–297. https://doi.org/10.1016/S0197-0186(98)00023-0
79. Watts, A.G.; Khan, A.M.; Sanchez-Watts, G.; Salter, D.; Neuner, C.M. Activation in neural networks controlling ingestive behaviors: What does it mean, and how do we map and measure it? *Physiol Behav* **2006,** *89*, 501–510. https://doi.org/10.1016/j.physbeh.2006.05.025
80. Khan, A.M. Controlling feeding behavior by chemical and gene-directed targeting in the brain: what's so spatial about our methods? *Front Neurosci* **2013,** *7*, 182. https://doi.org/10.3389/fnins.2013.00182
81. Towler, D.A.; Havlin, C.E.; Craft, S.; Cryer, P. Mechanism of awareness of hypoglycemia. Perception of neurogenic (predominantly cholinergic) rather than neuroglycopenic symptoms. *Diabetes* **1993,** *42*, 1791–1798. https://doi.org/10.2337/diab.42.12.1791
82. Swanson, L.W. *Brain maps 4.0—Structure of the rat brain*: An open access atlas with global nervous system nomenclature ontology and flatmaps. *J Comp Neurol* **2018,** *526*(6), 935–943. https://doi.org/10.1002/cne.24381
83. Wenzel, J.; Wenzel, K. De Penitiori Structura Cerebri Hominis et Brutorum; Cotta: Tübingen, Germany, **1812**. Online link; last accessed 5 May 2022.
84. Khan, A.M. Insulin-induced hypoglycemia is associated with ERK phosphorylation in locus coeruleus neurons: Implications for arousal triggered by metabolic stress, *The Neurobiology of Stress Workshop 2010*, Boulder, Colorado, USA (15–19 June 2010).
85. Jayewickreme, C.; Ramchandani, A.; Si, G.; Khan, A. M. Insulin-induced hypoglycemia is associated with ERK phosphorylation in locus coeruleus neurons: Implications for arousal triggered by metabolic stress, *2010 Neuroscience Meeting Planner*, Annual Meeting of the Society for Neuroscience, San Diego, California, USA, 13–17 November; Society for Neuroscience: Washington, DC, USA, 2010; Program No. 389.23. Online.
86. Chenausky, S.D.; Carreon, T. A., Khan, A.M. Rapid activation of hindbrain neurons following glycemic challenge: Regions and phenotypes. *COURI Symposium Abstracts, Summer 2012* [Paper 15], The University of Texas at El Paso, El Paso, Texas, USA (27 July 2012). http://digitalcommons.utep.edu/couri_abstracts_sum12/15
87. Chenausky, S.D.; Ramchandani. A.; Si, G.; Thompson, R.H.; Khan, A.M. Hindbrain autonomic nuclei: High resolution imaging of chemoarchitecture and cellular responses to glycemic challenges, In *2012 Neuroscience Meeting Planner*, Annual Meeting of the Society for Neuroscience, New Orleans, Louisiana, USA (13–17 Oct 2012); Society for Neuroscience: Washington, DC, USA, 2012; Program No. 93.14. Online.
88. Barnes, J.N.; Molina, D.D.; Tapia, G.P.; Khan, A.M. Atlas-based spatial analysis of rat hindbrain regions that display rapid activation in association with glycemic challenge. *Fall 2019 UTEP COURI Symposium*, The University of Texas at El Paso, El Paso, Texas, USA, 3 August 2019.
89. Tapia, G.P.; Agostinelli, L.J.; Chenausky, S.D.; Barnes, J.; Molina, D.D.; Khan, A.M. Atlas-based spatial analysis of rat hindbrain regions that display rapid activation in association with glycemic challenge, *2019 Neuroscience Meeting Planner*, Annual Meeting of the Society for Neuroscience, Chicago, Illinois, USA (19–23 October 2019); Society for Neuroscience: Washington, DC, USA, 2019; Program No. 591.16. Online.
90. Swanson, L.W. *Neuroanatomical Terminology: A Lexicon of Classical Origins and Historical Foundations*; Oxford University Press: New York, NY, USA, **2015**.
91. Salter, D.; Watts, A.G. Differential suppression of hyperglycemic, feeding, and neuroendocrine responses in anorexia. *Am J Physiol Regul Integr Comp Physiol* **2003,** *284*, R174–R182. https://doi.org/10.1152/ajpregu.00275.2002
92. Rinaman, L. Postnatal development of catecholamine inputs to the paraventricular nucleus of the hypothalamus in rats. *J Comp Neurol* **2001,** *438*(4), 411–422. https://doi.org/10.1002/cne.1324
93. Márquez-Ruiz, J.; Morcuende, S.; Navarro-López, J.D.D.; Escudero, M. Anatomical and pharmacological

relationship between acetylcholine and nitric oxide in the prepositus hypoglossi nucleus of the cat: functional implications for eye-movement control. *J Comp Neurol* **2007,** *503*(3), 407–420. https://doi.org/10.1002/cne.21397
94. Lenhossék, M. Der Feinere Bau Des Nervensystems im Lichte Neuester Forsuchungen. 2nd ed. H. Kornfeld: Berlin, **1895**. Available online at the Internet Archive: https://archive.org/details/derfeinerebaude00lenh/page/n3/mode/2up. Last accessed on 21 May 2022.
95. Kiernan, J. A. Classification and naming of dyes, stains and fluorochromes. *Biotech Histochem* [formerly *Stain Technol*], **2001,** *76*, 261–278. https://doi.org/10.1080/bih.76.5-6.261.278
96. Airy, G.B. On the diffraction of an object-glass with circular aperture. *Trans Camb Phil Soc* **1835,** *5* (Part 3), 283–291. Available online at the Internet Archive: https://archive.org/details/transactionsofca05camb/page/n305/mode/2up. Last accessed on 2 Jun 2022.
97. North, A.J. Seeing is believing? A beginner's guide to practical pitfalls in image acquisition. *J Cell Biol* **2006,** *172*(1), 9–18. https://doi.org/10.1083/jcb.200507103
98. Yossner, M.; Yamada, K.M. What's in a picture? The temptation of image manipulation. *J Cell Biol* **2004,** *166*(1), 11–15. https://doi.org/10.1083/jcb.200406019
99. Jost, A.P.-T.; Waters, J.C. Designing a rigorous microscopy experiment: Validating methods and avoiding bias. *J Cell Biol* **2019,** *218*(5), 1452–1466. https://doi.org/10.1083/jcb.201812109
100. Zséli, G.; Vida, B.; Martinez, A.; Lechan, R.M.; Khan, A.M.; Fekete, C. Elucidation of the anatomy of a satiety network: Focus on connectivity of the parabrachial nucleus in the adult rat. *J Comp Neurol* **2016,** *524*, 2803–2827. https://doi.org/10.1002/cne.23992
101. Simmons, D.M.; Swanson, L.W. Comparing histological data from different brains: Sources of error and strategies for minimizing them. *Brain Res Rev* **2009,** *60*, 349–367. https://doi.org/10.1016/j.brainresrev.2009.02.002
102. Reil, J.C. Fragmente über die Bildung des kleinen Gehirns im Menschen. *Archiv für die Physiologie* **1807–1808,** *8*, 1–58.
103. Swanson, L.W. *Brain Maps: Structure of the Rat Brain. A Laboratory Guide with Printed and Electronic Templates for Data, Models and Schematics, 3rd Edn.*; Elsevier: Amsterdam, **2004**; 215 pp. with CD-ROM, *Brain Maps: Computer Graphics Files 3.0.*
104. Procháska, G. Operum Minorum Anatomici, Physiologici et Pathologici Argumenti [2 parts]. Wappler et Beck: Vienna, **1800**. Available online at the : https://nbn-resolving.org/urn:nbn:de:gbv:3:1-653484. [urn:nbn:de:gbv:3:1-653484]. Last accessed on 21 May 2022.
105. Swanson, L.W. The locus coeruleus: A cytoarchitectonic, Golgi and immunohistochemical study in the albino rat. *Brain Res* **1976,** *110,* 39–56. https://doi.org/10.1016/0006-8993(76)90207-9
106. Bellingeri, C.F. De Medulla Spinali Nervisque ex ea Prodeuntibus Annotationes Anatomico-Physiologiae; Typographia Regia: Turin, 1823. Available online at the Internet Archive: https://archive.org/details/b21709142/page/n5/mode/2up. [urn:oclc:record:1040259879]. Last accessed on 21 May 2022.
107. Saper, C. Any way you cut it: A new journal policy for the use of unbiased counting methods. *J Comp Neurol* **1996,** *364*, 5. https://doi.org/10.1002/(SICI)1096-9861(19960101)364:1<5::AID-CNE1>3.0.CO;2-9
108. Coggeshall, R.E.; Lekan, H.A. Methods for determining numbers of cells and synapses: A case for more uniform standards of review. *J Comp Neurol* **1996,** *364*, 6–15. https://doi.org/10.1002/(SICI)1096-9861(19960101)364:1<6::AID-CNE2>3.0.CO;2-9
109. Abercrombie, M. Estimation of nuclear population from microtome sections. *Anat Rec* **1946,** *94*, 239–247. https://doi.org/10.1002/ar.1090940210
110. Shapiro, S.S.; Wilk, M.B. An analysis of variance test for normality (complete samples). *Biometrika* **1965,** *52*(3–4), 591–611. https://doi.org/10.1093/biomet/52.3-4.591
111. Wilcoxon, F. Individual comparisons by ranking methods. *Biometr Bull* **1945,** *1*(6), 80–83.
112. Kruskal, W.H. Historical notes on the Wilcoxon unpaired two-sample test. *J Am Stat Assoc* **1957,** *52*(279), 356–360. https://doi.org/10.1080/01621459.1957.10501395
113. Benjamini, Y.; Hochberg, Y. Controlling the False Discovery Rate: a practical and powerful approach to multiple testing. *J R Stat Assoc B* **1995,** *57*(1), 289–300. Available online at the JSTOR digital library: https://

www.jstor.org/stable/2346101.
114. R Core Team. *R: A language and environment for statistical computing.* R Foundation for Statistical Computing: Vienna, Austria, **2019**. https://www.R-project.org/
115. Kassambara, A. *rstatix*: Pipe-friendly framework for basic statistical tests. R package, version 0.7.0. https://CRAN.R-project.org/package=rstatix
116. Wickham, H. *ggplot2*: Elegant graphics for data analysis. Springer-Verlag: New York, NY, USA, **2016**.
117. Grzanna, R.; Morrison, J.H.; Coyle, J.T.; Molliver, M.E. The immunohistochemical demonstration of noradrenergic neurons in the rat brain: the use of homologous anti-serum to dopamine-β-hydroxylase. *Neurosci Lett* **1977,** *4*, 127–134. https://doi.org/10.1016/0304-3940(77)90127-6
118. Grzanna, R.; Molliver, M.E.; Coyle, J.T. Visualization of central noradrenergic neurons in thick sections by the unlabeled antibody method: A transmitter-specific Golgi image. *Proc Natl Acad Sci USA* **1978,** *75*(5), 2502–2506. https://doi.org/10.1073/pnas.75.5.2502
119. Cimarusti, D.L.; Saito, K.; Vaughn, J.E.; Barber, R.; Roberts, E.; Thomas, P.E. Immunocytochemical localization of dopamine-β-hydroxylase in rat locus coeruleus and hypothalamus. *Brain Res* **1979,** *162*, 55–67. https://doi.org/10.1016/0006-8993(79)90755-8
120. Grzanna, R.; Molliver, M.E. The locus coeruleus in the rat: An immunohistochemical delineation. *Neurosci* **1980,** *5*, 21–40. https://doi.org/10.1016/0306-4522(80)90068-8
121. Hökfelt, T.; Johansson, O.; Goldstein, M. Central catecholamine neurons with special reference to adrenaline neurons. In *Handbook of Chemical Neuroanatomy, Volume 2. Part 1: Classical Transmitters in the CNS*; Björklund, A., Hökfelt, T., Eds.; Elsevier: Amsterdam, The Netherlands, **1984**; pp. 157–276.
122. Feynman, R.P. *The Pleasure of Finding Things Out: The Best Short Works of Richard P. Feynman* (Robbins, J., Ed.). Basic Books: New York, USA, **1999**.
123. Hoffman, G.E.; Smith, M.S.; Verbalis, J.G. c-Fos and related immediate early gene products as markers of activity in neuroendocrine systems. *Front Neuroendocrinol* **1993,** *14*(3), 173–213. https://doi.org/10.1006/frne.1993.1006
124. Luckman, S.M.; Dyball, R.E.; Leng, G. Induction of c-fos expression in hypothalamic magnocellular neurons requires synaptic activation and not simply increased spike activity. *J Neurosci* **1994,** *14*(8), 4825–4830. https://doi.org/10.1523/JNEUROSCI.14-08-04825.1994
125. Bullock, T.H. Signals and signs in the nervous system: The dynamic anatomy of electrical activity is probably information-rich. *Proc Natl Acad Sci USA* **1997,** *94*, 1–6. https://doi.org/10.1073/pnas.94.1.1
126. Hoffman, G.E.; Lyo, D. Anatomical markers of activity in neuroendocrine systems: are we all 'Fos-ed out'? *J Neuroendocrinol* **2002,** *14*(4), 259–268. https://doi.org/10.1046/j.1365-2826.2002.00775.x
127. Guzowski, J.F.; Timlin, J.A.; Roysam, B.; McNaughton, B.L.; Worley, P.F.; Barnes, C.A. Mapping behaviorally relevant neural circuits with immediate early gene expression. *Curr Op Neurobiol* **2005,** *15*, 599–606. https://doi.org/10.1016/j.conb.2005.08.018
128. Hudson, A.E. Genetic reporters of neuronal activity: c-Fos and G-CaMP6. *Meth Enzymol* **2018,** *603*, 197–220. https://doi.org/10.1016/bs.mie.2018.01.023
129. Chen, Z.; Gibson, T.B.; Robinson, F.; Silvestro, L.; Pearson, G.; Xu, B.; Wright, A.; Vanderbilt, C.; Cobb, M.H. MAP kinases. *Chem Rev* **2001,** *101*, 2449–2476. https://doi.org/10.1021/cr000241p
130. Flood, D.G.; Finn, J.P.; Walton, K.M.; Dionne, C.A.; Contreras, P.C.; Miller, M.S. et al. Immunolocalization of the mitogen-activated protein kinases p42MAPK and JNK1, and their regulatory kinases MEK1 and MEK4, in adult rat central nervous system. *J Comp Neurol* **1998,** *398*, 373–392. https://doi.org/10.1002/(SICI)1096-9861(19980831)398:3<373::AID-CNE6>3.0.CO;2-X
131. Anderson, N.G.; Maller, J.L.; Tonks, N.K.; Sturgill, T.W. Requirement for integration of signals from two distinct phosphorylation pathways for activation of MAP kinase. *Nature* **1990,** *343*, 651–653. https://doi.org/10.1038/343651a0
132. Willmann, R.; Haischer, D.J.; Gust, A.A. Analysis of MAPK activities using MAPK-specific antibodies. *Meth Mol Biol* **2014,** *1171*, 27–37. https://doi.org/10.1007/978-1-4939-0922-3_3
133. Borges, G.; Miguelez, C.; Neto, F.; Mico, J. A.; Ugedo, L.; Berrocoso, E. Activation of extracellular signal-regulated kinase (ERK1/2) in the locus coeruleus contributes to pain-related anxiety in arthritic male

rats. *Intl J Neuropsychopharmacol* **2017,** *20*(6), 463. https://doi.org/10.1093/ijnp/pyx005
134. Wu, R.-N.; Kuo, C.-C.; Min, M.-Y.; Chen, R.-F.; Yang, H.-W. Extracellular signal-regulated kinases mediate an autoregulation of GABAB-receptor-activated whole-cell current in locus coeruleus neurons. *Sci Rep* **2020,** *10*, 7869. https://doi.org/10.1038/s41598-020-64292-x
135. Heydendael, W.; Sengupta, A.; Beck, S.; Bhatnagar, S. Optogenetic examination identifies a context-specific role for orexins/hypocretins in anxiety-related behavior. *Physiol Behav* **2014,** *130*, 182–190. https://dx.doi.org/10.1016/j.physbeh.2013.10.005
136. Sutton, G.M.; Patterson, L.M.; Berthoud, H.-R. Extracellular Signal-Regulated Kinase 1/2 signaling pathway in solitary nucleus mediates cholecystokinin-induced suppression of food intake in rats. *J Neurosci* **2004,** *24*(45), 10240–10247. https://doi.org/10.1523/JNEUROSCI.2764-04.2004
137. Campos, C.A.; Ritter, R.C. NMDA-type glutamate receptors participate in reduction of food intake following hindbrain melanocortin receptor activation. *Am J Physiol Regul Integr Comp Physiol* **2015,** *308*, R1–R9. https://doi.org/10.1152/ajpregu.00388.2014
138. Cao, Y.-K.; Guo, Q.; Ma, H.-J.; Wang, R.; Teng, X.; Wu, Y. Microinjection of urotensin II into the rostral ventrolateral medulla increases sympathetic vasomotor tone via the GPR14/ERK pathway in rats. *Hypertension Res* **2020,** *43*(8), 765–771. https://doi.org/10.1038/s41440-020-0460-y
139. Fields, R.D.; Eshete, F.; Stevens, B.; Itoh, K. (1997). Action potential-dependent regulation of gene expression: Temporal specificity in Ca^{2+}, cAMP-Responsive Element Binding Proteins, and Mitogen-Activated Protein Kinase signaling. *J Neurosci* **1997,** *17*(19), 7252–7266. https://doi.org/10.1523/jneurosci.17-19-07252.1997
140. Iacobas, D.A.; Iacobas, S.; Lee, P.R.; Cohen, J.E.; Fields, R.D. Coordinated activity of transcriptional networks responding to the pattern of action potential firing in neurons. *Genes* **2019,** *10*, 754. https://doi.org/10.3390/genes10100754
141. Lee, P.R.; Cohen, J.E.; Iacobas, D.A.; Iacobas, S.; Fields, R.D. Gene networks activated by specific patterns of action potentials in dorsal root ganglion neurons. *Sci Rep* **2017,** *7*, 43765. https://doi.org/10.1038/srep43765
142. Lee, P.R.; Fields, R.D. Activity-dependent gene expression in neurons. *The Neuroscientist* **2021,** *27*(4), 355–366. https://doi.org/10.1177/1073858420943515
143. Warburg, O.; Posener, K.; Negelein, E. Über den Stoffwechsel der Carcinomzelle. Biochem Zeitschr **1924**, 152, 309–344. Available online at The Internet Archive: https://archive.org/details/sim_biochemische-zeitschrift-beitraege-zur-chemischen_1924_152_0/page/308/mode/2up. Last accessed on 12 Jul 22.
144. Koppenol, W.H.; Bounds, P.L.; Dang, C.V. Otto Warburg's contributions to current concepts of cancer metabolism. *Nat Rev Cancer* **2011,** *11*, 325–337. https://doi.org/10.1038/nrc3038
145. Woodward, G.E.; Hudson, M.T. The effect of 2-desoxy-D-glucose on glycolysis and respiration of tumor and normal tissues. *Cancer Res* **1954,** *14*(8), 599–605.
146. Burk, D. Über die Begründung einer Chemotherapie des Krebses auf der grundlage einer primären hemmung der glucosephosphorylierung (Hexokinasereaktion) durch beeinflussung von substrat, coenzym und enzym. *Klin Wochenschr* **1957,** *35*, 1102–1105.
147. Landau, B.R.; Laszlo, J., Stengle, J.; Burk, D. Certain metabolic and pharmacologic effects in cancer patients given infusions of 2-deoxy-D-glucose. *J Nat Cancer Inst* **1958,** *21*(3), 485–494. https://doi.org/10.1093/jnci/21.3.485
148. Laszlo, J.; Harlan, W.R.; Klein, R.F.; Kirshner, N.; Estes, E.H., Jr.; Bogdonoff, M.D. The effect of 2-deoxy-D-glucose infusions on lipid and carbohydrate metabolism in man. *J Clin Invest* **1961,** *40*(1), 171–176. https://doi.org/10.1172/JCI104232
149. Landau, B.R.; Lubs, H.A. Animal responses to 2-deoxy-D-glucose administration. *Proc Soc Exp Biol Med* **1958,** *99*(1), 124–127. https://doi.org/10.3181/00379727-99-24268
150. Smith, G.P.; Epstein, A.N. Increased feeding in response to decreased glucose utilization in the rat and monkey. *Am J Physiol* **1969,** *217*(4), 1083–1087. https://doi.org/10.1152/ajplegacy.1969.217.4.1083
151. Pénicaud, L., Thompson, D.A., Le Magnen, J. Effects of 2-deoxy-D-glucose on food and water intake and body temperature in rats. *Physiol Behav* **1986,** *36*, 431–435. https://doi.org/10.1016/0031-9384(86)90310-0.

152. Tsujii, S.; Bray, G.A. Effects of glucose, 2-deoxyglucose, phlorizin, and insulin on food intake of lean and fatty rats. *Am J Physiol* **1990,** *258*, E476–E481. https://doi.org/10.1152/ajpendo.1990.258.3.E476
153. Edmonds, B.K.; Edwards, G.L. Dorsomedial hindbrain participation in glucoprivic feeding response to 2DG but not 2DG-induced hyperglycemia or activation of the HPA axis. *Brain Res* **1998,** *801*, 21–28. https://doi.org/10.1016/S0006-8993(98)00528-9
154. Thompson, C.I.; Fleming, R.; Franken, K.A.; Hornback, D.A.; Boha, S.P. Dual 24-hour feeding response to 2DG in rats: Daytime increase and nighttime decrease. *Physiol Behav* **1989,** *45*, 155–161. https://doi.org/10.1016/0031-9384(89)90179-0
155. Delprete, E.; Scharrer, E. Effects of 2-deoxy-D-glucose on food intake of rats are affected by diet composition. *Physiol Behav* **1992,** *51*, 951–956. https://doi.org/10.1016/0031-9384(92)90076-E
156. Singer, L.K.; Ritter, S. Differential effects of infused nutrients on 2-deoxy-D-glucose- and 2-mercaptoacetate-induced feeding. *Physiol Behav* **1994,** *56*, 1, 193–196. https://doi.org/10.1016/0031-9384(94)90279-8
157. Sols, A.; Crane, R.K. Substrate specificity of brain hexokinase. *J Biol Chem* **1954,** *210*(2), 581–595. https://doi.org/10.1016/S0021-9258(18)65384-0
158. Wick, A.N.; Drury, D.R.; Nakada, H.I.; Wolfe, J.B. Localization of the primary metabolic block produced by 2-deoxyglucose. *J Biol Chem* **1957,** *224*(2), 963–969.
159. Bachelard, H.S.; Clark, A.G.; Thompson, M.F. Cerebral-cortex hexokinases. Elucidation of reaction mechanisms by substrate and dead-end inhibitor kinetic analysis. *Biochem J* **1971,** *123*, 707–715.
160. Bachelard, H.S. Deoxyglucose and brain glycolysis. *Biochem J* **1972,** *127*(5), 83P.
161. Lineweaver, H.; Burk, D. The determination of enzyme dissociation constants. *J Am Chem Soc* **1934,** *56*(3), 658–666. https://doi.org/10.1021/ja01318a036
162. Horton, R.W.; Meldrum, B.S.; Bachelard, H.S. Enzymic and cerebral metabolic effects of 2-deoxy-D-glucose. *J Neurochem* **1973,** *21*(3), 507–520. https://doi.org/10.1111/j.1471-4159.1973.tb05996.x
163. Kessler, S.; Labouèbe, G.; Croizier, S.; Gaspari, S.; Tarussio, D.; Thorens, B. Glucokinase neurons of the paraventricular nucleus of the thalamus sense glucose and decrease food consumption. *iScience* **2021,** *24*(10), 103122. https://doi.org/10.1016/j.isci.2021.103122.
164. Hertog, A. den; Greengard, P.; Ritchie, J.M. On the metabolic basis of nerve activity. *J Physiol (London)* **1969,** *204*, 511–521. https://doi.org/10.1113/jphysiol.1969.sp008928
165. Hertog, A. den; Ritchie, J. M. A comparison of the effect of temperature, metabolic inhibitors and of ouabain on the electrogenic component of the sodium pump in mammalian non-myelinated nerve fibers. J *Physiol (London)* **1969,** *204*, 523–538. https://doi.org/10.1113/jphysiol.1969.sp008929
166. Forte, N.; Medrihan, L.; Cappetti, B.; Baldelli, P.; Benfenati, F. 2-deoxy-D-glucose enhances tonic inhibition through the neurosteroid-mediated activation of extrasynaptic GABAA receptors. *Epilepsia* **2016,** *57*(12), 1987–2000. https://doi.org/10.1111/epi.13578
167. Hartman, A.L. Glycolysis inhibition: The gift of GAB(A). *Epilepsy Currents* **2017,** *17*(2), 118–120. https://doi.org/10.5698/1535-7511.17.2.118
168. Kim, E.S.; Kim, K.-S.; Lee, C.H.; Jeon, M.-T.; Lee, S.B., Lee, J.H. *et al*. Brain endothelial cells utilize glycolysis for the maintenance of the transcellular permeability. *Mol Neurobiol* **2022,** *59*, 4315–4333. https://doi.org/10.1007/s12035-022-02778-7
169. Dumont, J.E.; Dremier, S.; Pirson, I.; Maenhaut, C. Cross signaling, cell specificity and physiology. A*m J Physiol Cell Physiol* **2002,** *282*, C2–C28. https://doi.org/10.1152/ajpcell.00581.2001
170. Datema, R.; Schwarz, R.T. Interference with glycosylation of glycoproteins. Inhibition of formation of lipid-linked oligosaccharides *in vivo*. *Biochem J* **1979,** *184*(1), 113–123. https://doi.org/doi.org/10.1042/bj1840113
171. Kutoglu, M.; Maher, J.C.; Lampidis, T.J. Differential toxic mechanisms of 2-deoxy-D-glucose versus 2-fluorodeoxy-D-glucose in hypoxic and normoxic tumor cells. *Antiox Redox Signal* **2007,** *9*(9), 1383–1390. https://doi.org/10.1089/ars.2007.1714
172. Osaka, T. 2-deoxy-D-glucose-induced hypothermia in anesthetized rats: Lack of forebrain contribution and critical involvement of the rostral raphe/parapyramidal regions of the medulla oblongata. *Brain Res Bull* **2015,** *116*, 73–80. https://doi.org/10.1016/j.brainresbull.2015.06.008

173. Parker, L.M.; Le, S.; Wearne, T.; Hardwick, K.; Kumar, N.N.; Robinson, K.J. *et al*. Neurochemistry of neurons in the ventrolateral medulla activated by hypotension: Are the same neurons activated by glucoprivation? *J Comp Neurol* **2017,** *525*(9), 2249–2264. https://doi.org/10.1002/cne.24203
174. Gujar, A.D.; Ibrahim, B.A.; Tamraker, P.; Cherian, A.K.; Briski, K.P. Hindbrain lactostasis regulates hypothalamic AMPK activity and metabolic neurotransmitter mRNA and protein responses to hypoglycemia. *Am J Physiol Regul Integr Comp Physiol* **2014,** *306*(7), R457–R469. https://doi.org/10.1152/ajpregu.00151.2013
175. Grill, H.J. Hindbrain energy status controls hypothalamic metabolic and neuropeptide signals. Focus on "hindbrain lactostasis regulates hypothalamic AMPK activity and hypothalamic metabolic neurotransmitter mRNA and protein responses to hypoglycemia". *Am J Physiol Regul Integr Comp Physiol* **2014,** *306*(7), R439–R440. https://doi.org/10.1152/ajpregu.00076.2014
176. Damanhuri, H.A.; Burke, P.G.R.; Ong, L.K.; Bobrovskaya, L.; Dickson, P.W.; Dunkley, P.R.; Goodchild, A.K. Tyrosine hydroxylase phosphorylation in catecholaminergic brain regions: a marker of activation following acute hypotension and glucoprivation. *PLoS One* **2012,** *7*(11), e50535. https://doi.org/10.1371/joirnal.pone.0050535.
177. *Tron Legacy*, directed by J. Kosinski; written by E. Kitsis, A. Horowitz, B. Klugman, L. Sternthal (**2010**; Walt Disney Pictures); 125 min (see 56:30–57:00 for reference to "biodigital jazz").
178. Swanson, L.W. Biochemical switching in hypothalamic circuits mediating responses to stress. *Prog Brain Res* **1991,** *87*, 181–200. https://doi.org/10.1016/s0079-6123(08)63052-6
179. Sara, S.J. The locus coeruleus and noradrenergic modulation of cognition. *Nat Rev Neurosci* **2009,** *10*, 211–223. https://doi.org/10.1038/nrn2573
180. McCormick, D.A.; Nestvogel, D.B.; He, B.J. Neuromodulation of brain state and behavior. *Annu Rev Neurosci* **2020,** *43*, 391–415. https://doi.org/10.1146/annurev-neuro-100219-105424
181. Dagogo-Jack, S.; Rattarasarn, C.; Cryer, P.E. Reversal of hypoglycemia unawareness, but not defective glucose counterregulation, in IDDM. *Diabetes* **1994,** *43*(12), 1426–1434. https://doi.org/10.2337/diab.43.12.1426
182. Uematsu, A; Tan, B.Z.; Ycu, E.A; Cuevas, J.S; Koivumaa, J; Junyent, F., *et al*. Modular organization of the brainstem noradrenaline system coordinates opposing learning states. *Nat Neurosci* **2017,** *20*(11), 1602–1611. https://doi.org/10.1038/nn.4642
183. Seo, D.-o.; Bruchas, M.R. Polymorphic computation in locus coeruleus networks. *Nat Neurosci* **2017,** *20*(11), 1517–1519. https://doi.org/10.1038/nn.4663
184. Holloway, B.B.; Stornetta, R.L.; Bochorishvili, G.; Erisir, A.; Viar, K.E.; Guyenet, P.G. Monosynaptic glutamatergic activation of locus coeruleus and other lower brainstem noradrenergic neurons by the C1 cells in mice. *J Neurosci* **2013,** *33*(48), 18792–18805. https://doi.org/10.1523/JNEUROSCI.2916-13.2013
185. Nieber, K; Sevcik, J; Illes, P. Hypoxic changes in rat locus coeruleus neurons *in vitro*. *J Physiol* **1995,** *486*(Pt. 1), 33–46. https://doi.org/10.1113/jphysiol.1995.sp020788
186. Bodineau, L.; Larnicol, N. Brainstem and hypothalamic areas activated by tissue hypoxia: Fos-like immunoreactivity induced by carbon monoxide inhalation in the rat. *Neurosci* **2001,** *108*(4), 643–653. https://doi.org/10.1016/s0306-4522(01)00442-0
187. Guyenet, P.G.; Abbott, S.B.G. Chemoreception and asphyxia-induced arousal. *Respir Physiol Neurobiol* **2013,** *188*(3), 333–343. https://doi.org/10.1016/j.resp.2013.04.011
188. Magalhães, K.S.; Spiller, P.F.; da Silva, M.P.; Kuntze, L.B.; Paton, J.F.R.; Machado, B.H. et al. Locus Coeruleus as a vigilance centre for active inspiration and expiration in rats. *Sci Rep* **2018,** *8*, 15654. https://doi.org/10.1038/s41598-018-34047-w
189. Illes, P.; Sevcik, J.; Finta, E.P.; Frölich, R.; Nieber, K.; Nörenberg, W. Modulation of locus coeruleus neurons by extra- and intracellular adenosine 5'-triphosphate. *Brain Res Bull* **1994,** *35*(5–6), 513–519. https://doi.org/10.1016/0361-9230(94)90165-1
190. Dallaporta, M.; Perrin, J.; Orsini, J.-C. Involvement of adenosine triphosphate-sensitive K^+ channels in glucose-sensing in the rat solitary tract nucleus. *Neurosci Lett* **2000,** *278*(1–2), 77–80. https://doi.org/10.1016/S0304-3940(99)00898-8
191. De Bernardis Murat, C.; Leão, R.M. A voltage-dependent depolarization induced by low external glucose

in neurons of the nucleus of the tractus solitarius: interaction with KATP channels. *J Physiol* **2019,** *597*(9), 2515–2532. https://doi.org/10.1113/JP277729
192. Loewy, A.D.; Spyer, K.M., eds. *Central Regulation of Autonomic Functions.* Oxford University Press: Oxford, **1990**.
193. Blessing, W. W. *The Lower Brainstem and Bodily Homeostasis*; Oxford University Press: New York, NY, USA, **1997**. Available online at the Internet Archive: https://archive.org/details/lowerbrainstembo0000bles/page/n5/mode/2up. [urn:oclc:record:1176260336]. Last accessed on 21 May 2022.
194. Zséli, G.; Vida, B.; Martinez, A.; Lechan, R.M.; Khan, A.M.; Fekete, C. Elucidation of the anatomy of a satiety network: Focus on connectivity of the parabrachial nucleus in the adult rat. *J Comp Neurol* **2016,** *524*(14):2803–2827. https://doi.org/10.1002/cne.23992
195. Khan, A.M.; Grant, A.H.; Martinez, A.; Burns, G.A.P.C.; Thatcher, B.S.; Anekonda, V.T.; Thompson, B.W.; Roberts, Z.S.; Moralejo, D.H.; Blevins, J.E. Mapping molecular datasets back to the brain regions they are extracted from: Remembering the native countries of hypothalamic expatriates and refugees. *Adv Neurobiol* **2018,** *21*, 101–193. https://doi.org/10.1007/978-3-319-94593-4_6
196. Khan, A.M.; Perez, J.; Wells, C.E.; Fuentes, O. Computer vision evidence supporting craniometric alignment of rat brain atlases to streamline expert-guided, first-order migration of hypothalamic spatial datasets related to behavioral control. *Front Sys Neurosci* **2018,** *12* (Article 7):1–29. https://doi.org/10.3389/fnsys.2018.00007
197. Santarelli AJ, Khan AM, Poulos AM. Contextual fear retrieval-induced Fos expression across early development in the rat: An analysis using established nervous system nomenclature ontology. *Neurobiol Learn Mem* **2018,** *155*, 42–49. https://doi.org/10.1016/j.nlm.2018.05.015
198. Gu, G.; Roland, B.; Tomaselli, K.; Dolman, C.S.; Lowe, C.; Heilig, J.S. Glucagon-like peptide-1 in the rat brain: Distribution of expression and functional implication. *J Comp Neurol* **2013,** *521*, 2235–2261. https://doi.org/10.1002/cne.23282
199. Uschakov, A.; Gong, H.; McGinty, D.; Szymusiak, R. Efferent projections from the median preoptic nucleus to sleep- and arousal-regulatory nuclei in the rat brain. *Neurosci* **2007,** *150*, 104–120. https://doi.org/10.1016/j.neuroscience.2007.05.055
200. Loo, Y.T. The forebrain of the opossum, *Didelphis virginiana*. Part II. Histology. *J Comp Neurol* **1931,** *52*, 1–148. https://doi.org/10.1002/cne.900520102
201. Reiner, A.; Honig, M.G. Dextran amines: Versatile tools for anterograde and retrograde studies of nervous system connectivity. In *Neuroanatomical Tract-Tracing Methods 3: Molecules, Neurons, and Systems*; Zaborszky, L.; Wouterlood, F.G.; Lanciego, J.L., Eds.; Springer Science+Business Media, Inc.: New York, **2006**; pp. 304–335.
202. Swanson, L.W. *Brain Maps: Structure of the Rat Brain*; Elsevier: Amsterdam, 1992.
203. Ju, G.; Swanson, L.W. Studies on the cellular architecture of the bed nuclei of the stria terminalis in the rat: I. Cytoarchitecture. *J Comp Neurol* **1989,** *280*, 587–602. https://doi.org/10.1002/cne.902800409
204. Khan, A.M.; Watts, A.G. Tracking intracellular events associated with glucoprivic challenge in three forebrain regions that contain CRH neurons receiving hindbrain noradrenergic input. American Neuroendocrine Society, *2005 Workshop on the Neuroendocrinology of Stress*, Poster 29, 2005.
205. Khan, A.M.; Watts, A.G. Glucoprivic challenge is associated with elevated levels of phosphorylated signaling intermediates in discrete forebrain regions: Immunofluorescence studies of ERK1/2 and CREB [Program #634.15] *2005 Abstract Viewer/Itinerary Planner*. Washington, DC: Society for Neuroscience, 2005. Online.
206. Hahn, J.D.; Swanson, L.W. Connections of the juxtaventromedial region of the lateral hypothalamic area in the male rat. *Front Syst Neurosci* **2015,** *9*, 66. https://doi.org/10.3389/fnsys.2015.00066